

HYDRAULIC STUDIES OF THE 18-PLATE ASSEMBLY IN THE MCMASTER
NUCLEAR REACTOR

HYDRAULIC STUDIES OF THE 18-PLATE ASSEMBLY IN THE MCMASTER
NUCLEAR REACTOR

By

TAESUNG HA, M.A.Sc (Mechanical Engineering)
Pohang University of Science and Technology, Pohang, Korea

A Thesis
Submitted to the School of Graduate Studies
in Partial Fulfilment of the Requirements
for the Degree
Master of Applied Science

McMaster University
© Copyright by Taesung Ha, April 2002

MASTER OF APPLIED SCIENCE (2002)
(Engineering Physics)

McMaster University
Hamilton, Ontario

TITLE: Hydraulic Studies of the 18-plate Assembly in the Mc-
Master Nuclear Reactor

AUTHOR: Taesung Ha
M.A.Sc (Mechanical Engineering)
Pohang University of Science and Technology, Pohang,
Korea

SUPERVISOR: Dr. Wm. J. Garland, Professor
Department of Engineering Physics
McMaster University

NUMBER OF PAGES: xvi, 180

Abstract

To support the update of the safety analysis of McMaster Nuclear Reactor (MNR), the local velocities in the channels and the flow distribution through a typical MNR assembly have been investigated. Velocity measurements in a mock-up of the 18-plate fuel assembly were conducted over the range of mass flow rate, $M=2.0\text{--}5.0$ kg/s (velocity, $U_n = 0.59\text{--}1.48$ m/s). To enable the velocity measurement in the channels by Laser Doppler Velocimetry (LDV), the curved fuel plate in the assembly was modified to flat plates. The velocity distributions both in the individual channels and through the assembly are obtained, as well as the channel-to-channel flow distribution in the assembly.

The present experiment shows that the velocity distribution is fairly symmetric from channels 1 to 17 centered about channel 9 in the assembly. The flow in the individual channels can be simply approximated as flow between parallel plates. The flow is relatively uniformly-distributed from one channel to another; the outmost channels (channels 1 and 3) have an average flow of about 95–97% of the assembly average flow and the central channels (channels 4 and 8) have about 103–105%. This result is compared to those of previous studies and Yu's numerical simulation. From this comparison, the entrance effect (the inlet flow condition from the reactor pool to the top end fitting) is one of the most influential factors on the channel-to-channel flow distribution among the entrance effect, the handle effect (the handle in the top end fitting), and exit effect (the flow stream bending to enter the bottom end fitting).

Pressure drop was measured through the simulated 18-plate assembly and is accurately predicted by a simple 1-D correlation. The pressure drop is related mainly to the frictional resistance in the 17 channels (about 60% of overall pressure drop) but the minor pressure losses are not considerable. Flow visualization shows the detailed flow behavior in the top end fitting and in the plate-free duct just above the bottom end fitting.

Acknowledgement

The author wishes to express his gratitude toward his supervisor, Dr. William J. Garland of the Department of Engineering Physics, for his critical readings and constant support through the course of this thesis.

His thanks also go to his colleagues Tai Shih Nguyen, Simon Day, and Rongsheng Yu, for their constructive comments and suggestion. He also wishes to thank the Stern Laboratories Inc. for their support and advice to complete the experiment for this thesis. My special thanks should go to Kyong Shin, and Eddy. Without their generous assistant and invaluable technical advice, this work would have never been completed.

He wants to express his appreciation for the financial support provided by the AECL in the form of AECL-Kapyong scholarship, which gave him the chance to study in Canada, as well as by the Department of Engineering Physics and school of Graduate Studies at McMaster University.

Mostly, he'd like to thank his family, his wife (Sunnyu Lim), daughter (Christine Hyunjeong), mother, sisters for their consistent support and encouragement throughout this endeavor.

Contents

Contents	ix
List of Figures	xiii
List of Tables	xiv
1 Introduction	1
2 Literature review	4
3 McMaster Nuclear Reactor (MNR)	7
3.1 Introduction	7
3.2 Standard 18-plate assembly	12
3.3 Other components in the reactor core	14
4 Hydraulic characteristics in MNR core	15
4.1 Introduction	15
4.2 Hydraulic characteristics in standard 18-plate assembly	18
4.2.1 Velocity	18
4.2.2 Pressure drop	25
4.3 Summary	29

5	Experimental apparatus and measurement	30
5.1	Simulated 18-Plate assembly	30
5.2	Test loop for the 18-plate assembly flow simulation	35
5.3	Measurement	40
5.3.1	Velocity measurement	40
5.3.2	Pressure measurement	43
5.3.3	Flow rate measurement	46
5.3.4	Temperature measurement	46
5.4	Experimental Reynolds number	47
5.5	Data acquisition system	47
5.6	Flow visualization	51
6	Velocity profile and flow distribution	53
6.1	Control of flow rate and temperature through test loop	53
6.2	Velocity	58
6.3	Simulation of inflow to the calming length	60
6.3.1	Velocity distribution in the bottom of the calming length	60
6.3.2	Turbulent intensity in the bottom of the calming length	61
6.3.3	Summary	62
6.4	Vertical axial velocity distribution along the channels	65
6.4.1	Entrance region	65
6.4.2	Fully-developed region and exit region	67
6.4.3	Summary	68
6.5	Symmetry of velocity distribution through the assembly channels	70
6.6	Velocity profiles in the 18-plate assembly	73
6.6.1	Velocity profile in fully-developed region	73

6.6.2	Width-wise (Y) velocity profile in each channel	74
6.6.3	Exit effect on velocity profile	75
6.6.4	Summary	76
6.7	Flow distribution in the assembly	81
6.8	Handle effect on the flow in the assembly	83
6.8.1	Handle effect on Velocity Profile	83
6.8.2	Handle effect on flow distribution	84
6.8.3	Summary	84
6.9	Comparison of flow distribution with previous studies	88
6.9.1	Comparison of flow distribution with Rummens' experiment	88
6.9.2	Comparison of flow distribution with Blahnik's engineering calculation	91
6.9.3	Comparison of flow distribution with Yu's numerical simulation	93
6.9.4	Summary	94
6.10	Evaluation of flow rate through 18-plate assembly during experiment	98
6.11	Summary	100
7	Pressure drop in 18-plate assembly	102
7.1	Pressure drop through the channels	102
7.2	Pressure drop through the bottom end fitting	105
7.3	Overall Pressure Drop	107
7.4	Summary	109
8	Measurement uncertainty	110
8.1	Uncertainty in local velocity measurement in narrow channel	110
8.1.1	Uncertainty in measurement of the width-wise velocity distribution	111

8.1.2	Uncertainty in velocity measurement at thickness-wise (X) center	112
8.1.3	Summary	112
8.2	Uncertainty in pressure drop measurement	116
8.3	Uncertainty in flow rate measurement by orifice meter	116
8.4	Uncertainty in temperature measurement	118
8.5	Summary	118
9	Flow visualization in 18-Plate assembly	119
9.1	Flow visualization in calming length	119
9.2	Flow visualization in top end fitting	122
9.3	Flow visualization in plate-free duct	125
9.4	Summary	130
10	Conclusions	131
11	Recommendation for future work	134
A	18-Plate assembly flow simulator	140
A.1	Comparison of standard 18-plate assembly and simulated 18-plate assembly	140
A.2	Inspection of test section	144
B	Measurement instruments	148
B.1	Laser Doppler Velocimetry	148
B.2	Differential pressure transmitter	151
B.3	Flow orifice meter	152
B.4	Type T thermocouple	152

C	Calculation of average velocity	154
C.1	Calculation of average velocity in calming length	154
C.2	Calculation of average velocity in channels	155
D	Possible flow development past the handle	157
E	Channel flow with large aspect ratio	159
F	Flow rate calculation	161
G	Pressure drop calculation	164
G.1	Calculation of friction factor	164
G.2	Pressure drop calculation	170
G.3	Comparison of the pressure drop calculation with the experiment data	173
G.3.1	Comparison of the experimental data with Yu's numerical simulation	173
G.3.2	Comparison of the experimental data with 1-D correlation prediction	173
G.4	Ratio of pressure drop in each region to overall pressure drop along the assembly	174
G.5	Vertical pressure distribution in the plate region	175
H	Error analysis	177
H.1	Uncertainty in pressure drop measurement	178
H.2	Uncertainty in flow rate measurement	179
H.3	Uncertainty in temperature measurement	180

List of Figures

3.1	Primary heat transport system in MNR	9
3.2	Picture of the MNR core system in pool 1	10
3.3	Schematic of the reactor core system in MNR	10
3.4	Typical core layout in MNR	11
3.5	Standard 18-plate fuel assembly	13
4.1	Entrance effect in the assemblies from the pool and power density distribution	17
4.2	Coolant flow through standard 18-plate assembly in the reactor core .	22
4.3	Possible flow streams in the top end fitting of 18-plate fuel assembly .	23
4.4	Possible flow streams in the plate-free duct above the bottom end fitting of 18-plate fuel assembly	23
4.5	Coolant flow streams in the bottom end fitting of standard 18-plate assembly	24
4.6	Schematic of pressure drop calculation along the standard 18-plate assembly	28
5.1	Comparison of the standard 18-plate assembly and the simulated 18-plate assembly from top plane view	33
5.2	Schematic of the 18-plate fuel assembly from axial side view	34
5.3	Schematic of the test loop for the 18-plate assembly flow simulation .	37
5.4	Picture of the 18-plate assembly flow simulator	38
5.5	Picture of the test section	38
5.6	Picture of the surge tank	39

5.7	Picture of layout for measurement devices	39
5.8	Schematic of LDV measurement points in the channels. Velocity at only a quarter cross-sectional area at two elevations is measured . . .	42
5.9	Pressure drop measurement and location of the pressure taps in test section	45
5.10	Schematic of data acquisition system	50
5.11	Schematic of flow visualization by DFV technique in the flow simulation	52
6.1	Variation of the flow rate (M) and temperature (T) during the measurement at M=3.0 kg/s and $T = 30^{\circ}\text{C}$	56
6.2	Flow rate variation during the measurement at M=2.0–5.0 kg/s . . .	56
6.3	Temperature variation during the measurement at M=2.0–5.0 kg/s . .	57
6.4	Typical signal of raw voltage of the transient velocity in the channels	59
6.5	Dimensionless velocity profiles in calming length at Z=725 mm at M=3.0 kg/s	63
6.5	Cont'd	64
6.6	Turbulent intensity distribution in the calming length	64
6.7	Axial dimensionless velocity profiles from the channel inlet	69
6.8	Symmetry of dimensionless velocity profiles through the channels in the test section	72
6.9	Dimensionless velocity profiles with the handle on at Z=300 mm at M=2.0–4.5 kg/s	78
6.10	Widthwise velocity profile in the channels	79
6.11	Exit effect on the velocity profile in the channels	80
6.12	Channel-to-channel flow distribution in the assembly	82
6.13	Handle effect on dimensionless velocity profiles at Z=300 mm at M=2.0 and 5.0 kg/s	86
6.14	Handle effect on the channel-to-channel flow distribution at M=2.0 and 5.0 kg/s	87

6.15	Comparison of the channel-to-channel flow distribution in the laminar flow regime	95
6.16	Comparison of the channel-to-channel flow distribution in the turbulent flow regime	96
6.17	Comparison of the channel-to-channel flow distribution of the experiment and numerical simulation in the turbulent regime	97
6.18	Comparison of the nominal flow rates and the measured flow rates	99
7.1	Pressure drop through the plate region in the assembly	104
7.2	Pressure drop through the bottom end fitting in the assembly	106
7.3	Pressure drops through the assembly	108
8.1	Widthwise (Y) velocity distribution in the channels	114
8.2	Thickness-wise (X) velocity distribution in the channels	115
9.1	Flow visualization in the calming length duct at $M=1.2$ kg/s	121
9.2	Flow visualization in the junction of the calming length duct and the top end fitting at $M=0.8$ kg/s	123
9.3	Flow visualization in the junction of the calming length duct and the top end fitting at $M=1.2$ kg/s	124
9.4	Flow visualization in the plate-free duct at $M=0.8$ kg/s	128
9.5	Flow visualization in the plate-free duct at $M=1.2$ kg/s	129
A.1	Property comparison of the peripheral sub-channel	141
A.2	Property comparison of the central sub-channel	142
A.3	Property comparison of the standard assembly and the simulated assembly	143
A.4	Inspection result of Al plates	145
A.5	Inspection result of the calming length and test section	146
A.6	Entrance effect in the assemblies from the pool and power density distribution	147

B.1	Schematic of single beam LDV system.	150
B.2	Schematic of positioning of the LDV measuring volume in the channel	150
C.1	Velocity measurement points and scheme of average velocity calculation in calming length on top of test section	155
C.2	Velocity measurement points and scheme of average velocity calculation in the channels	156
D.1	Schematic of the possible flow streams and the axial velocity distribution in the top end fitting	158
E.1	Turbulent velocity profiles in rectangular channel	160
G.1	Vertical pressure distribution along the assembly from Yu's numerical simulation	176

List of Tables

5.1	Property comparison of the standard 18-assembly and the simulated assembly	31
5.2	Reynolds numbers for all the experimental cases	48
8.1	Summary of uncertainty analysis	117
B.1	Pressure transmitters and their application	151
B.2	Coefficients of 7th order inverse polynomial for the temperature conversion	153

NOMENCLATURE

Acronym

AR	aspect ratio (width to thickness ratio)
DFV	direct flow visualization
DP	pressure drop across the orifice meter
DPFUL	pressure drop across the plate region
DPOUT	pressure drop across the bottom end fitting
DPTS	overall pressure drop across the test section
HUT	hold-up tank
LDV	laser doppler velocitmetry
MNR	McMaster Nuclear Reactor
SL	Stern Laboratory

Symbol

Description

A_i	cross-sectional area at a given region
A, B, C	instrument calibration constants
C_d	discharge coefficient
d	orifice meter diameter, [m]
D_h	equivalent hydraulic diameter
d_f	distance from the front of the lens to the window, [m]
E	velocity approach factor
F	actual focus length of LDV, [m]
F_a	thermal expansion factor
F_D	focal distance of LDV lens, [m]
f_i	friction factor
f_c	friction correction factor
g	gravitational acceleration, $g=9.8$ m/s
h	half length of channel thickness, $h = t_w/2$, [m]
K	non-reversible loss coefficient
L	length, [m]
L_e	hydrodynamic entrance length, [m]
M	flow rate, [kg/s]

p	pressure, [pa]
P	perimeter, [m]
Q	volumetric flow rate, $Q=M/\rho$ [L/s]
Re	Reynolds number, $Re = \frac{\rho U D_h}{\mu}$
T	temperature, [°C]
Tu	turbulent intensity
t	time, [sec]
t_w	channel thickness, [m]
U	time-averaged velocity, [m/s]
u	local instant velocity, [m/s]
$(u - U)$	fluctuating term of velocity, [m/s]
U_{rss}	relative overall uncertainty
V	area-averaged velocity, [m/s]
W	channel width, [m]
X, Y, Z	coordinate
x^*, y^*, z^*	dimensionless coordinate

Greek

β	diameter ratio, $d_{\text{orifice}}/D_{\text{tube}}$
η	expansion factor
μ	fluid viscosity, [kg/m/s]
ρ	fluid density, [kg/m ³]
φ	angle the incident beam makes with the optical axis
ε	boundary layer thickness, [m]

Subscript

CL	calming length
$crit$	critical
$handle$	assembly handle
avg	average
TP	top end fitting

Chapter 1

Introduction

Thermal-hydraulic studies in nuclear reactors are mainly associated with the effort involving the integration of heat transfer and fluid mechanics principles to accomplish the desired rate of heat removal from the reactor core under both operating and accident conditions. This study is an important field for nuclear reactor design and safe operation since it relates to the nuclear analysis and reactor safety analysis. For the safety aspect, sufficient cooling of fuel assemblies in the nuclear reactor has been crucially important. The heat generated from the nuclear fission energy should be properly removed to prevent fuel failure as well as to utilize the nuclear energy for the generation of electricity for economic purposes. Thus, the fuel assemblies in nuclear reactors are designed to have excellent heat transfer areas but must be kept under the critical heat flux condition to avoid burnout. Coolant circulates through the channels in the assemblies of the reactor core to remove the heat energy generated and to keep fuel surface temperature below safe limits. Insufficient local or overall cooling may lead to a fuel sheath burnout, its structural damage, and subsequently release radioactive fission products.

Despite the wide usage of plate-type fuel assemblies in research reactors around the world, only a few thermal-hydraulic studies have been conducted and their experimental data have not been well documented. A few thermal-hydraulic studies at McMaster Nuclear reactor (MNR) has been conducted in the past [2-5]. Up to the present, these studies in MNR have been focused on engineering calculations and experiments in limited cases, which deduced the channel-to-channel flow distribution in the assembly, and the assembly-to-assembly flow distribution in the reactor core. However, these studies did not include the velocity distribution in the individual channels of the assembly.

Day [1] reported the power density distribution in the 18-plate assembly. The plate-to-plate power density distribution showed the highest power density in the outmost plates and the lowest power density in the central plate; it was slightly decreased toward the central plate. Its side-to-side distribution in the channels also had a similar distribution. Thermal-hydraulically, therefore, the hottest area in the assembly may be near the side plates of the second-to-outermost plates. This raised the interest in the local velocity information especially near the side plates with the side-to-side velocity distribution in the channels for safety reason. In addition, the velocity near the channel exit (especially near the side plates) in the outer channels may be influenced due to the bottom end fitting. Thus, the necessity in the local velocity information in the channels has been raised for MNR safety analysis. The objective of the present study is to provide the experimental database of the hydraulic characteristics in the channels of the 18-plate assembly for the assessment of thermal-hydraulic aspects of safety analysis update. For simplicity in the present work, only hydraulic characteristics in the 18-plate assembly in the central region of MNR core have been investigated and constant temperature throughout the assembly has been maintained. The velocity profile in the individual channels, the channel-to-channel flow distribution in the assembly, and the pressure drop through the assembly were experimentally measured over the MNR operating range: $M=2.0\text{--}5.0$ kg/s ($U_n=0.89\text{--}1.49$ m/s). Velocity was measured in the individual channels in a single assembly from the direct velocity measurement by Laser Doppler Velocimetry (LDV). Use of LDV required that the curved fuel plates in the standard 18-plate assembly be replaced with straight flat ones. The same wetted perimeter and hydraulic diameter were maintained. To simulate the inlet flow condition to the 18-plate assembly in the central region of the reactor core, an additional calming length duct was inserted on the top of the assembly. Velocity was measured at 54 local points in the channels at the experimental flow rates. From the measured velocity data, the velocity distribution in the individual channels and the channel-to-channel flow distribution in the assembly were obtained. The pressure drop was measured through the assembly and compared to the prediction by a simple 1-D correlation. The flow behavior in the assembly was visualized by a direct flow visualization method.

This thesis is composed of 10 main chapters. Chapter 2 will briefly review the

literature of the related studies. Chapter 3 will introduce the general aspect of the McMaster Nuclear Reactor (MNR). Chapter 4 will depict the hydraulic characteristics of the standard 18-plate assembly in the MNR, and Chapter 5 will describe the present experimental setup and the measurement technique, including the measurement points of the velocity and pressure drop along the assembly, and temperature through the experimental loop. Chapter 6 will discuss the hydraulic characteristics in the 18-plate assembly of the central channels in the MNR core, based on the result of the present experiment. The velocity profile in individual channels and the flow distribution from one channel to another will be discussed in more detail from the velocity measurements in the channels. Chapter 7 will show the measurement of the pressure drops through the assembly. These measured pressure drops will be compared to the pressure drops estimated by a simple 1-D correlation. Chapter 8 will analyze the measurement uncertainty of the velocity in the channels, the pressure drop along the assembly, and the temperature along the experimental loop. Chapter 9 will show the flow visualization in the assembly. The flow behaviors in the calming length duct, in the top end fitting, and especially in the bottom end fitting will be discussed in detail. Finally, Chapter 10 will summarize the results of the present experiment for the study of the hydraulic characteristics of the 18-plate assembly.

Chapter 2

Literature review

The plate-type fuel assemblies in the research reactors have been widely used. Several thermal-hydraulic studies have been performed experimentally and numerically. A few thermal-hydraulic studies of the assemblies at the McMaster Nuclear reactor (MNR) and of similar assemblies have been conducted in the past. The studies directly related to the present work are briefly summarized.

Kreyger et al[7] had performed hydraulic and thermal measurements at high flow velocities in the 19-plate and 23-plate fuel assemblies in the core of the High Flux Reactor at Petten, Netherlands. The measured temperature is proportional to power and inversely proportional to local flow, and thus can provide the information on the local flow in the assemblies. However, the Patten assemblies have slightly different geometry than MNR ones and its test condition of flow velocities through the channels was much higher than the nominal velocity in MNR. Its result may thus not be relevant for application to MNR.

Ernst[2] made engineering calculations for MNR heat transfer for 5 MW operation. To assess the heat transfer characteristics for the fuel assemblies in MNR, the coolant flow rate through the assembly channels were estimated from the information on the anticipated hydraulic resistance in the assemblies, and the flow distribution among the various types of assemblies in the core. It was used for the thermal-hydraulic analysis of 5 MW operation in MNR.

Osamusali et al[3] attempted the experimental simulation of the flow and the numerical modeling of the 10-plate assemblies of MNR. It showed that the assembly could be approximated as a flat parallel plate channel assembly. The heat transfer was numerically estimated from the reactor core inlet and outlet temperatures, and

average coolant flow rates. However, it is of limited application ability to MNR safety analysis since it was conducted over a restricted range of flow rate.

Rummens et al[4] conducted the experimental study of the thermal-hydraulics in the standard 10-plate and 18-plate assemblies in both the fuel assembly, simulator and the reactor core site. The channel-to-channel flow distribution in the assembly was evaluated from the measured pressure drop along the individual channels. The axial pressure drop distribution revealed significant entrance and the exit effects, and a non-uniform flow distribution among the channels was observed. The reactor-basis experiment showed no significant variation in flow rate among the core sites although the inlet flow pattern to the assemblies varied dramatically depending on the assembly location. However, this experiment had some limitations for application to MNR safety analysis. It had been conducted in the laminar regime, which is lower than MNR operating range of normally turbulent flow in all the channels. Since a single measurement of the pressure drop vertically along each channel was undertaken, the detailed information on the side-to-side flow variations anticipated in the individual channels and the local velocity were not captured. Furthermore, both of the entrance effect of the inlet flow to the assembly and the exit effect due to the bottom end fitting on the flow distribution were not investigated in detail.

For the recent update of the MNR safety analysis report, Blahnik[5] made engineering calculation for the velocity profile and the channel-to-channel flow distribution in the standard 18-plate fuel assembly for both laminar and turbulent regimes. The hydraulic resistances in the entry region of the top end fitting, in the plate region, and in the exit region near the bottom end fitting were assumed based on the published data in order to calculate the pressure drop in each channel of the assembly. The velocity profile and the channel-to-channel flow distribution in the assembly have been obtained as well as the minimum channel flow and maximum channel flow. It wasn't able to provide the accurate information for hydraulic analysis. However, it was a useful guide for comparison with the experimental data.

More recently, Yu[6] has made numerical simulations for thermal-hydraulic study of the standard 18-plate fuel assembly. The standard assembly was slightly modified to compare to the present experimental result by replacing the curved fuel plates

with flat ones. The velocity profile in the individual channels, the channel-to-channel flow distribution, and the temperature distribution in the assembly was obtained. Only the hydraulic results of the numerical simulation will be briefly compared to the experimental result of the present work in the text.

In the present study, the velocity profile in the individual channels and the channel-to-channel flow distribution in the assembly were experimentally obtained. These results will be compared to the hydraulic results in the 18-plate assembly from the previous works of Rummens' experiment, Blahnik's engineering calculation, and Yu's numerical simulation.

Chapter 3

McMaster Nuclear Reactor (MNR)

The McMaster Nuclear Reactor (MNR) is a pool type reactor used for research and isotope production purposes, and licensed for operation up to a maximum power of 5 Megawatts thermal (MW). The reactor is currently operated at 2 MW with enriched uranium fuel moderated by gravity driven light water.

3.1 Introduction

A schematic flowsheet of the MNR primary heat transport system shows in Fig. 3.1. The MNR is composed of major 6 parts [8]: 2 adjacent reactor pools, reactor core system, Hold-Up Tank (HUT), circulating pump, heat exchanger (HX), gate valves and check valves, and connecting piping of several different diameters. The reactor core system is located near the bottom of pool 1. Coolant flow results from the pressure difference (≈ 70 kPa) in between the reactor core and the HUT, which is approximately at atmospheric pressure. Coolant flows into the reactor core from the top and the side of pool 1 and downward through the core. After leaving the reactor core system, the coolant flows to the HUT via an outlet piping. The HUT and outlet piping into the HUT retains the coolant sufficiently for N^{16} - a short-lived (< 1 minute) radionuclide originating from activated oxygen in the water - to decay. The coolant is then pumped to the HX, which removes excess heat, and back to pool 2. Pool 1 and 2 are adjoined with a removable gate. A storage tank holds water for the time when either of the pools is emptied. A fission product monitor between the gate valves 42 and 43 contains a sodium iodine detector to scan for high concentration of radionuclides in the coolant.

The reactor core system in pool 1 is photographically shown in Fig. 3.2 and schematically in Fig. 3.3 [9]. The reactor core system is placed at 7.37 m below the water free surface in pool 1, and is composed of the reactor core, its supporting grid plate, plenum and flapper, and bellow. The reactor core is suspended by a movable supporting grid plate. This grid plate is made of 5 thick aluminium and defines the spacing of the core elements. This plate has a uniform matrix of through-holes which lock the bottom end fittings of the core assemblies, and smaller bypass holes (3/4 in.) for additional coolant flow. The plenum and flapper are placed in sequence below the grid plate. The plenum is a rectangular empty box, and the flapper is a cover for a 15 -diameter opening in the side of the plenum to constitute a safety mechanism in the reactor cooling system; it opens, initiating a reactor trip and permitting thermosyphoning under reduced coolant flow condition (< 1100 USGPM). The bellows is connected to the outlet piping through the reactor bottom floor. Coolant flows into the reactor core from the top and the side in pool 1, downward the core, through its supporting grid plate, through the rectangular plenum, through the bellows section and into the outlet piping.

The reactor accommodates many different configurations of fuel assemblies and its core consists of a 9×6 rectangular array of fuel, control, reflector and irradiation assemblies [9]. The layout of various types of these assemblies is schematically shown in Fig. 3.4. The grid plate in the reactor core holds 28 enriched uranium fuel assemblies, 7 graphite reflector assemblies (G), 6 control fuel assemblies (CR), 1 beryllium reflector assembly (Be), 2 Iodine irradiation sites (I), 1 central irradiation site (CIF), and 9 empty water sites (W). The control fuel assemblies that adjust reactor power level fit into gaps provided by certain fuel elements. The graphite reflector assemblies are made of graphite slabs to scatter neutrons back into the core. The central irradiation site is not fuelled and is used for material activation. The beryllium reflector assembly provides a beryllium neutron source to facilitate the reactor start-up. Enriched uranium fuel assemblies use classical plate-type elements and consist of standard 10-plate or 18-plate fuel assembly with either all, or all but the outer, plates fuelled. These plates are made of an aluminium-clad uranium aluminide, and are curved to minimize the contact between the plates upon potential buckling. Coolant circulates through the channels between these plates.

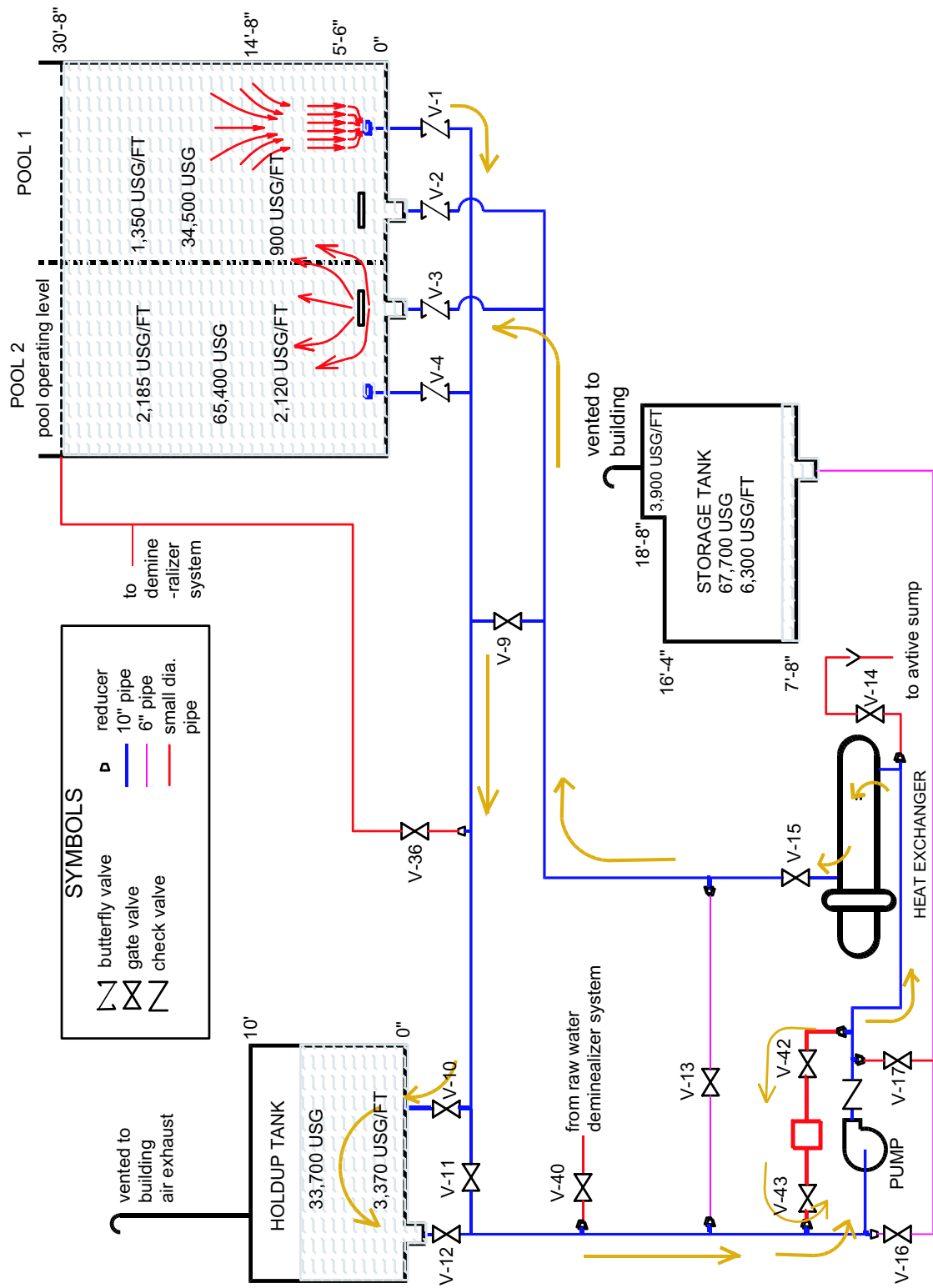


FIGURE 3.1: Primary heat transport system in MNR

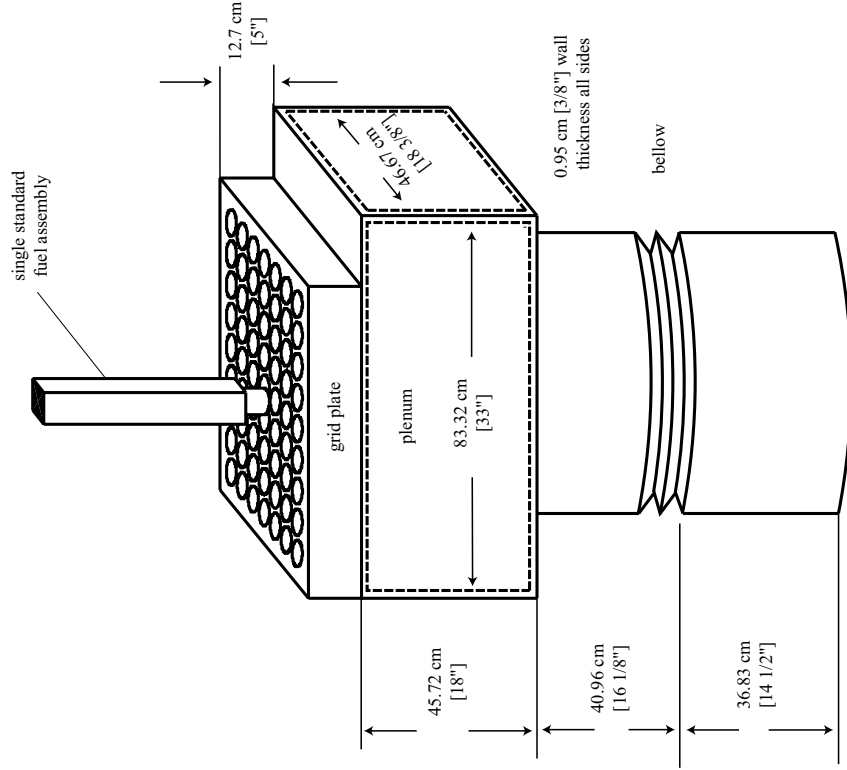


FIGURE 3.3: Schematic of the reactor core system in MNR

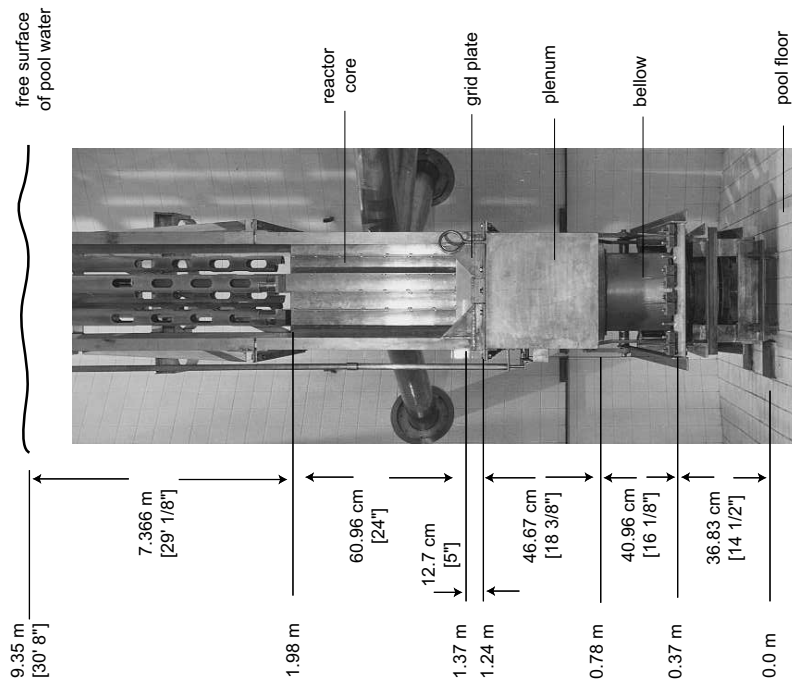


FIGURE 3.2: Picture of the MNR core system in pool 1

3.2 Standard 18-plate assembly

The standard 18-plate fuel assembly is composed of 16 curved fuel plates and 2 outside curved dummy plates as shown in Fig. 3.5 [10]. These plates are firmly held between two aluminium (Al) side plates. The fuel plates are made of Al plates with fuel meat and its cladding inside, while the 2 dummy plates are made of solid Al plates. From its axial side view, the assembly can be divided into three main parts: the top end fitting, the plate region, and the bottom end fitting. The top end fitting is 50.8 mm long, and is an empty rectangular duct with no plates placed inside. The 9.5 mm-diameter handle is located about 38.1 mm above the top end of the fuel plates. The plate region is 625.5 mm long, and the 16 fuel plates are inserted to make 17 flow channels with the 2 dummy plates. The bottom end fitting is 171.45 mm long, and the flow area is abruptly transformed from a rectangular duct to a circular pipe. This pipe is further gradually contracted from 62.71 to 50.80 mm in diameter. In addition, there is 25.4 mm long plate-free duct just below the fuel plates in between the 17 flow channels and the circular entrance into the bottom end fitting. In the top plane view, it is clearly shown that there are the 17 flow channels associated with the 16 fuel plates and the 2 dummy plates. The fuel plates have the 139.7 mm-radius curvature. Hence, each flow channel is curved with the same inner dimensions (i.e., 3.00×66.32 mm). The flow cross-sectional area (A), wetted perimeter (P), and equivalent hydraulic diameter (D_h) for single flow channel can be calculated. Note that the actual plate width is not 66.32 mm but 66.96 mm due to its curvature.

$$A = 3.00 \times 66.32 = 198.96 \text{ mm}^2 \quad P = 2 \times (66.96 + 3.00) = 139.92 \text{ mm}$$

$$D_h = \frac{4A}{P} = \frac{4 \times 198.96}{139.92} = 5.6878 \text{ mm}$$

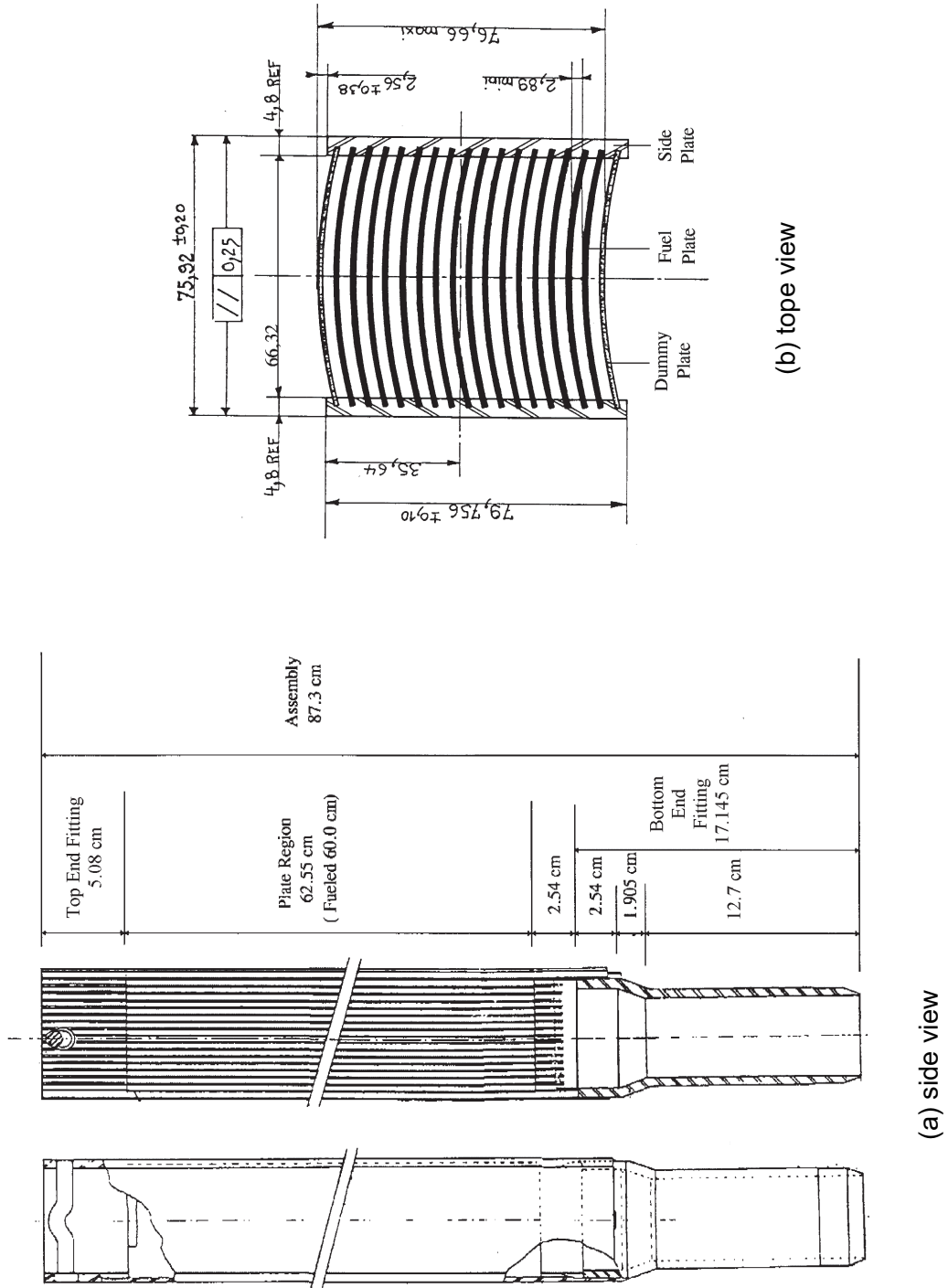


FIGURE 3.5: Standard 18-plate fuel assembly

3.3 Other components in the reactor core

PTR 10-plate fuel assembly is geometrically similar to the standard 18-plate fuel assembly but with all 10 plates fuelled. It is slightly different in the bottom end fitting and has only 9 internal flow channels with larger inner dimensions (i.e., 6.44×66.45 mm) when compared to the standard 18-plate fuel assembly. The control rod assembly is identical in dimensions to the standard 18-plate fuel assembly with the central 9 plates removed and a central slot added for the control rod. The top end fitting is extended by the addition of a shock absorber seat (separate piece which sits on top of the assembly). The graphite and the beryllium reflector assemblies are almost rectangular blocks with a central hole. The Al grid plate sits at the bottom of the reactor core and has a 9×6 array of 2.377 mm-diameter holes for the insertion of fuel assemblies. Bypass holes are drilled through this grid plate and can be plugged. Normally they are open for an additional bypass flow, and currently 22 of the 40 holes are open. A more detailed specification of the PTR 10-plate fuel assembly, control rod assembly, graphite reflector assembly, beryllium reflector assembly, and grid plate was reported in Reference 10. The MNR core system was briefly described in this chapter. Next, chapter 4 considers the hydraulic characteristics in the 18-plate assembly in the central region among the several types of the assemblies in the MNR core.

Chapter 4

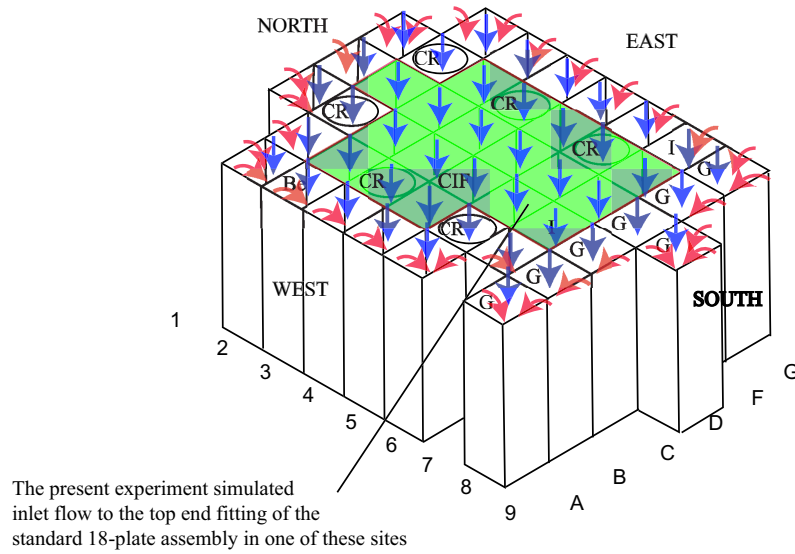
Hydraulic characteristics in MNR core

4.1 Introduction

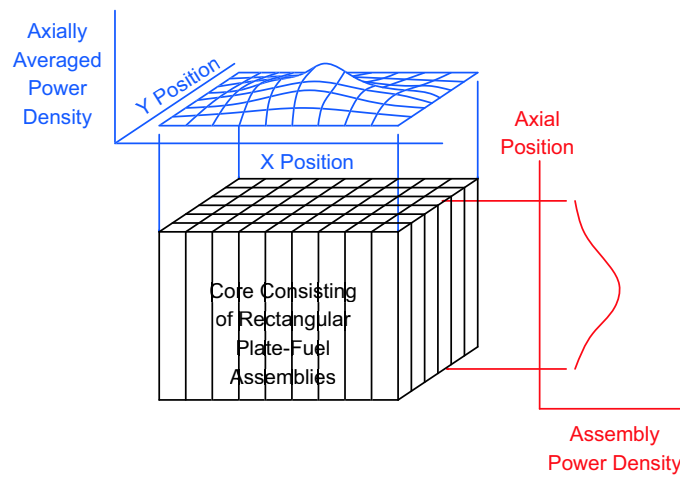
The coolant flow in the MNR primary heat transport system is driven by the acting pressure difference between the reactor core and the HUT, while that in the secondary heat transport system is pumped. This flow rate can be controlled by the valve (V-1, see Fig. 3.1). The possible inflow stream to the reactor core to the top end fittings of assemblies is roughly sketched in Fig. 4.1 (a). Note that 9 empty water sites were removed in this sketch. The coolant inflow pattern to the reactor core is slightly dependent on the location of the assemblies. In the outermost assemblies coolant flows into the assemblies from their top and one side, while coolant flows vertically downward into the assemblies only from their top in the central assemblies. In the corner assemblies, the inflow pattern is more complicated. The coolant flows into the assemblies from their top and 2 or 3 sides. Therefore, the flow distribution just above the fuel plates in the top end fittings of the assemblies should be significantly different, depending on their location. In addition to the main coolant flow through the assemblies, there is an additional flow through the gaps (i.e., major and minor bypass flow paths) between the individual assemblies as shown in Fig. 3.4 (b) and through the minor bypass flow path vertically along the outermost assemblies from pool 1 [9]. This additional flow passes into the bypass holes in the grid plate. Hence, the coolant flow into the reactor core and out through the grid plate is considerably complex. For the complete analysis of these complex hydraulic characteristics in the MNR core, the coolant flow through the assemblies and the bypass flow should be separately assessed, depending on the types of the assemblies and their location. In addition, the vertical and horizontal power density distribution in the reactor core, based on the neutron flux [1], is shown in Fig. 4.1 (b). Thermal-hydraulically,

higher temperatures can be attained along the central assemblies at a given operation condition than that in the outermost assemblies in the core. Thus the hottest area may occur near the side plates in the second-to-outermost plates (channel 2 to 3 or 15 to 16) in the central assemblies in the MNR core.

In the experimental study herein, the hydraulic characteristics through one of the standard 18 plates fuel assemblies in the central region of reactor core was investigated since this is the region of most interest from a safety viewpoint. The maximum temperature may occur near the bottom region of the channels of the assembly in this region. In addition, the inflow stream to the top end fitting in this region can be more simply simulated than that in the outermost region.



(a) possible inflow stream from pool 1 into reactor core



(b) vertical and horizontal power density distribution in reactor core

FIGURE 4.1: Possible inflow streams to the top end fittings of the assemblies from the reactor pool and power density distribution in the reactor core

4.2 Hydraulic characteristics in standard 18-plate assembly

The coolant through a single standard 18-plate assembly in the central region of the core flows through hydraulically complex flow paths, as illustrated in Fig. 4.2. Coolant is accelerated into the rectangular ducts from the pool water that is at rest. Then it undergoes the flow contraction into the multi-channel core before it is hydraulically fully developed. In the plate region, coolant flows independently through the parallel 17 flow channels, which have large aspect ratio, AR (i.e., width-to-thickness ratio) of approximately 22. Then the parallel multiple flow streams from the multi-channel merges into the plate-free duct just below the fuel plates. This flow is suddenly contracted to the bottom end fitting. Then an additional gradual flow contraction occurs further in the bottom end fitting.

4.2.1 Velocity

A stylized flow stream in the top end fitting is illustrated in Fig. 4.2 and 4.3. Coolant from pool 1 enters vertically downward into the plate-free duct of the top end fitting and separates by inertia from the inner surface close behind the entrance [11]. Then the flow meets the flow obstruction of the 9.53 mm-diameter handle located 38.1 mm ($\approx 4.0D_{h,handle}$) above the fuel plates. This handle obstructs the flow path above the central channels 8 to 10, and a vortex sheet and wake flow could form downstream just above these channels. This flow phenomenon might disturb the uniformly accelerated core flow upstream of channels 8 to 10; the axial velocity in their upstream may be substantially lower than the axial velocity upstream of the other channels. In addition, this flow separation and induced formation of eddies from the leading edge walls of the side plates and dummy plates might have an influence on the velocity in their immediate proximity. Therefore, the velocity profile may not be uniform above the channels but be severely disturbed due to the handle presence in the top end fitting.

In the plate region, the flow stream is relatively simple as shown in Fig. 4.2. The flow in the individual channels is accelerated into the multi-channel core from the top end fitting and then fully developed downstream. For the flow accelerated from the top end fitting to be fully developed in the channels, a finite channel length,

called the “hydrodynamic entrance length”, L_e , is required. This entrance length required is associated with the entrance configuration (i.e., abrupt or smooth) of the individual channels and upstream history (i.e., laminar or turbulent) [12]. For the purpose of estimating L_e , a uniform velocity profile just above the channels is assumed by ignoring the influence due to the handle. For laminar flow, the entrance length is a linear function of Reynolds number [13] :

$$\frac{L_e}{D_h Re} \simeq 0.06 \quad (4.1)$$

The maximum entrance length is attained at critical Reynolds number (i.e., $Re_{crit} \approx 2300$). Note that the constant in Eq. (4.1) decreases slightly with increasing aspect ratio of ducts. In turbulent flow, the boundary layer from the leading edge of the channel inlet grows faster, and the entrance length is relatively shorter and becomes almost independent of aspect ratio for all ducts [13].

$$\frac{L_e}{D_h} \simeq 4.4 Re^{1/6} \quad (4.2)$$

In addition, the entrance configuration can have an effect on the pressure distribution downstream of the channels [12]. An abrupt entrance configuration can cause the laminar-to-turbulent transition to occur at relatively low Reynolds number (i.e., $Re \approx 2000$), whereas the transition Reynolds number can be extended up to 7000 with a smooth entrance configuration. Hence, the entrance length with an abrupt entrance configuration is relatively shorter than that with a smooth entrance. For fully developed flow in the plate region, it may be assumed to be simple channel flow through narrow rectangular channels with high aspect ratio (AR= 22 : 1) by ignoring the curvature of the fuel plates. The flow can be assumed to be flow through parallel plates a distance t_w apart due to its high aspect ratio. Thus, the flow can be analytically solved for laminar flow [13]. The thickness-wise velocity profile is:

$$u = \frac{1}{2\mu} \left[-\frac{d}{dx} (p + \rho gz) \right] \quad (4.3)$$

where u =local flow velocity, μ =viscosity of fluid, ρ =density of fluid, $h(= t_w/2)$ =half length of channel thickness, p =pressure, g = gravitational acceleration, $g=9.8$ m/s.

If the rectangular channel has a width W , average velocity is:

$$V = \frac{Q}{Wh} = \frac{h^2}{3\mu} \left[-\frac{d}{dx} (p + \rho gz) \right] = \frac{2}{3} U_c \quad (4.4)$$

where W =channel width, V = average velocity in channel, Q =volumetric flow rate, U_c =velocity along the centerline at $x=0$, maximum flow velocity.

For turbulent flow between parallel plates, the fully developed velocity profile can be described by the logarithm law. The logarithmic law in the overlap layer can approximate a velocity profile across the entire channel [13]:

$$\frac{u(X)}{u_\tau} \approx \frac{1}{\kappa} \ln \left(\frac{Xu_\tau}{\nu} \right) + B \quad 0 < X < h \quad (4.5)$$

Note that X is wall coordinator in Fig. 4.2 (d), and the wall layer and the outer layer among the three regions in turbulent flow are neglected since both must have very small portion of the profile in the narrow channel. Average velocity is:

$$V = \frac{1}{h} \int_0^h u(X)dX = u_\tau \left(\frac{1}{\kappa} \ln \left(\frac{hu_\tau}{\nu} \right) + B - \frac{1}{\kappa} \right) \quad 0 < X < h \quad (4.6)$$

And, maximum velocity is along the centerline between parallel plates:

$$\frac{U_c}{u_\tau} = \frac{1}{\kappa} \ln \left(\frac{hu_\tau}{\nu} \right) \quad \text{at } X = h \quad (4.7)$$

The relationship relating average velocity to maximum velocity can be derived from Eqs. (4.6) and (4.7):

$$\frac{V}{U_c} \approx \frac{1}{1 + 0.86\sqrt{f}} \quad (4.8)$$

where u =wall-friction velocity, $u_\tau = (\tau_w/\rho)^{1/2}$, w =wall shear stress, κ, B =dimensionless constants, $\kappa = 0.41$, $B = 5.0$, ν = kinematic viscosity, $\nu = \mu/\rho$, X =wall coordinate, distance from the wall, f =friction factor by Eqs. (4.14) and (4.15).

In the width-wise direction, y , the side-plate walls provide additional frictional resistance (i.e., within 2 to 3 mm of the side-plate walls) in addition to the walls of the fuel plates. Thus, substantially lower coolant velocity occurs at the corner of the channels. Since only two fuel plates provide frictional resistance in the middle of the channel, the velocity profile may be similar to flow in an infinitely long narrow channel. Hence, the velocity may be substantially lower in the both corners and nearly constant in the middle of the channels as shown in Fig 4.2 (d).

In the exit region of the plate-free duct and the bottom end fitting, the flow stream is hydrodynamically complex, as shown in Fig 4.4 and 4.5. Below the fuel plates, flow area is abruptly expanded by the half of the plates' thickness on either side. Then it is abruptly contracted from a larger rectangular duct into a smaller circular pipe. Hence, the flow from the peripheral sub-channels, which are not aligned with the bottom end fitting pipe, must bend to reach the circular entrance. In contrast, the flow stream from the central sub-channels, which are aligned with the circular entrance into the bottom end fitting, is vertically straight downward. In addition, small eddy pairs could form just underneath the fuel plates and large eddies could form in the corners of the plate-free duct just above the bottom end fitting. The flow downstream behind the circular entrance also separates and the formations of eddies may be induced about the resultant jet [11] [15]. Thus, this jet contracts until a minimum area is attained at the section, called the "vena contracta", and then expands to fill the circular pipe until fully developed flow is established. However, the circular pipe at 25.4 mm downstream from the leading edge of circular entrance is further contracted over a short length (19.05 mm) gradually from 62.74mm-diameter to 50.8 mm-diameter tube. Therefore, the induced formation of eddies around the "vena contracta" may be fed into this convergent diffuser because the tube length is too short for fully developed flow to be completely established. The fully developed flow may be established far downstream in the 50.8 mm-diameter tube of the bottom end fitting before the flow enters the plenum. In summary, the hydrodynamics in this region is extremely complex because the flow of sudden expansion and contraction occurs abruptly over a relatively short length. Once the flow exits the fuel plates, the flow undergoes the expansion from the multi-channel core and then contraction into the circular entrance of the bottom end fitting. Then the flow undergoes a further contraction in the smaller tube of the bottom end fitting and is fully developed before the plenum.

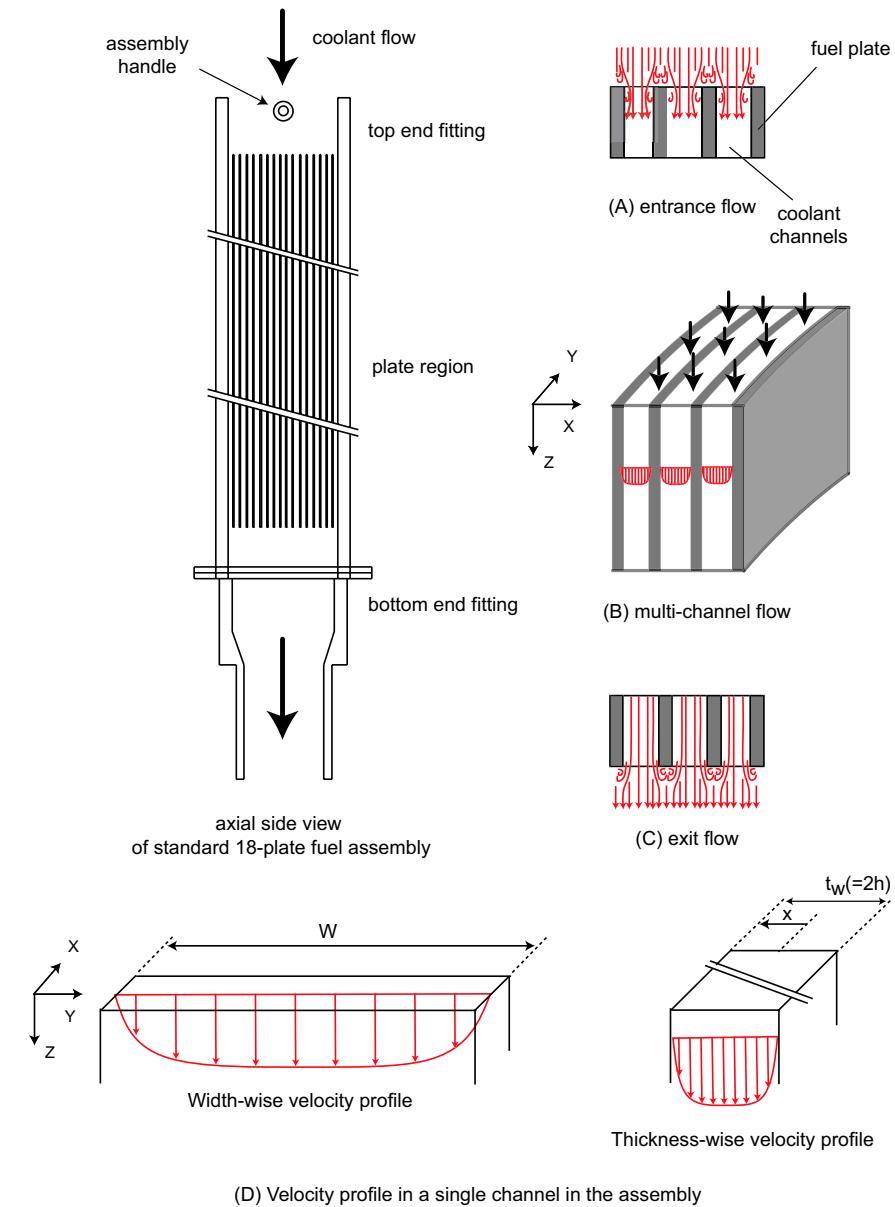


FIGURE 4.2: Coolant flow through standard 18-plate assembly in the reactor core

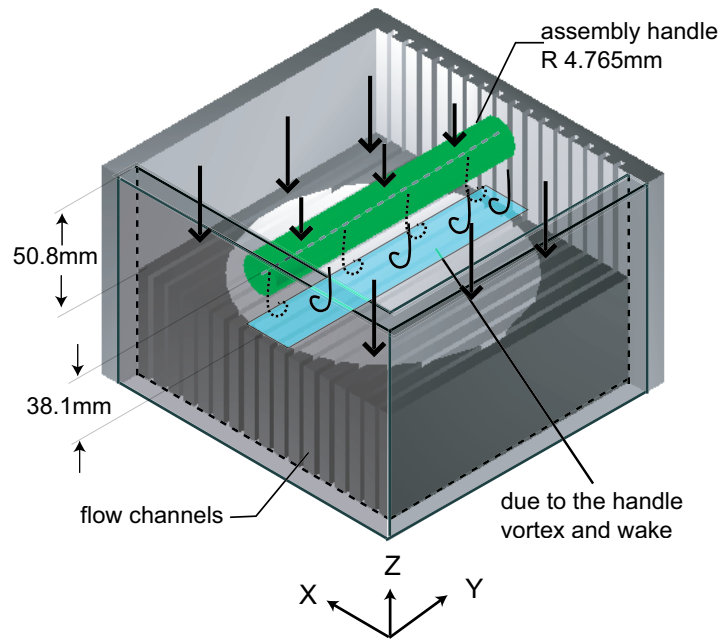


FIGURE 4.3: Possible flow streams in the top end fitting of 18-plate fuel assembly

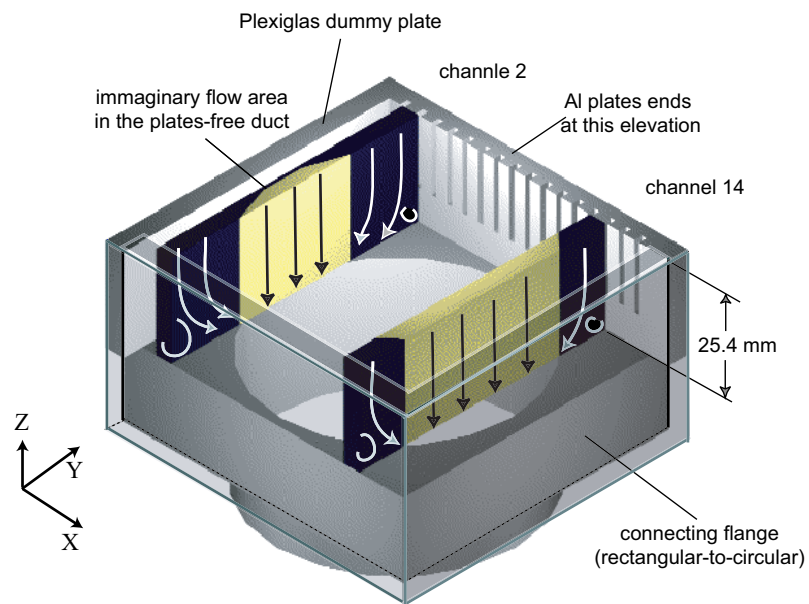


FIGURE 4.4: Possible flow streams in the plate-free duct above the bottom end fitting of 18-plate fuel assembly

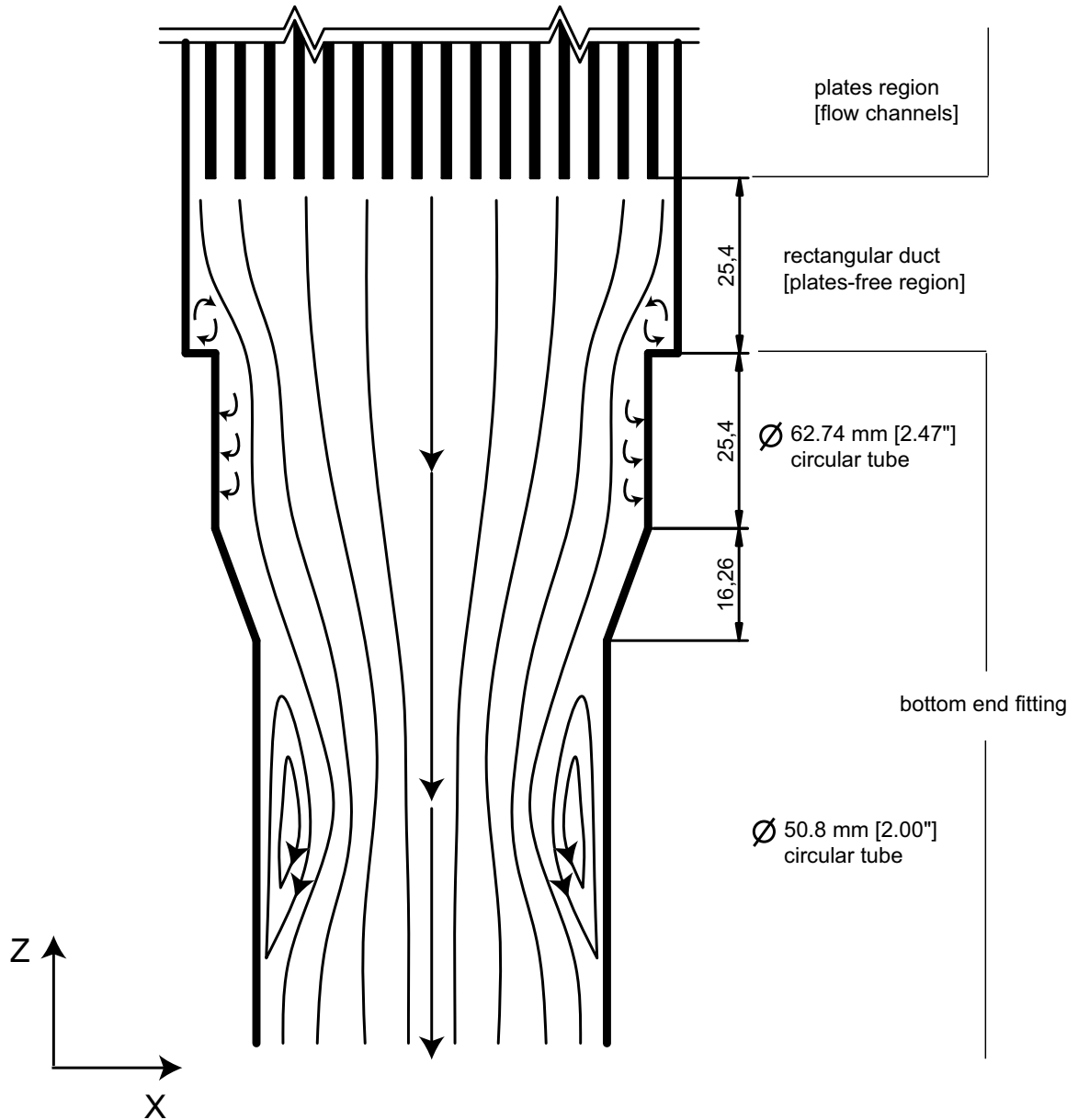


FIGURE 4.5: Coolant flow streams in the bottom end fitting of standard 18-plate assembly

4.2.2 Pressure drop

To estimate the pressure drop along the standard 18-plate fuel assembly [15], the fuel assembly can be divided into two sections (see Fig. 4.6): the “top section” including the region (0→1) plus part of the region (1→2), and the “bottom section” including part of the region (1→2) and the region (2→4). For the top section, the flow undergoes the flow contraction into the multi-channel core, the simple multi-channel flow, and then the flow expansion from the multi-channel core. The pressure drop for the abrupt contraction into the multi-channel core in the region (0→1) can be expressed:

$$p_0 - p_1 = \frac{1}{2}\rho U_0^2 \left(\frac{f_0 L_0}{D_{h,0}} \right) + \frac{1}{2}\rho U_1^2 \left(K_1 + \frac{f_1 L_1}{D_{h,1}} \right) + \rho g (L_0 + L_1) \quad (4.9)$$

The pressure drop for the abrupt expansion from the multi-channel core in the region (1→2) is:

$$p_1 - p_2 = \frac{1}{2}\rho U_1^2 K_2 + \frac{1}{2}\rho U_2^2 \left(\frac{f_2 L_2}{D_{h,2}} \right) + \rho g L_2 \quad (4.10)$$

The minor loss coefficients in Eqs. (4.9) and (4.10) are:

$$K_1 = 0.64 + \frac{38}{\text{Re}}, \quad K_2 = 0 \quad \text{for laminar flow}$$

$$K_1 = \frac{1}{2} \left(1 - \frac{A_1}{A_0} \right), \quad K_2 = \left(1 - \frac{A_1}{A_2} \right)^2 \quad \text{for turbulent flow}$$

Therefore, the pressure drop in the top section (0→2) can be estimated by adding Eqs. (4.9) and (4.10).

For the bottom section, the flow undergoes an abrupt contraction from a larger rectangular duct to a smaller circular tube, then further a gradual contraction from a larger diameter tube to a smaller one, and out through a smaller tube, as shown in Fig. 4.5 and 4.6. The flow in this region is extremely complex as explained in previous section and the flow may not be completely recovered downstream of the abrupt contraction (or upstream of the gradual contraction, region 3). However, assuming that the flow separation due to the abrupt contraction is completely recovered and then undergoes the gradual contraction to the smaller tube, the pressure drop through the bottom end fitting can be predicted by a 1-D correlation. For the abrupt contraction from the plate-free duct to the circular tube (2→3), the pressure drop

can be predicted:

$$p_2 - p_3 = \frac{1}{2}\rho U_2^2 \left(\frac{f_2 L_2}{D_{h,2}} \right) + \frac{1}{2}\rho U_3^2 \left(K_3 + \frac{f_3 L_3}{D_{h,3}} \right) + \rho g (L_2 + L_3) \quad (4.11)$$

For the gradual contraction from a larger diameter tube to a smaller one (3→4), the pressure drop can be:

$$p_3 - p_4 = \frac{1}{2}\rho U_4^2 \left(K_4 + \frac{f_4 L_4}{D_{h,4}} \right) + \rho g (H + L_4) \quad (4.12)$$

The minor loss coefficients in Eqs. (4.11) and (4.12) are:

$$\begin{aligned} K_3 &= 1.20 + \frac{38}{\text{Re}}, & K_4 &= \frac{64}{\text{Re}} & \text{for laminar flow} \\ K_3 &= \frac{1}{2} \left(1 - \frac{A_3}{A_2} \right), & K_4 &= 0.075 & \text{for turbulent flow} \end{aligned}$$

where p_i =pressure in the given region, U_i =average velocity in a given region, A_i =cross-sectional area of the given region, L_i =height of the given region, ρ =density of fluid, f_i =friction factor in a given region, K_i =non-reversible loss coefficient, g =gravitational acceleration, $g=9.8$ m/s, $D_{h,i}$ =equivalent hydraulic diameter of the given region, H =height of the gradual contraction region (3→4).

Therefore, the overall pressure drop in the bottom section (2→4) can be estimated from Eqs. 4.11 and 4.12.

For an estimation of the friction factor (f_{rect}) in the rectangular channel with large width to height ratios, it is recommended that a correction factor(f_c) be used to calculate the friction factor from that of pipe flow (f_{pipe}) [18].

$$f_{\text{rect}} = f_c \times f_{\text{pipe}} \quad (4.13)$$

For laminar flow ($\text{Re} < 2 \times 10^3$):

$$\begin{aligned} f_{\text{pipe}} &= \frac{64}{\text{Re}} \\ f_c &= 1.503 - 1.894 \left(\frac{t_w}{W} \right) + 2.034 \left(\frac{t_w}{W} \right)^2 - 0.755 \left(\frac{t_w}{W} \right)^3 \end{aligned} \quad (4.14)$$

For turbulent flow ($3 \times 10^3 < \text{Re}$):

$$\begin{aligned} \frac{1}{\sqrt{f_{\text{pipe}}}} &= -2 \log \left(\frac{\epsilon/D_h}{3.7} + \frac{2.51}{\text{Re} \sqrt{f_{\text{pipe}}}} \right) \\ f_c &= 1.097 - 0.177 \left(\frac{t_w}{W} \right) + 0.083 \left(\frac{t_w}{W} \right)^2 \end{aligned} \quad (4.15)$$

where f_{rect} =friction factor in rectangular duct, f_{pipe} =friction factor in pipe, f_c = correction factor, ϵ =roughness.

Assuming that the transition between laminar and turbulent regimes can be taken to occur at $2 \times 10^3 < \text{Re} < 3 \times 10^3$, the friction factors in this intermediate range are simply linearly-extrapolated between the value given by Eq. (4.14) at $\text{Re} = 2 \times 10^3$ and the value given by Eq. (4.15) at $\text{Re} = 3 \times 10^3$.

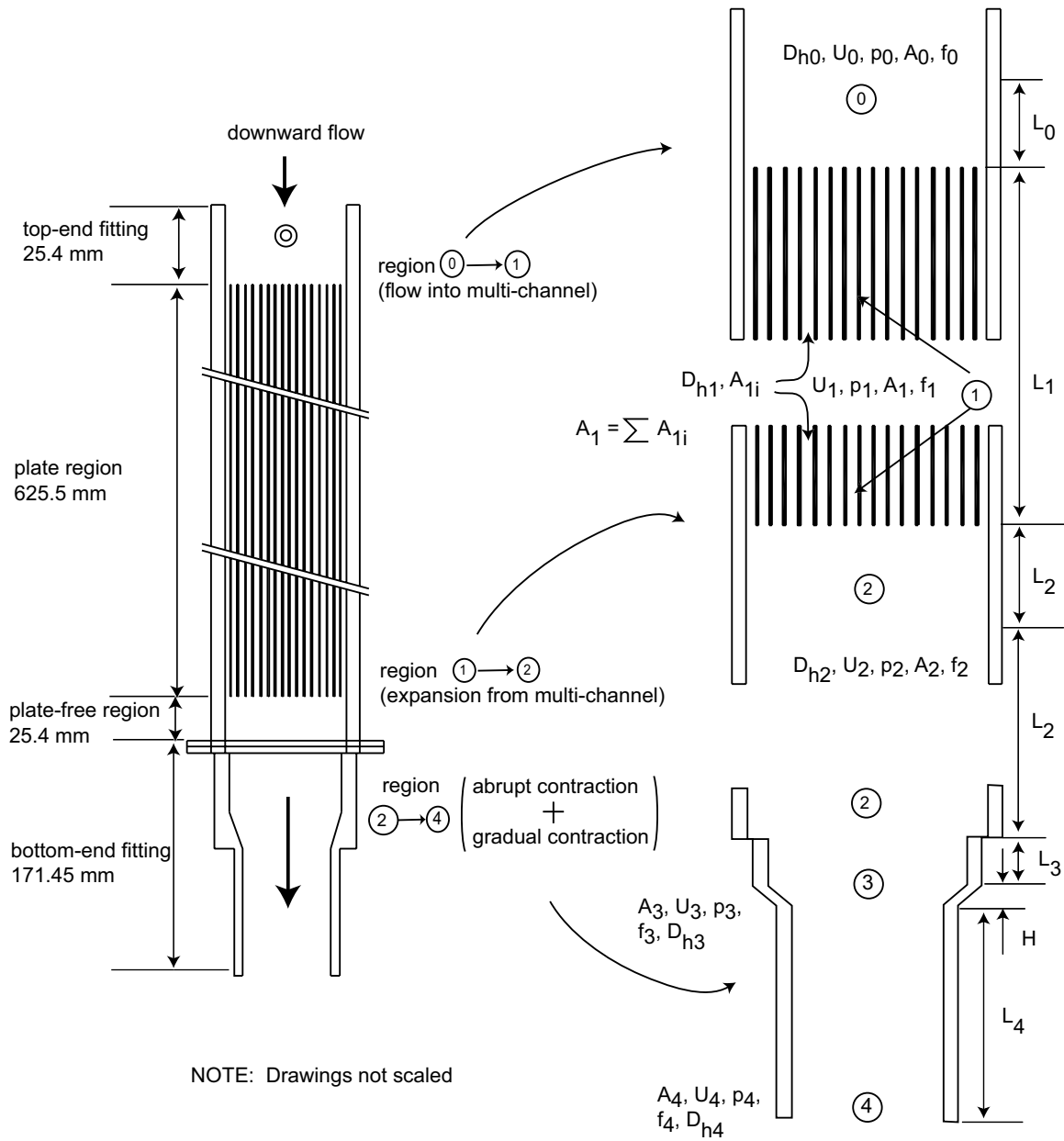


FIGURE 4.6: Schematic of pressure drop calculation along the standard 18-plate assembly

4.3 Summary

The flow through the channels in the 18-plate assembly in the central region of the MNR core is significantly complicated as previously discussed. To investigate this complex flow, velocity was measured by using direct measurement device (Laser Doppler Velocimetry) in the channels, and pressure drop was measured through the assembly by differential pressure transmitters, as described in the following Chapter 5.

Chapter 5

Experimental apparatus and measurement

To simulate the hydraulic characteristics in the standard 18-plate fuel assembly in the central region of the MNR core, the fuel assembly was slightly modified by replacing the actual curved plates with straight flat ones, and an additional calming length duct was inserted to simulate the inflow condition to the top end fitting in the reactor core. Velocity at various points in the channels of the assembly was measured using Laser Doppler Velocimetry (LDV). Pressure drops and temperatures were also measured along the assembly. To examine the complex flow behaviour from the plate-free duct into the bottom end fitting, flow visualization was conducted.

5.1 Simulated 18-Plate assembly

Laser Doppler Velocimetry (LDV) was selected for velocity measurement in the channels of the standard 18-plate assembly. Since LDV is a line of sight device, the standard 18-plate assembly should be slightly modified to permit the usage of LDV. The sixteen curved fuel plates were replaced with straight flat Al plates, and two Al dummy plates and two Al side plates were replaced with transparent Plexiglas sheets. However, the height of the simulated assembly was maintained at the same length. The geometric changes for the flow channels were compensated by maintaining the same equivalent hydraulic diameter of the individual channels. Consequently, the thickness of the individual channels was decreased from 3.00 mm to 2.97 mm, but their width was increased from 66.32 mm to 66.99 mm. In addition, their wetted perimeter and cross-sectional flow area were maintained, as shown in Fig. 5.1. Here the equivalent hydraulic diameter, wetted perimeter, and flow area for one flow channel were calculated in the same manner as in Section 3.2. Their comparison for

TABLE 5.1: Comparison of equivalent hydraulic diameter, wetted perimeter, and cross-sectional area for single flow channel of the standard 18-assembly and the simulated 18-plate assembly

	Standard 18-plate assembly	simulated 18-plate assembly
width W [mm]	66.32	66.99
thickness t_w [mm]	3.00	2.97
cross-sectional area A [m ²]	198.96	198.96
wetted perimeter P [mm]	139.92	139.92
equivalent hydraulic diameter D_h [mm]	5.6878	5.6878

the single flow channel in both cases is summarized in Table 5.1. The more detailed comparison caused by the geometric changes is discussed in Appendix A.1.

The sixteen flat Al plates were made from 1.27 mm thick solid Al plates without being fuelled inside, and two dummy plates and two side plates were fabricated from 13 mm thick Plexiglas sheet. To guide the insertion of sixteen Al plates, sixteen grooves with about 3 mm deep were carved into the surfaces of two side plates. The handle was fabricated from 9.53 mm-diameter brass rod. The heights of the top end fitting and the plate region in the simulated assembly were maintained the same as those in the standard assembly. The bottom nozzle for the bottom end fitting, where the flow channel configuration changes from a rectangular duct to a round pipe, was made from a cast Acrylic rod. To simulate the inlet flow condition to the top end fitting, an additional calming length was inserted on the top of the simulated assembly. It was fabricated from 13 mm thick Plexiglas sheet. Its height was 717.6 mm long with the same inner dimension (66.99×70.82 mm²) as that of the simulated assembly. To connect these individual parts to each other and with the test loop piping, four connecting flanges were manufactured from 50.8 mm thick Acrylic sheet. The detailed

information on the calming length and the test section of the simulated assembly is shown in the drawing of Fig. 5.2.

After the manufacture of all individual pieces, dimension inspection was undertaken. The individual pieces were glued together using liquid cement, and then sixteen Al plates were inserted. The handle was positioned 38.1 mm above the Al plates in the top end fitting. After assembling both the calming length and the test section, the inner flow area was measured. These inspection results are outlined in Appendix A.2.

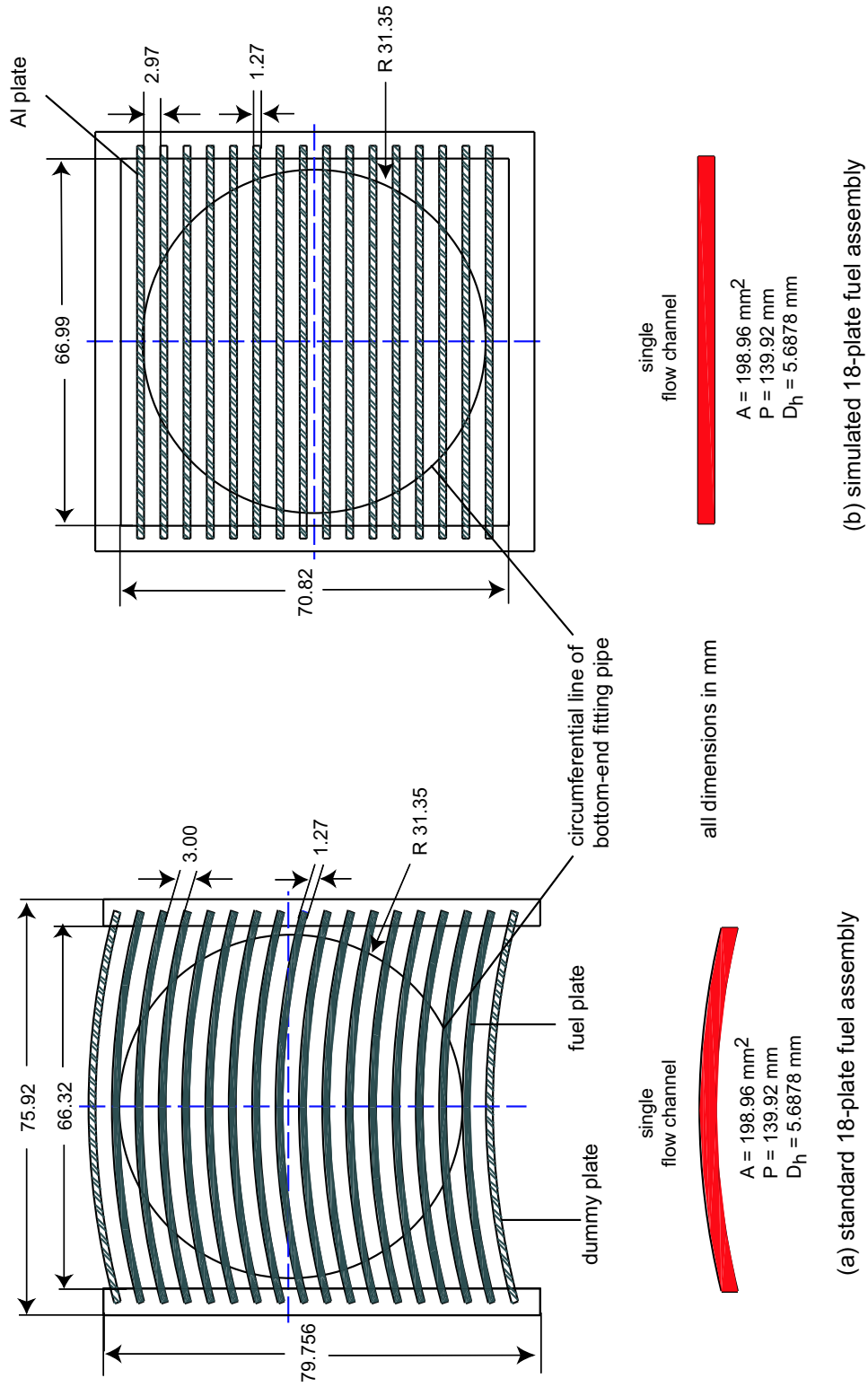


FIGURE 5.1: Comparison of the standard 18-plate assembly and the simulated 18-plate assembly from top plane view

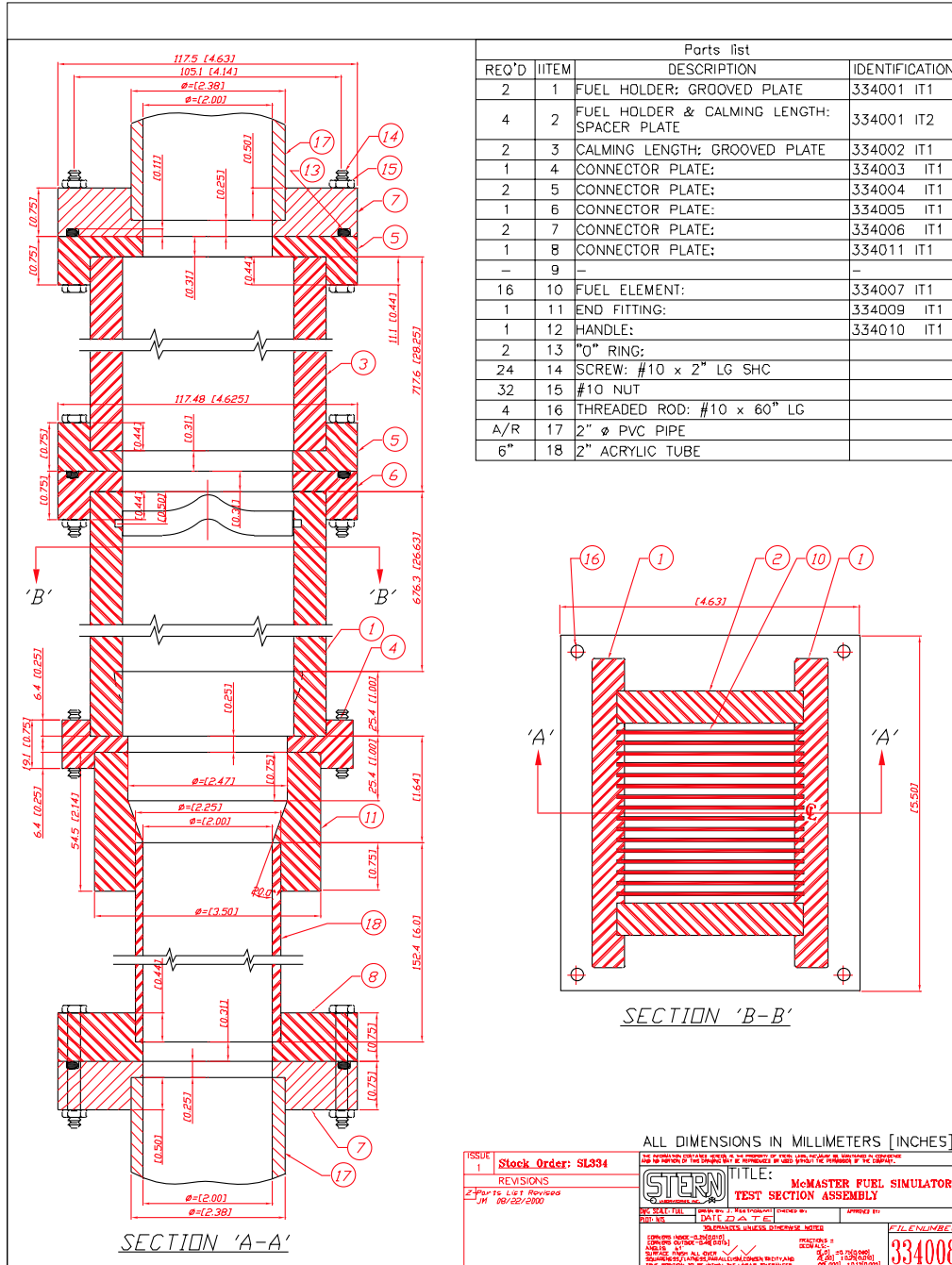


FIGURE 5.2: Schematic of the 18-plate fuel assembly from axial side view

5.2 Test loop for the 18-plate assembly flow simulation

The test loop for the 18-plate assembly flow simulation, as shown in Fig. 5.3, consisted of a circulating pump, an open surge water tank, a 18-plate assembly flow simulator, a flow orifice, an electric heater, a cooling tap water loop, and a flow control valve. The surge water tank was located to maintain a constant pressure in the channels. The circulating pump was connected to the surge tank, and would deliver a flow rate from 2.0 up to 5.0 kg/s. The test loop piping was made from plastic pipes and fittings. The test loop was filled with de-ionized water and operated approximately at the experimental temperature, 30 °C. The electric heater was used to heat cold de-ionized water up to the experimental temperature during the preliminary test run, and the cooling tap water loop was used to remove the pumping heat and maintain the loop water at the desired temperature.

The 18-plate assembly flow simulator was vertically positioned between the open surge tank and the circulating pump. It consisted of the calming length duct and the simulated 18-plate assembly (test section) as shown in Fig. 5.4 and 5.5. The calming length was placed on the top of the test section. They were connected by a rectangular-to-rectangular connecting flange, which had the same inner dimension ($66.99 \times 70.82 \text{ mm}^2$). The calming length was 717.6 mm long while the test section was 895.8 mm long. To connect the test loop pipe with both the calming length and the exit section of the test section, the rubber tube with the same inner diameter (50.8 mm) as the test loop piping was used. Their vertical lengths were 650 mm at the top of the calming length and 640 mm at the bottom of the test section, respectively. In addition, two type T thermocouples (T1, T2) were installed in the junction of the plastic pipe and the rubber tube at the top and the bottom, in order to measure the temperature variation through the 18-plate assembly flow simulator during the test.

A circulating pump, a flow orifice, and a flow control valve were installed to set the flow rate through the test loop. A centrifugal pump was utilized as a circulating pump to deliver a flow rate from 2.0 to 5.0 kg/s (i.e., $U_n=0.59\text{--}1.48 \text{ m/s}$). The pump of maximum capacity greater than 5.5 kg/s was selected to provide stable flow rates through the test loop. An orifice meter and a flow control valve were placed in sequence downstream of the pump. One differential pressure transmitter from

Rosemount Inc. was placed across the orifice meter to measure the pressure drop, which was converted to flow rate. By adjusting the flow control valve, the flow rate was set at the experimental condition.

An electric heater and cooling tap water loop were employed to control the temperature variation through the test loop. The electric heater was to heat cold de-ionized water to the experimental temperature ($30\text{ }^{\circ}\text{C}$) in the loop during the preliminary test run. The water temperature at the start of test was normally below the experimental temperature ($T \approx 15\text{--}20\text{ }^{\circ}\text{C}$). Once the test loop water was reached to the experimental temperature, the electric heater was turned off. However, additional heat was continuously supplied by the pumping. In order to remove this additional pumping heat, a cooling tap water loop was installed in the surge tank. Thus, the water in the test loop could be maintained within the desired range of the experimental temperature by controlling this cooling tap water loop.

An open surge water tank was used as an intermediate reservoir for the test loop water. It was located about 2.60 m above ground level to maintain a constant pressure head in the channels of the test section, as shown in Fig. 5.6. The pipe from the exit of the test section was submerged in the water from the top of the surge tank. Several small holes were drilled onto its sidewall surface to prevent the water level from fluctuating greatly by the momentum force induced as the circulating water was discharged into the surge tank. This was because the fluctuating water level in the surge tank could influence the performance of the pump, and consequently cause a fluctuation in flow rate in the test section. The other pipe feeding the water to the pump was connected on the bottom of the surge tank. The water level in the surge tank was maintained approximately by 0.60–0.70 m high during the test. An additional type T thermocouple (T3) was placed in the surge tank to measure the temperature variation through the test loop.

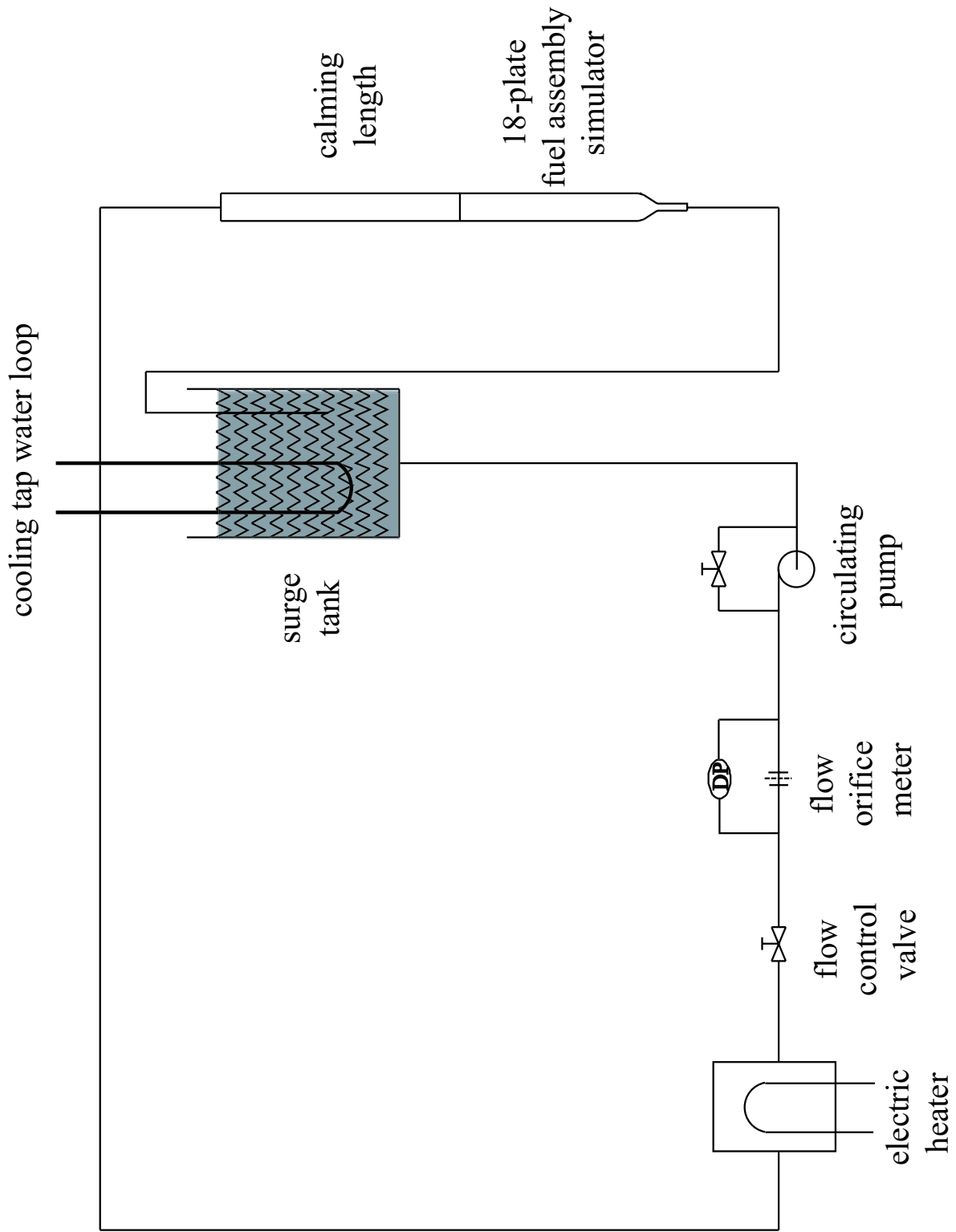
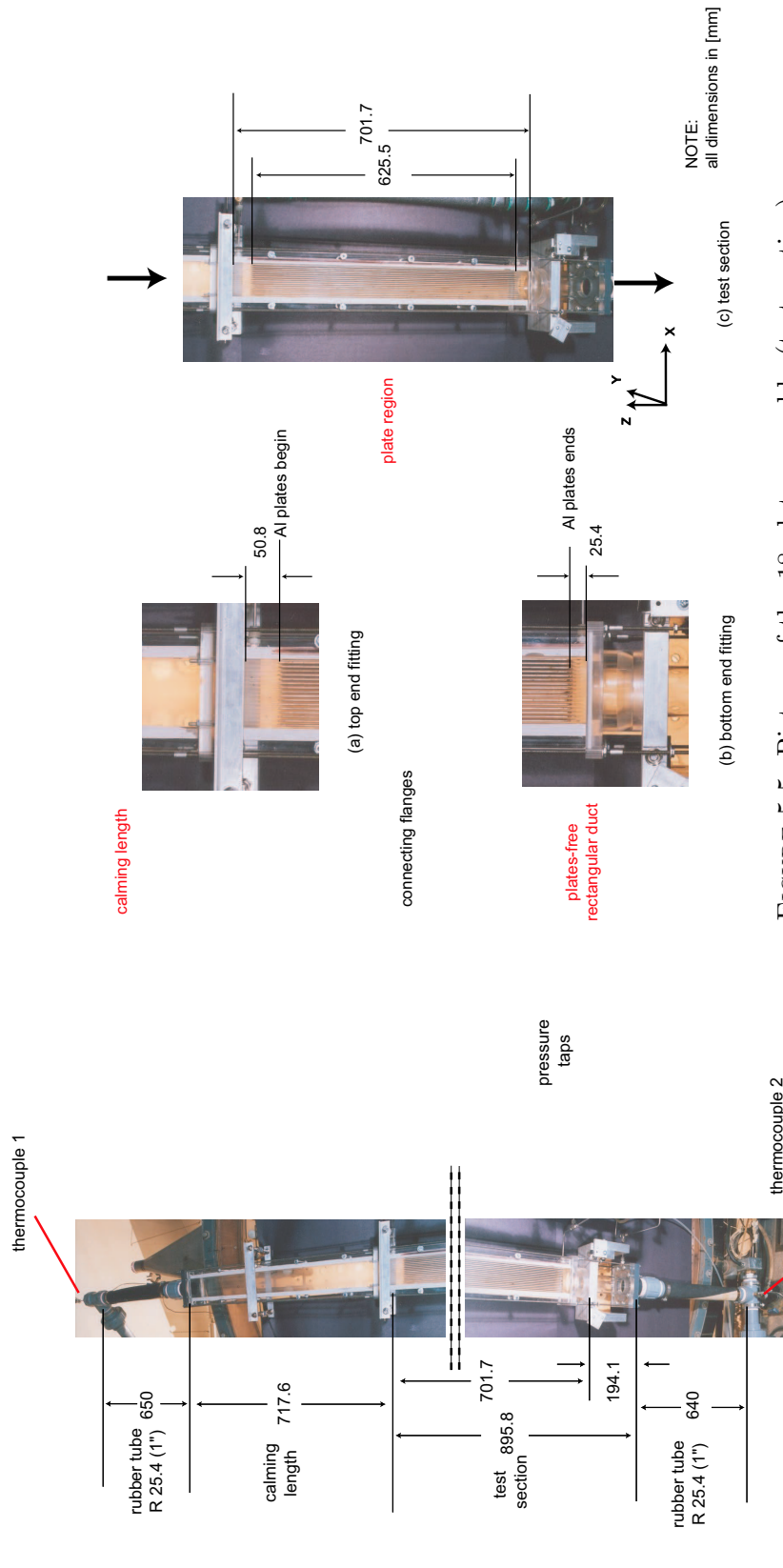


FIGURE 5.3: Schematic of the test loop for the 18-plate assembly flow simulation



NOTE:
 1. calming length and test section are vertically straight.
 2. all dimensions in [mm].

FIGURE 5.4: Picture of the 18-plate assembly simulator

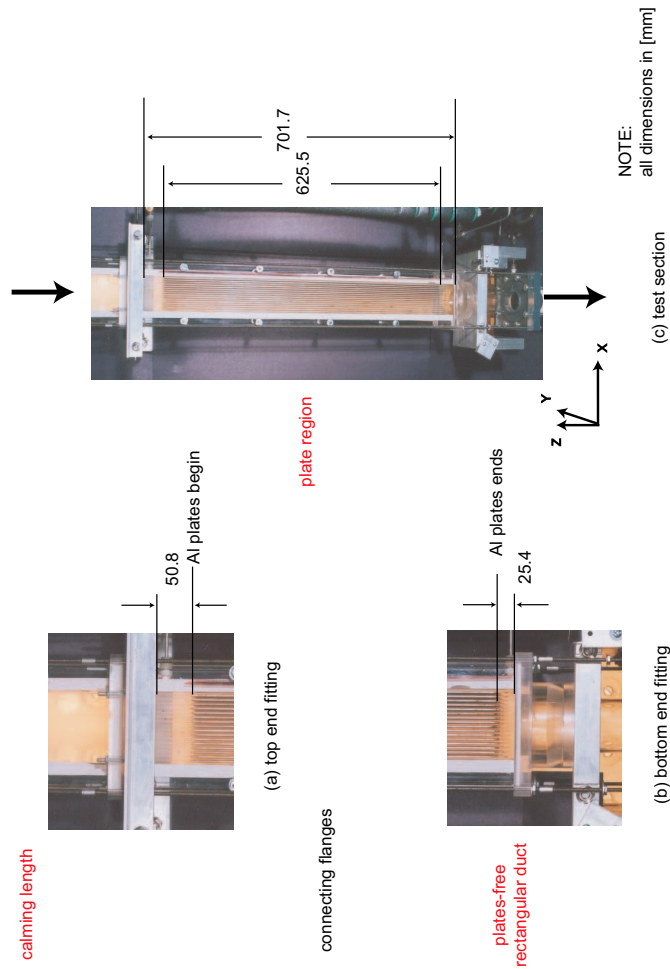


FIGURE 5.5: Picture of the 18-plate assembly (test section). It consists of the top end fitting (a), the plate region and the bottom end fitting (b)

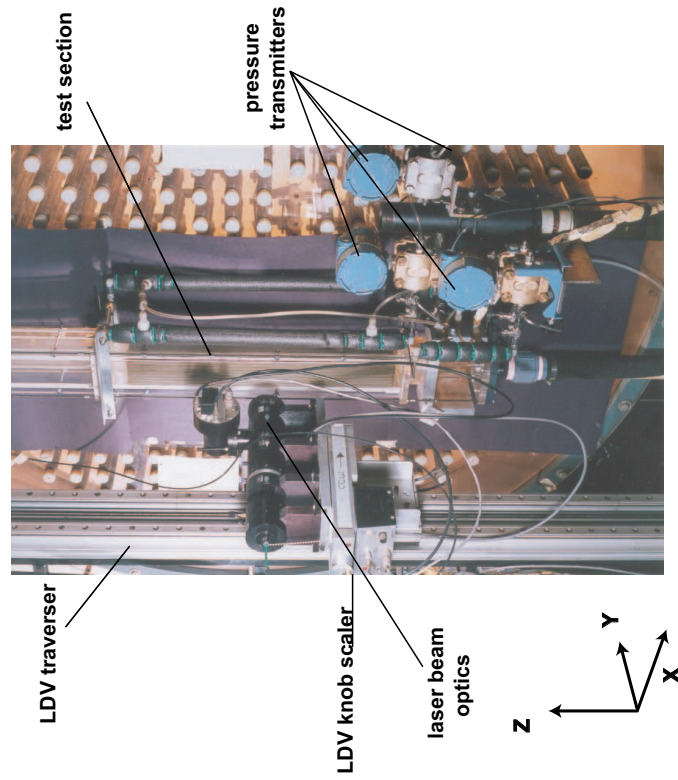


FIGURE 5.7: Picture of layout for measurement devices of velocity and pressure drop in test section

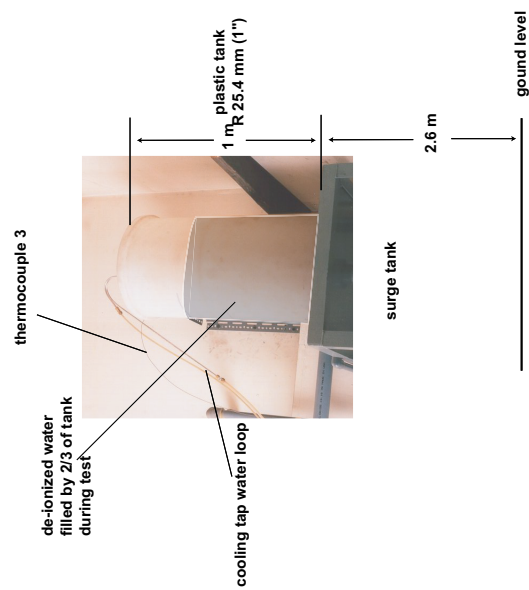


FIGURE 5.6: Picture of the surge tank

5.3 Measurement

Measurement of velocity, pressure drop, and temperature was undertaken through the test loop. The layout of devices for velocity and pressure drop measurements in the test section is shown in Fig. 5.7. The custom software developed by Stern Laboratory (SL) was used to control a data acquisition system and convert measured voltage to engineering units using instrument calibration constants, A, B, and C for pressure and temperature measurement.

$$\text{Data in Engineering units} = A + B \times V + C \times V^2 \quad (5.1)$$

where V =instrument output signal, [V], A, B, C =instrument calibration constants. Velocity, pressure drop, and temperature were measured at 10 Hz for 100 seconds as well as at 10 Hz for 5 seconds by the data acquisition system. The 100-second averaged and transient data for velocity measurement were recorded, but only time-averaged data for pressure drop and temperature measurement was recorded.

5.3.1 Velocity measurement

For velocity measurement, the Laser Doppler Velocimetry (LDV) from TSI Inc. was utilized because flow velocity could be determined optically without interfering with the fluid itself. In addition, it is easy to scan several points in every single channel of the test section in contrast to other techniques. For the use of LDV, the standard 18-plate fuel assembly was slightly modified as described in previous Section 5.2. The LDV system used in this study is briefly depicted in Appendix B.1. The single beam on-axis backscattering method was employed to collect the scattered light by particles in flow. The de-ionized water was circulated through the test loop without adding any additional seeding particles because microscopic particles present in de-ionized water was sufficient to generate good quality velocity signal. The LDV beam measuring volume was positioned at the desired points in the channels by the LDV traversing system. The X and Z coordinates were controlled by the X-Z coordinate motor controller with its position on display while the Y coordinate was manually controlled. The positioning of the Y coordinate in the channels is outlined in more detail in Appendix B.1.

Velocity was measured by LDV at the bottom of the calming length and at two elevations of the channels in the plate region of the test section. In the calming length, velocity was measured to investigate the inlet flow condition to the test section. Velocity measurement was undertaken at 49.2 mm ($Z=725$ mm) above the top end fitting and only in half the duct because of its geometrical symmetry in the Y direction. In the plate region, velocity was measured at two elevations (i.e., $Z=1$ and 300 mm) and only in a quarter of the cross-sectional area of the assembly because of its geometrical symmetry in the X and Y directions. At each vertical elevation, velocity measurement was undertaken at 54 points: 6 points in each channel for 9 channels, as is depicted in detail in Fig. 5.8. The velocity profile at $Z=300$ mm was used to investigate the velocity distribution in each channel and the channel-to-channel flow distribution in the test section. This was compared with the velocity profile at $Z=1$ mm to study the influence on the local velocity in the channels by both the bottom end fitting and the sudden expansion of flow area caused by the plate-free duct. A flow rate range from 2.0 to 5.0 kg/s was covered at $Z=1$ and 300 mm.

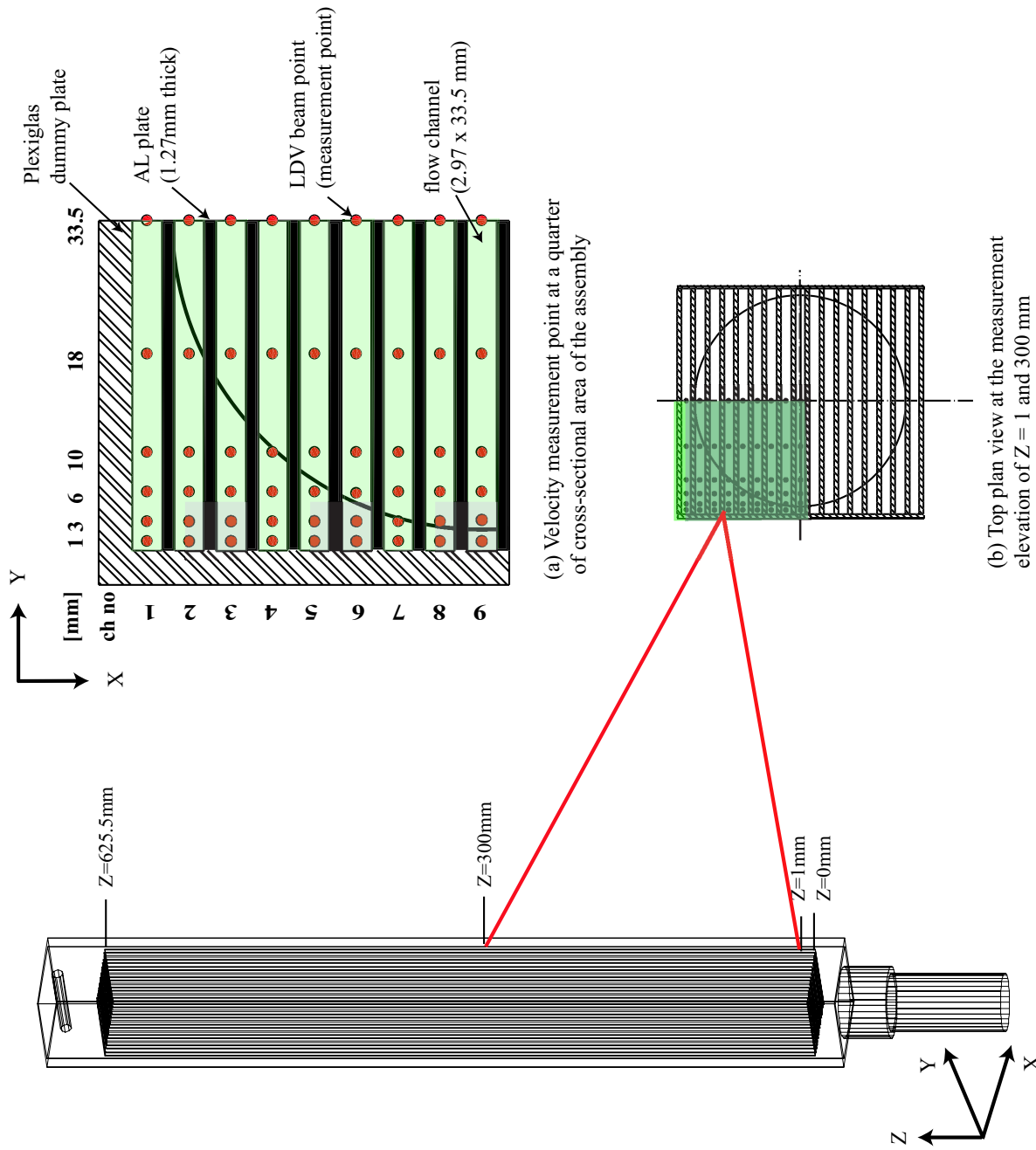


FIGURE 5.8: Schematic of LDV measurement points in the channels. Velocity at only a quarter cross-sectional area at two elevations is measured

5.3.2 Pressure measurement

Pressure was measured by the differential pressure transmitters from Rosemount Inc. in the test section and across the orifice meter. In the test section, pressure measurement was undertaken vertically along the test section as shown in Fig. 5.9. The pressure drop across the plate region (DPFUL), the pressure drop across the bottom end fitting (DPOUT), the total pressure drop across the test section (plate region + bottom end fitting, DPTS), and the absolute pressure in the test section (PRTS) were separately measured by four pressure transmitters.

Pressure taps of 1.524 mm (=0.060 in.) in diameter were drilled into one side of two dummy plates. These taps were located 25.4 mm (=1.0 in.) above the Al plates in the top end fitting, 12.7 mm (= 0.5 in.) below the Al plates in the plate-free duct, and at the bottom end of the bottom end fitting, respectively. These taps were connected to a 3.175 mm (=1/8 in.)-diameter polyethylene tubing to link the pressure transmitters. The water in the pressure tubing was static during the tests, and a density variation along the elevation might be possible due to the temperature difference in between the test loop and the pressure tubing, especially in winter. To compensate for this effect, a cooling jacket was employed. The pressure tap tubing was wrapped by another tubing of larger diameter. The water of the test loop, which was extracted from the surge tank, was circulated through this outer tubing, thereby maintaining a uniform temperature.

All pressure transmitters were deliberately chosen for suitable pressure measurement range depending on the possible range of pressure drops in their application. These transmitters were separately calibrated by Stern Laboratories (SL) to convert measured voltage signal to corresponding pressure difference. These calibration data are attached in Appendix B.2. The calibration constants were input to the pressure conversion equation.

During the preliminary test run, the air bubbles possibly trapped in the pressure tap tubing were removed by the purge valve attached in every transmitter. When the transmitters were equalized, the zero-offset voltage values of all the transmitters were initially measured and recorded for use in the pressure conversion equation. The

measured voltage signal from the transmitters can be converted to pressure by the Eq. (5.2).

$$P = A + B(V - V_{\text{offset}}) + C(V - V_{\text{offset}})^2 \quad (5.2)$$

where P =pressure, [Pa]; V_{offset} =measured zero-offset voltage when the transmitter is equalized, [V]; V =measured voltage signal from the transmitter, [V]; A, B, C =SL calibration constants.

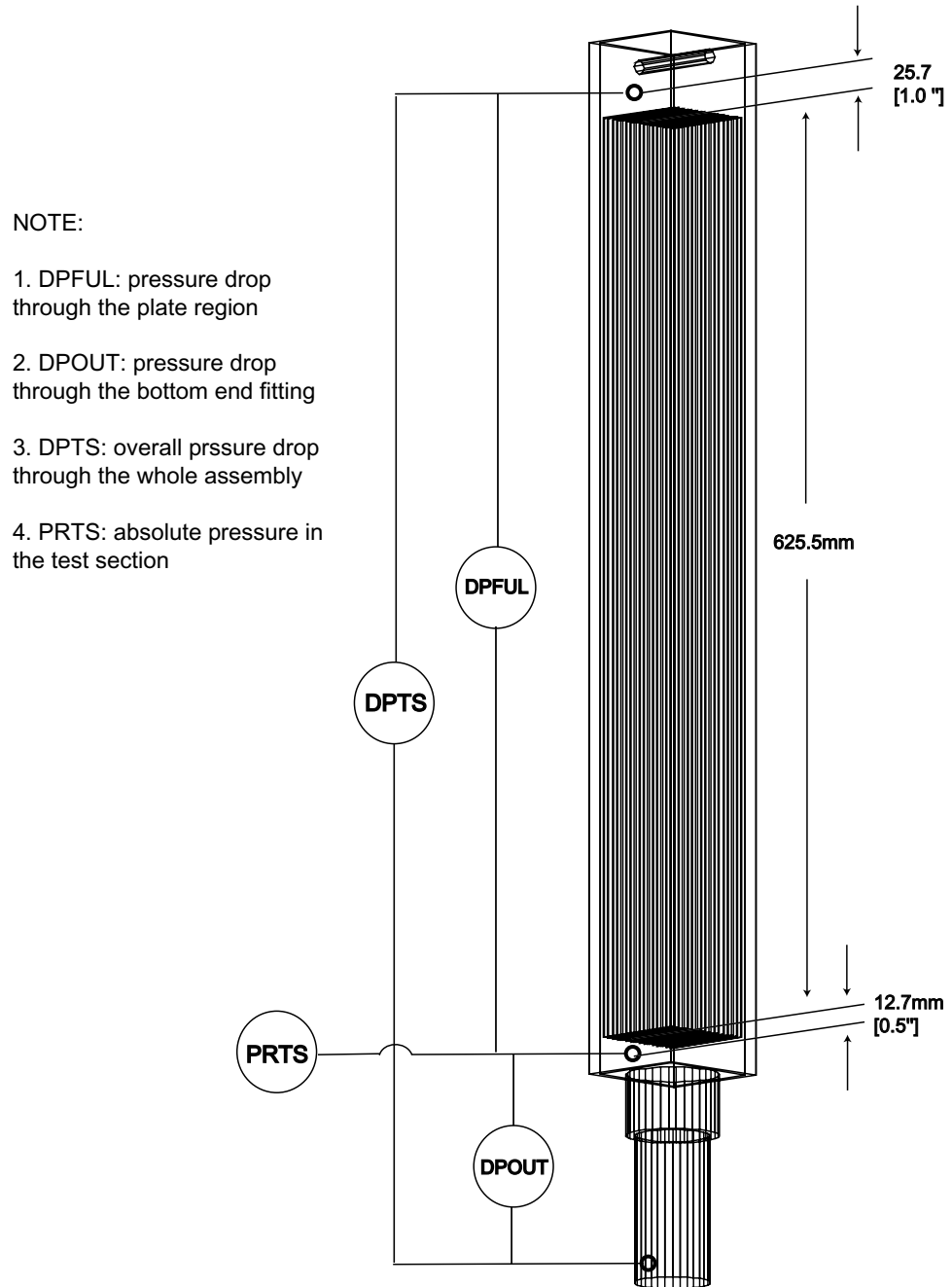


FIGURE 5.9: Pressure drop measurement and location of the pressure taps in test section

5.3.3 Flow rate measurement

A nominal flow rate through the MNR flow simulator was set by the combination of circulating pump, flow orifice, and flow control valve. The pressure drop across the orifice meter was measured by the differential pressure transmitter. The calibration of this orifice meter with the pressure transmitter was undertaken by SL to allow direct conversion from voltage signal to pressure drop and flow rate. Its calibration data is attached in Appendix B.3. The flow rate was calculated as shown in Appendix B.3. Here the 36.817 mm (=1.4475 in.)-diameter orifice plate with D and 1/2 D pressure taps was used. The data of 5-second averaged flow rate was updated on-line on a video screen as described in Section 5.5. Hence, the flow rate through the test loop, observed on the video screen, could be set at the desired rate during the preliminary test run by simply adjusting the flow control valve.

5.3.4 Temperature measurement

Temperature was measured using type T thermocouples at three locations: upstream of the calming length (T1), at the exit of the bottom end fitting (T2), and at the surge tank (T3). The calibration check for these thermocouples was undertaken by SL. The SL reference junction temperature was electrically simulated at 65.56 °C(=150 °F). The measured output voltage signals from the thermocouples were converted from millivolts to temperature by the equation of 7th order inverse polynomial based on the standard table developed by the National Institute of Science and Technology (NIST):

$$T(^{\circ}\text{C}) = f(mV + A) \quad (5.3)$$

where mV is measured thermocouple output voltage, and A is the equivalent mV value at the SL reference temperature, 65.56 °C. During the preliminary test run, the zero-offset values of these thermocouples (i.e., $A=2.7110$ mV) were initially measured and recorded for the temperature conversion equation.

The temperatures of T1 and T2 were to detect the vertical temperature variation along the 18-plate assembly flow simulator as shown in Fig. 5.4. The additional temperature of T3 was to evaluate the temperature variation through the test loop

with T1 and T2 in Fig. 5.6. Three voltage signals from these thermocouples were input through the conditioning device to the data acquisition system for temperature conversion. The data of 5-second averaged temperature was updated on-line on a video screen as described in Section 5.5. Hence, the temperature could be controlled within the desired range of 30 ± 1 °C using the cooling jacket.

5.4 Experimental Reynolds number

Experiments were conducted changing the flow rate from 2.0 to 5.0 kg/s while the temperature was maintained at 30 °C. The flow rate was adjusted at nominal values by the flow control valve with the pump, while the temperature was adjusted by the cooling tap water loop as briefly described in previous Sections. The Reynolds numbers through the test section can be calculated:

$$Re = \frac{\rho U_n D_h}{\mu} \quad (5.4)$$

where $\rho=995.7\text{kg/m}^3$ density of water at $T = 30$ °C, $P=101.3$ kPa; $\mu = 7.9735 \times 10^{-4}$ N s/m² viscosity of water at $T = 30$ °C, $P=101.3$ kPa; U_n =nominal average velocity. The pressure change has little influence on the change of the density and the viscosity of water (liquid), and the pressure in test section varies possibly only from 121.1 to 166.2 kPa. Hence, the density and the viscosity of the water in the test loop were evaluated at the temperature of 30 °C and the atmospheric pressure of 101.3 kPa. Nominal average velocity, $U_n = \frac{M}{\rho A_{tot}}$ with the assumption of uniform flow distribution through the 17 channels in the test section: A_{tot} =sum of the flow area of the 17 channels in the test section and M =flow rate through the test section. Hence, nominal average velocity is the same through all the channels at given flow rate. The Reynolds numbers for all the experimental cases are listed in Table 5.2.

5.5 Data acquisition system

Data acquisition software was developed by SL and its system is depicted in block diagram in Fig. 5.10. Nine measured experimental variables were processed via this

TABLE 5.2: Reynolds numbers for all the experimental cases

M[kg/s]	T[°C]	Q[L/s]	U_n [m/s]	Re
2.0	30	2.01	0.5939	4218.1
2.5	30	2.51	0.7424	5272.6
3.0	30	3.01	0.8908	6327.1
3.5	30	3.52	1.0393	7381.6
4.0	30	4.02	1.1878	8436.1
4.5	30	4.52	1.3363	9490.6
5.0	30	5.02	1.4847	10545.2

data acquisition system. Individual instrument signals were connected via conditioning devices to a Digital Equipment Corporation computer (DEC, VAX 4000), which has 120 CIP/RTP channels scanners and 12-bit A/D converter. In all, three temperature measurements (T1, T2, and T3), one velocity measurement, and five pressure measurements (DPFUL, DPOUT, DPTS, PRTS, and DP from orifice meter) were interfaced. The programs for data acquisition and processing were manipulated via two remote terminals, which were connected directly to the DEC computer. Terminal 1 was connected to a laptop computer and terminal 2 was connected to a desktop computer. At the terminal 1, LDV setting and measurement point coordinates were input to the laser program for every test. This laser program scans transient velocity, pressure drops and temperatures at 10 Hz for 100 seconds, and calculates the average value of 1000 samples of each signal. The transient and time-averaged data of velocity were only recorded, whereas the time-average data of pressure drops, temperatures and flow rate were stored. At terminal 2, the setup program was executed to scan the velocity, temperature and pressure at 10 Hz for 5 seconds, and calculate the 5-second average of velocity, pressure drops, flow rate and temperatures. This 5-second steady-state data was updated on-line on both a video screen and a monitor in terminal 2.

For every test, the following detailed information of time-averaged experimental variables and LDV settings was printed out and stored: three temperatures, velocity

and its frequency, flow rate, measurement point coordinates, LDV setting parameter, and time of measurement.

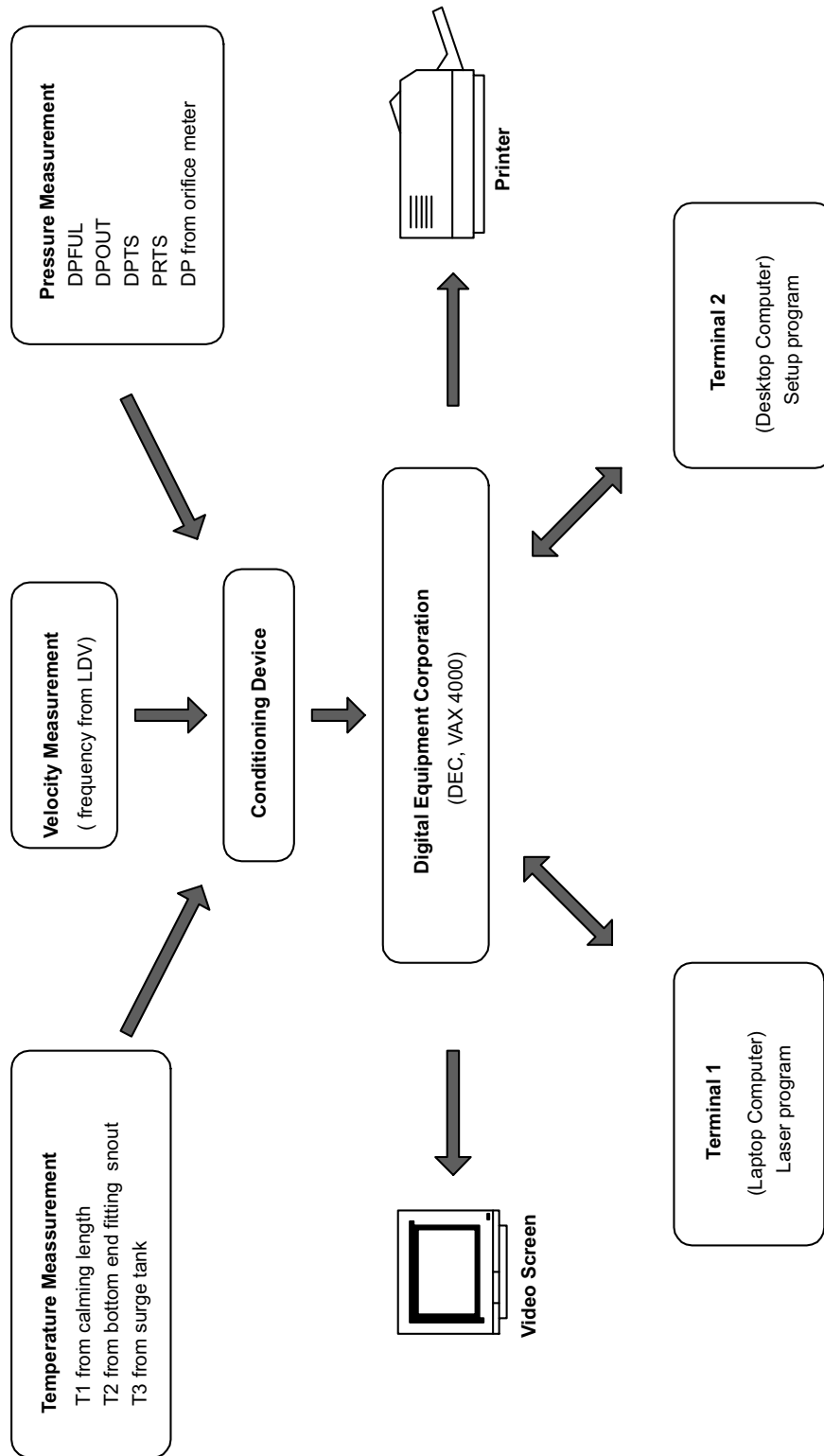


FIGURE 5.10: Schematic of data acquisition system. 3 temperature, 5 pressure drop, and 1 velocity in test section are measured, processed, and recorded through data-acquisition system

5.6 Flow visualization

For flow visualization, direct flow visualization (DFV) by a chemical indicator technique was employed. A chemical indicator is normally an organic substance whose color depends on the H_3O^+ concentration in its containing medium [20, 21, 29]. An indicator changes rapidly from an acid color to an alkaline color within narrow range of H_3O^+ concentration, which is conventionally expressed in pH ($\text{pH} \equiv -\log[\text{H}_3\text{O}^+]$). Flow behavior can be monitored by means of visual contrast. This can also be directly observed by human eye, and photographed or videotaped. This DFV technique is very simple and cost-effective for the present study.

The schematic of DFV system in the present study is shown in Fig. 5.11. Bromo Thymol Blue (BTB) solution was used as a chemical indicator. BTB of 5 g was dissolved in 1 L water, and this solution of 250 mL was added in the surge tank. Acid solution and alkali solution were prepared with 1 N NaOH and 1 N HCl, respectively. These solutions were contained in the C-PVC pipe cylinder of injection system. This injection system was connected to the 5 psig. compressed air to inject acidic or basic solutions into the pump suction, to provide flow visualization through the test section. By injecting NaOH or HCl solution, the color of the BTB dissolved in the fluid could be reversed from “blue” to “yellow”, and vice versa (yellow for acidic solutions $\text{pH} < 6$, and blue for basic solution $\text{pH} > 7.5$). A 2 m-diameter parabolic dish was installed behind the test section to provide uniform lighting for clear flow visualization. A 2 kW light source was directed at the dish to provide the background lighting. A video camera was used to record the flow behavior in the 18-plate assembly simulator during the test.

Flow visualization was undertaken by changing the flow rate from 0.8 to 1.8 kg/s. Flow behavior was recorded in the calming length, in the top end fitting, in the plate region, and in the plate-free duct in between the plate region and the bottom end fitting. This flow visualization through the assembly is discussed in chapter 9.

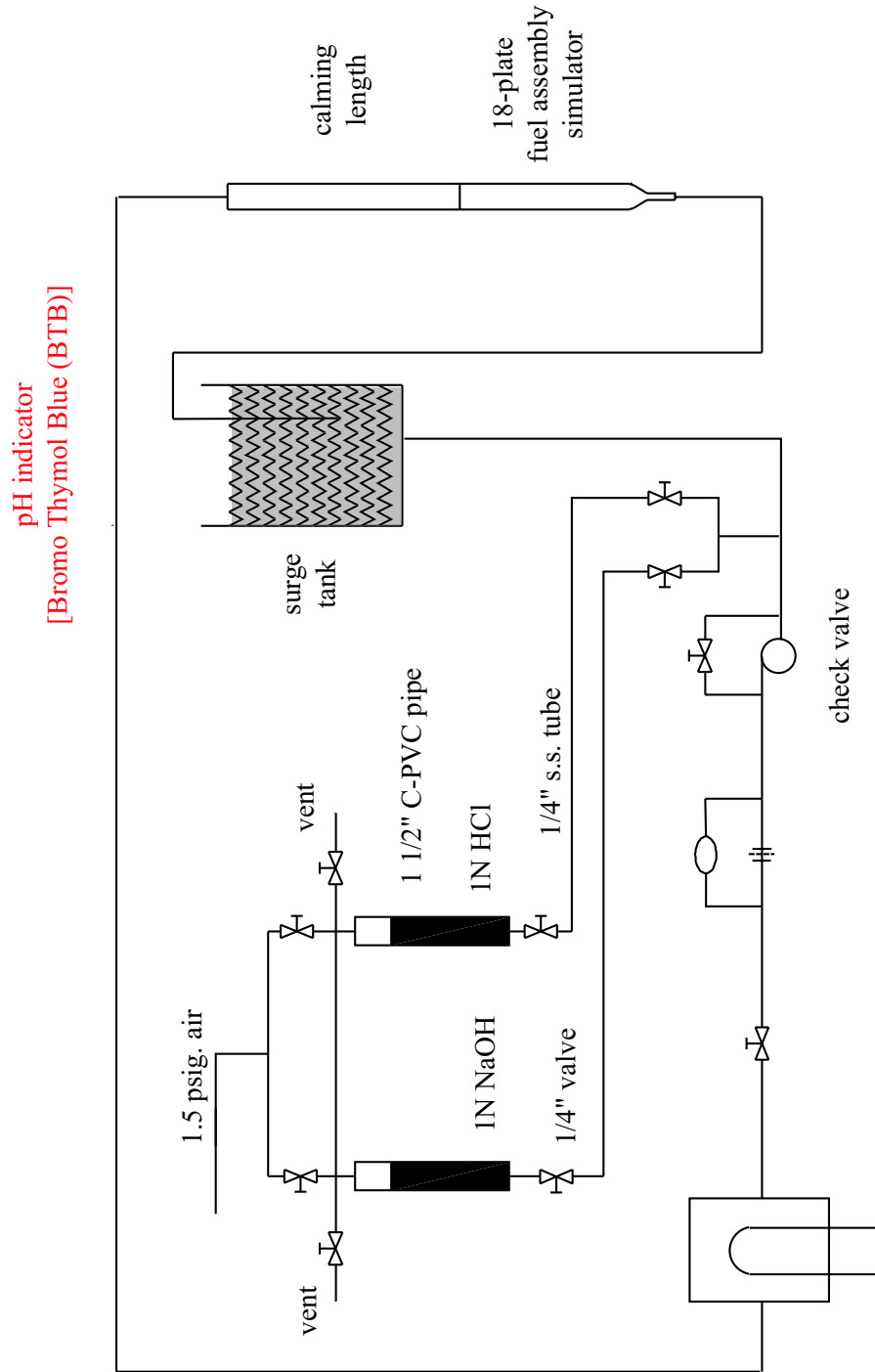


FIGURE 5.11: Schematic of flow visualization by Direct Flow Visualization technique in 18-plate assembly flow simulation

Chapter 6

Velocity profile and flow distribution in an 18-Plate assembly

To investigate the hydraulic characteristics of coolant flow in one of the standard 18-plate assemblies in the central region of the MNR core, the standard assembly was slightly modified replacing curved plates with flat ones, and an additional calming length duct was inserted to simulate the inlet flow condition to the top end fitting (see chapter 5). The test loop was set up with the calming length duct sitting on the simulated 18-plate assembly (test section). The experiment was undertaken changing flow rate through the test loop from 2.0 to 5.0 kg/s (i.e., $U_n=0.59\text{--}1.48\text{m/s}$, where U_n is bulk velocity through individual channels). Velocity measurement using a single beam Laser Doppler Velocimetry (LDV) was conducted at the bottom of the calming length ($Z=725\text{ mm}$) and at two elevations of $Z=1$ and 300 mm in the channels as shown Fig. 5.8.

6.1 Control of flow rate and temperature through test loop

The temperature and the flow rate through the test loop were controlled at specific nominal values during measurement. During preliminary testing, the flow rate and the temperature ($T = 30\text{ }^\circ\text{C}$) were set. The flow rate was adjusted using the control valve, whereas the temperature was raised to the nominal value by using the electric heater and then maintained at that value using the cooling tap water loop, which is to remove the pumping heat. Here the temperature was controlled within the range of $T = 30 \pm 1\text{ }^\circ\text{C}$ because the temperature variation of only $\pm 1\text{ }^\circ\text{C}$ could have little influence on water properties (i.e., density, and viscosity) and thus Reynolds number.

Both flow rate and temperature were controlled at the nominal values as described in Section 5.5.

Fig. 6.1 shows an example of the flow rate and the temperature variation during measurement at $M=3.0$ kg/s and $T = 30^\circ\text{C}$. Data was recorded at 10 Hz for 100 seconds. Hence, each data point represents a 100-second averaged value (i.e., 1000-sample-averaged value). It is shown that the flow rate and the temperature were controlled precisely around their specified values during measurement. The flow rate was maintained around the mean value of 3.01 kg/s with 0.0461% standard deviation, whereas the temperature was maintained around $T = 30.02^\circ\text{C}$ with 1.02%. The control valve with the pump performed accurate control for the flow rate through the test loop. The simple cooling tap water loop was sufficient for the temperature control possibly because the pumping heat is small compared to the heat capacity of the loop water. The slow temperature increase by the pumping heat can be easily removed by the cooling tap water loop. Therefore, the mass flow rate and the temperature through the test loop were precisely controlled around the specified nominal values during measurement at $M=3.0$ kg/s.

The variation of the flow rate and the temperature for all the experimental conditions are shown in Fig. 6.2 and 6.3, respectively. Here both flow rate and temperature were initially set at their nominal values before measurement. Each data is recorded at the sampling rate of 10 Hz for 5 seconds and averaged. It is shown that the flow rates were accurately controlled around the specified nominal values for every experiment at $M=2.0$ – 5.0 kg/s. The magnitude of error for the flow rate control is less than 0.7%. On the other hand, the temperature was also precisely controlled within its projected range. Its magnitude of error based on the absolute temperature is very small and could have little influence on the water properties. In addition, it is clearly observed that the little temperature difference exists through the test loop (i.e., T1 to T3). As previously explained, this may be because the additional heat addition by pumping is relatively small compared to the heat capacity of the total loop water. This also suggests that the cooling tap water loop is sufficient for the temperature control through the test loop during measurement. Thus it can be concluded that the flow rate and the temperature were accurately controlled around their nominal values in every experiment at $M=2.0$ – 5.0 kg/s.

In conclusion, the flow rate and the temperature through the test loop were controlled around their specified values from the individual case of $M=3.0$ kg/s and all the experimental cases. The flow control valve with the pump could control the flow around the nominal flow rate, while the cooling tap water loop controlled the temperature to the allowable limit of temperature variation (± 1 °C).

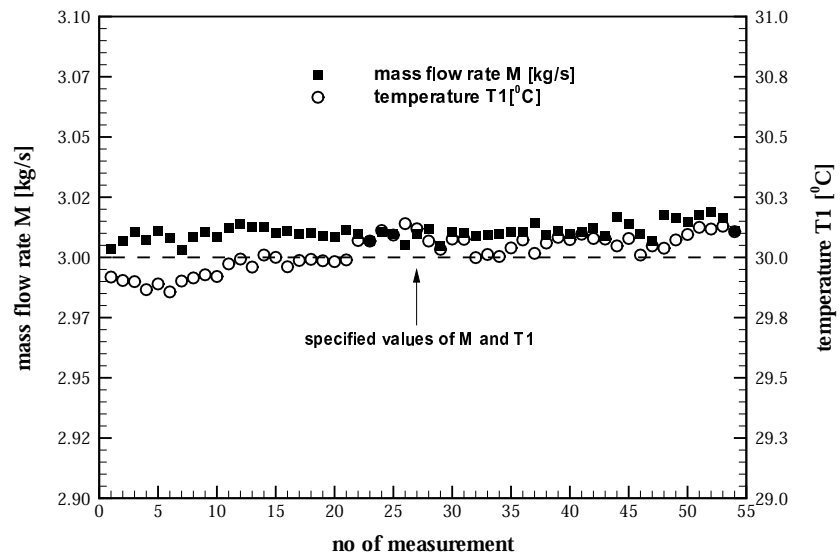


FIGURE 6.1: Variation of the flow rate (M) and temperature (T) during the measurement at $M=3.0$ kg/s and $T = 30^\circ\text{C}$

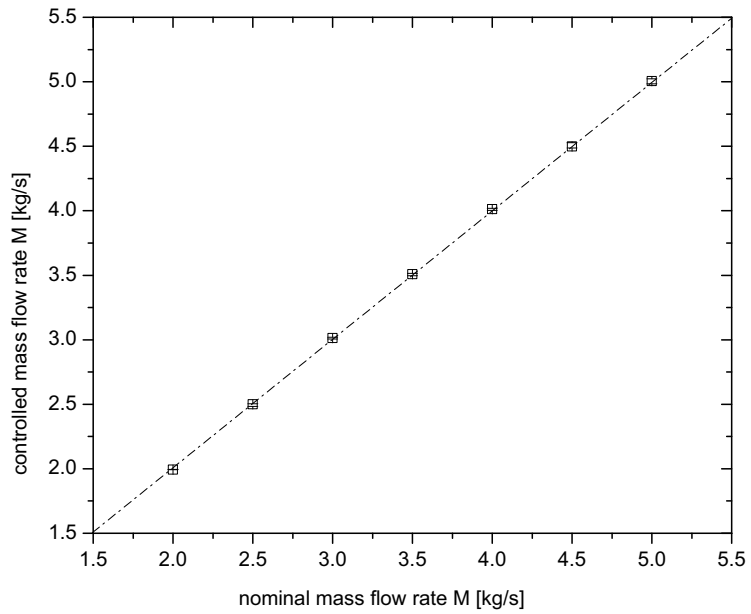
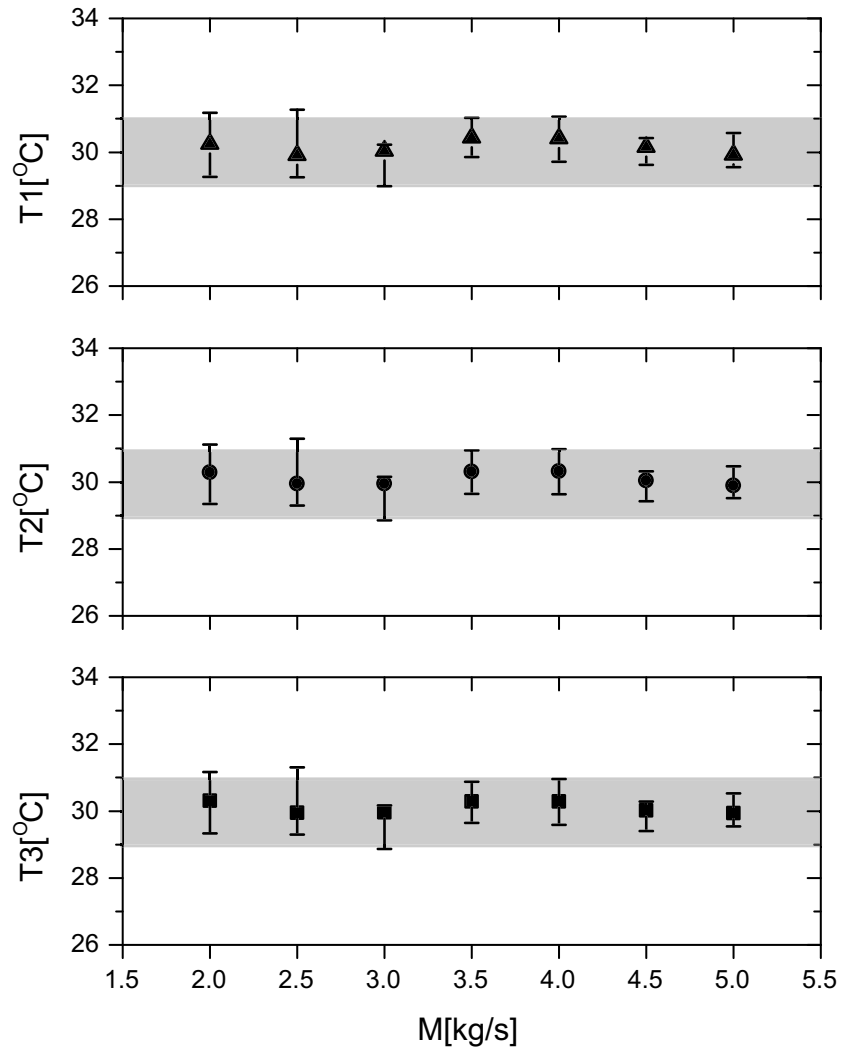


FIGURE 6.2: Flow rate variation during the measurement at $M=2.0$ – 5.0 kg/s

FIGURE 6.3: Temperature variation during the measurement at $M=2.0-5.0$ kg/s

6.2 Velocity

Axial velocity was measured using a single beam Laser Doppler Velocimetry (LDV) by changing the flow rate from $M=2.0$ to 5.0 kg/s. Velocity measurement was undertaken at the bottom of the calming length duct ($Z=725$ mm), and vertically at two elevations of $Z=1$ and 300 mm from the bottom ends of the plates in the channels. Axial velocity was scanned at 10Hz or 20Hz for 100 seconds by LDV. The typical signal of raw voltage of the transient velocity in the channels at $M=2.5\text{--}4.5$ kg/s is shown in Fig. 6.4. Note that the velocity in this figure was scanned at 10 Hz. It is observed that the voltage signals are fluctuating and agitated regardless of their measurement points in the channels for all the cases. The Reynolds number corresponding to the flow rate ranges from 5272.6 to 9490.6 in the channels (see Table 5.2). Therefore, it can be deduced that the flow in the channels are slightly or completely turbulent steady flow for the experiment conditions. Hence, the average of axial velocity in the channels, U and turbulent intensity, T_u can be calculated simply by integrating transient velocity over the given time period and dividing it by that period [13].

$$U = \frac{1}{t} \int_0^t u dt \quad T_u = \left(\frac{1}{t} \int_0^t (u - U)^2 dt \right)^{1/2} \quad (6.1)$$

where, u =local transient velocity, t =time period of averaging, U =average of axial velocity, $(u-U)$ =fluctuating term of velocity.

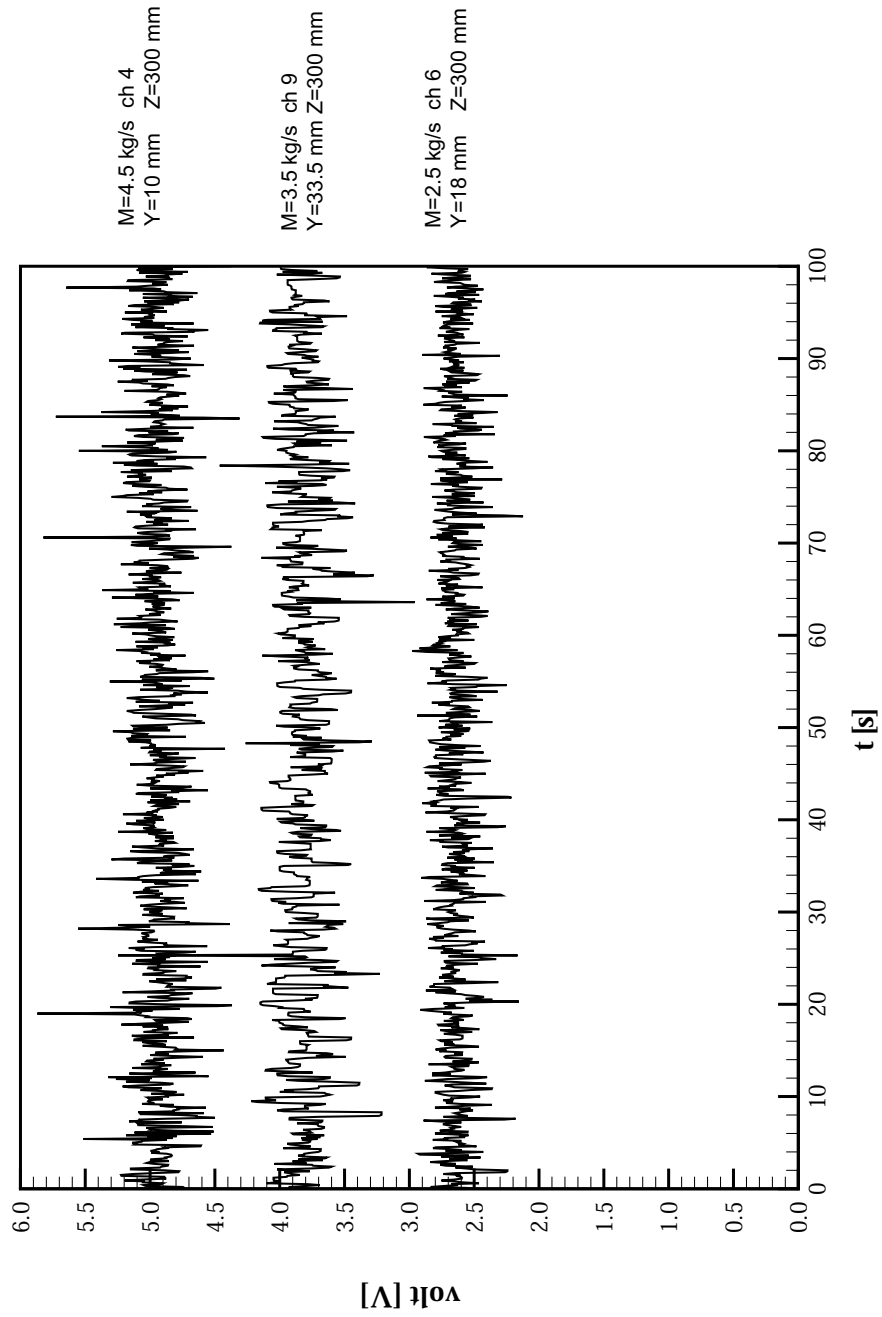


FIGURE 6.4: Typical signal of raw voltage of the transient velocity in the channels

6.3 Simulation of inflow to the calming length

The present experiment was aimed at investigating the hydraulic characteristics in an 18-plate assembly in the central region of the MNR core. Hence, the additional calming length was inserted on top of the simulated 18-plate assembly to simulate the inlet flow condition to the top end fitting of the 18-plate assembly in the central region of the MNR core (see Section 5.2). In order to examine this simulation of the inlet flow to the top end fitting, axial velocity measurements were undertaken at 66 points in the calming length duct at $Z=725$ mm (see Fig. C.1). It is only half of the cross-sectional area of the rectangular duct due to its geometric symmetry and velocity measurement difficulty in the other half from excessive light reflection of the laser beam by the other side plate.

6.3.1 Velocity distribution in the bottom of the calming length

Fig. 6.5 shows the dimensionless velocity profile at $Z=725$ mm in the bottom half of the calming length at $M=3.0$ kg/s. The velocity in the core region of the duct is high and nearly uniform. However, it is decreased significantly toward the wall due to the viscous effect from the plate's wall. The velocity contour of the figure (a) shows that the velocity field is not completely symmetric in the X-direction but it is slightly deformed to the east. This may be a result of the 90° change of the stream direction from the test loop piping to the circular tube just above the calming length duct in the northwest-west direction and from sudden flow expansion from this smaller circular tube to a larger rectangular duct (Section 5.2). The effects of diffuser and bellmouth from 90° flow-stream direction change may lead to flow separation and eddy flow formation in both inner walls and outer walls of the elbow [11], which should disturb significantly the flow downstream. The combination of these phenomena may lead to the considerable deflection of the velocity profile upstream in the calming length. However, the calming length appears to be too short for this disturbed flow to be completely redeveloped into the duct velocity profile downstream. It is only $4.5D_{h,CL}$ ($=617.7$ mm) at the velocity measurement points ($Z=725$ mm); here $D_{h,CL}$ is the hydraulic diameter of the calming length duct. Hence, the velocity profile is shown

slightly deformed in one direction.

The measured average velocity is 0.645 and 0.634 m/s in the east-south 1/4 region and the west-south 1/4 region of the duct, respectively; the average velocity in each region is calculated by Eq. C.1. Their difference is only 1.76%. The difference of the local velocities between at the points in the east-south region and at their geometrically corresponding points in the west-south region is also only less than 3% in the figure (c). It is clearly shown that all the profiles in the X-direction at the Y-direction measurement points are considerably symmetric except at Y=1 mm where the slight velocity deflection is observed. Hence, it can be concluded that the velocity distribution is nearly symmetric in the X-direction despite a slightly deflected profile.

The velocity was measured only in half of the duct in the Y-direction. The averaged velocity in the measured half duct is 0.644 m/s, whereas the nominal average velocity is anticipated to be 0.639 m/s in the entire duct. Note that the nominal average velocity in the calming length duct, $U_{n,CL} = \frac{M}{\rho A_{tot,CL}}$ where M is nominal mass flow rate, ρ fluid density at $T = 30^\circ\text{C}$, and $A_{tot,CL}$ total flow area in the calming length duct. The measured average velocity is only 0.78% higher than its nominal value. This suggests that the flow rate through the unmeasured half duct should be close to that value in the measured half duct. In addition, based on the geometrical symmetry of the calming length duct, which led to the symmetric velocity distribution in the X-direction, the velocity distribution in the Y-direction can be also assumed to be symmetric. Therefore, it can be concluded that the velocity distribution be also symmetric in the Y-direction.

In summary, the velocity distribution in the bottom of the calming length duct is shown nearly symmetric in the X- and Y-directions at M=3.0 kg/s. The extent of the velocity profile deflection is very small and its magnitude should be further reduced downstream just above the test section.

6.3.2 Turbulent intensity in the bottom of the calming length

Turbulent intensity, Tu_{CL} at the bottom of the calming length is shown in Fig. 6.6. Here the turbulent intensity data along the X-direction at Y=1 mm was excluded to

observe more clearly the turbulent intensity profile in the calming length because of its relatively high value of 18 to 29%. This arises possibly from the difficulty in locating the LDV measurement point exactly at $Y=1$ mm as described in Appendix C.2. The turbulent intensity distribution in the core region of the duct is relatively high and uniform, ranging approximately from 9 to 14%: relatively low in the central region and relatively high near the wall plates. However, even in almost immediate proximity of the sidewalls (i.e., $X=1$ mm along the Y -direction) turbulent intensity is only slightly higher than that in the central region. This may be due to the near attainment of the fully developed turbulent velocity profile in the bottom of the calming length duct (at the velocity measurement points) and the extremely small relative ratio of the surface roughness of Plexiglas side plates. In summary, the turbulent intensity distribution in the bottom of the calming length is slightly high but considerably uniform except at $Y=1$ mm along the X -direction. This suggests that the considerably disturbed flow from the upstream of the calming length is nearly fully-developed in its bottom.

6.3.3 Summary

The velocity distribution at the bottom of the calming length duct is shown nearly symmetric in the X - and Y -directions. Its turbulent intensity distribution is also considerably uniform. Thus, the flow, considerably disturbed from the test loop piping to the calming length, may be nearly fully-redeveloped in its bottom. This suggest that the method of the calming length duct sitting on the test section to simulate the inlet flow to the top end fitting of the central assemblies in the MNR core works successfully. In addition, the flow behavior in the entire calming length is visualized and its result is discussed in Section 9.1.

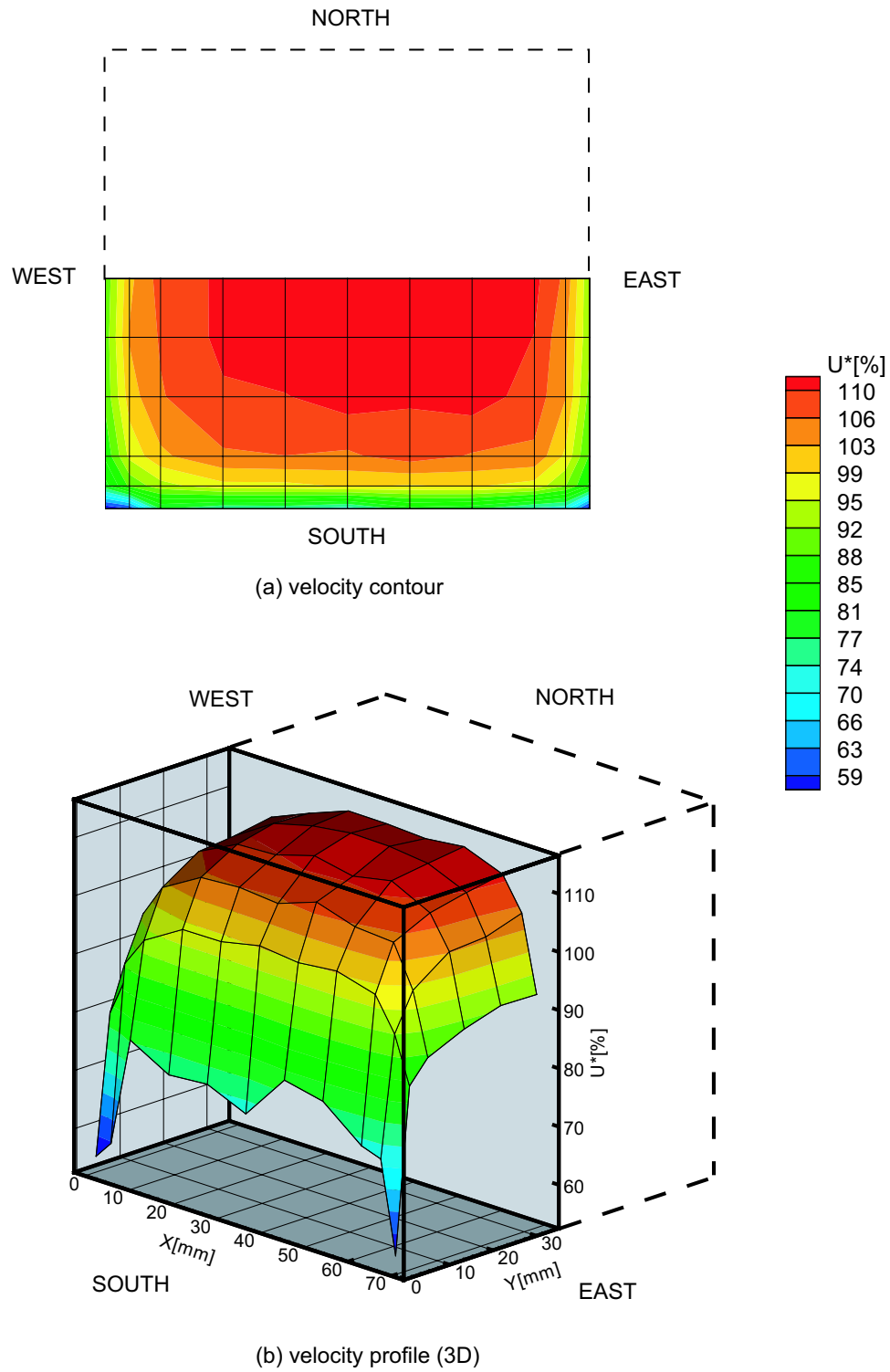


FIGURE 6.5: Dimensionless velocity profiles in calming length at $Z=725$ mm at $M=3.0$ kg/s

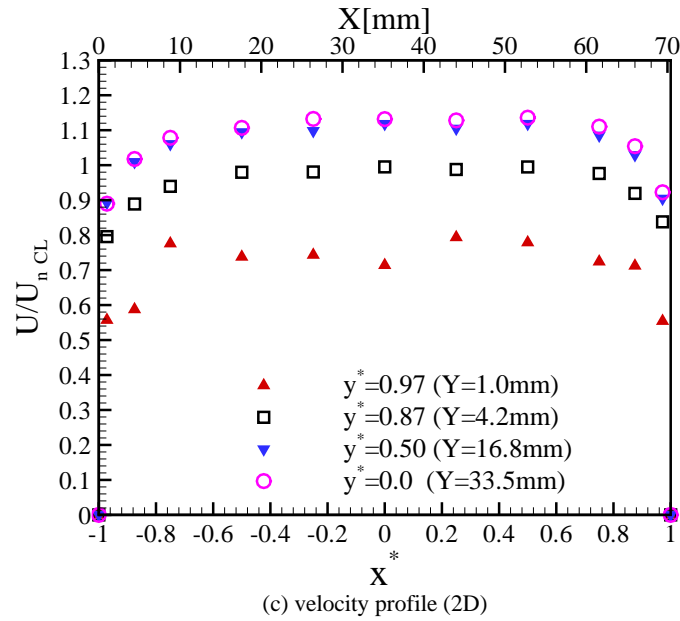


FIGURE 6.5: Cont'd

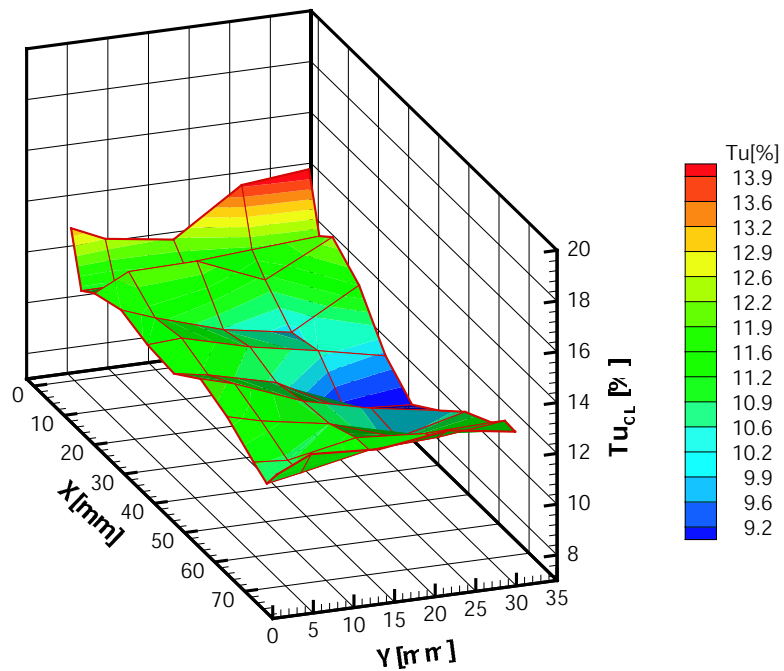


FIGURE 6.6: Turbulent intensity distribution in the calming length at $Z=725$ mm at $M=3.0$ kg/s. Note that Tu_{CL} at $Y=1$ mm along the X -direction (18 to 29%) is excluded

6.4 Vertical axial velocity distribution along the channels

The axial velocity was vertically measured at the thickness-wise center at the various width-wise points in the channels in the test section. The axial velocity was averaged from the transient velocity by Eq. (6.1). For the measure of the flow development in the channels of high aspect ratio in the assembly, blockage factor, B is used as suggested by Klein [22].

$$B = 1 - \frac{U_n}{U} \quad (6.2)$$

where, U_n =nominal average velocity (bulk velocity) at given flow rate (see Table 5.2), U =measured velocity at the thickness-wise center in each channel. The blockage factor was plotted against normalized channel length in Fig. 6.7. The development of the axial velocity profiles both in the present experiment and in Yu's numerical simulation shows the existence of three main regions along the channels: the entrance region, the fully-developed region, and the exit region.

6.4.1 Entrance region

In the entrance region in channel 6 at $M=2.0$ kg/s and in channel 2 at $M=3.0$ kg/s at $Y=33.5$ mm of the present experiment (figure (a)), the blockage factor increases gradually until the boundary layers merge at the thickness-wise center in the channels. It reaches a maximum around $z^*=15$, which is significantly less than 35–40 D_h for pipe flow [22]. Then it decreases slightly and levels off downstream around $z^*=18$ –22 where the fully developed flow may be considered to be attained. Therefore, the hydrodynamic length for both cases can be taken as about $21D_h$. This is shorter compared to 25–100 D_h for turbulent flow. It may be due to the very sharp-edged entrance configuration of the assembly channels in the test section and the high turbulent upstream flow across the inlet of the test section (i.e., $Tu_{CL} \approx 9$ –14% in the bottom of the calming length in Section 6.3.2) [12]. Therefore, the laminar-turbulent transition may occur at relatively low Reynolds number (i.e., $Re_{crit} \approx 2000$). The boundary layers from the leading edge of the channel inlet grow faster. Thus the fully developed flow may be attained earlier. The entrance length, L_e can be calculated by

Eq. 4.2 for turbulent flow.

$$L_e = 18D_h \quad \text{at } M=2.0 \text{ kg/s (Re=4218.1)}$$

$$L_e = 19D_h \quad \text{at } M=3.0 \text{ kg/s (Re=6327.1)}$$

These values are very close to the experimental result of $L_e \approx 21D_h$.

Fig. 6.7 (b) shows the development of the axial velocity profile from Yu's numerical simulation [6] at $M=3.0$ to 5.0 kg/s ($\text{Re}=5151\text{--}8585$). The profiles in the entrance region show slightly different trend from the present experiment. The "undershoot" and "overshoot" of the profile after the maxima are observed. However, the maximum B value is larger at the lower flow rate (Re), which agrees well with the result of Klein [22]. The locations of the maxima are also slightly different from the present experiment and the result of Klein; they are observed almost at immediate downstream of the channel inlet. The fully developed flow is attained around $z^*=20$ (or $L_e = 20D_h$) for all the cases. This agrees accurately with the present experiment.

For laminar flow, the entrance length in the channels of the standard 10-plate assembly was measured at $M=0.03$ to 0.40 kg/s ($\text{Re}=8 \sim 1073$ or $U_n=0.008 \sim 0.104$ m/s) by Rummens [4]. It was shown that the flow was fully developed within $39D_h$ (22cm from the leading edges of the fuel plates in the channels) for all the cases. However, L_e was not exactly determined. Its value is obviously larger than those of the present experiment and Yu's numerical simulation. This is reasonable because the entrance length for laminar flow is slightly longer than that for turbulent flow in the channels.

The axial velocity distribution in channel 9 at $M=3.0$ kg/s and at $Y=33.5$ mm shows a different trend from the others in Fig. 6.7 (a) in that a profile maximum is not observed. The velocity is increased downstream of the channel entrance and then quickly stabilized toward the fully developed profile. This may be associated with the upstream flow obstruction by the handle, which is located 38.1 mm directly above the inlet of channel 9. The handle should disturb the nearly uniform flow developing from the calming length (Appendix D). It may generate a disorganized wake downstream of the handle, similarly to flow past a circular cylinder [14], which enters channel 9 (see Fig. D.1). Hence, the flow right above the inlets of channels 8 to 10 should be not uniform but highly unsteady and irregular. This flow disturbance may enhance the

boundary layers from the leading edge of the channel walls to be quickly developed into the central region of the channel without long core-region velocity acceleration. Therefore, the boundary layer merger may be attained quickly, which leads to early stabilization toward fully developed flow without the profile maximum observed in the other channels.

In summary, both present experiment and Yu's numerical simulation are in a good agreement for predicting the hydrodynamic entrance length along the channels. The entrance length was about $21D_h$ and is close to that predicted by a simple correlation for turbulent flow. However, this is slightly shorter than that for turbulent pipe flow possibly because of the abrupt entrance configuration of the channels and the relatively high turbulent intensity upstream from the calming length. On the other hand, the flow in channel 9 is quickly fully-developed without the profile maximum possibly due to the wake past the handle (handle effect).

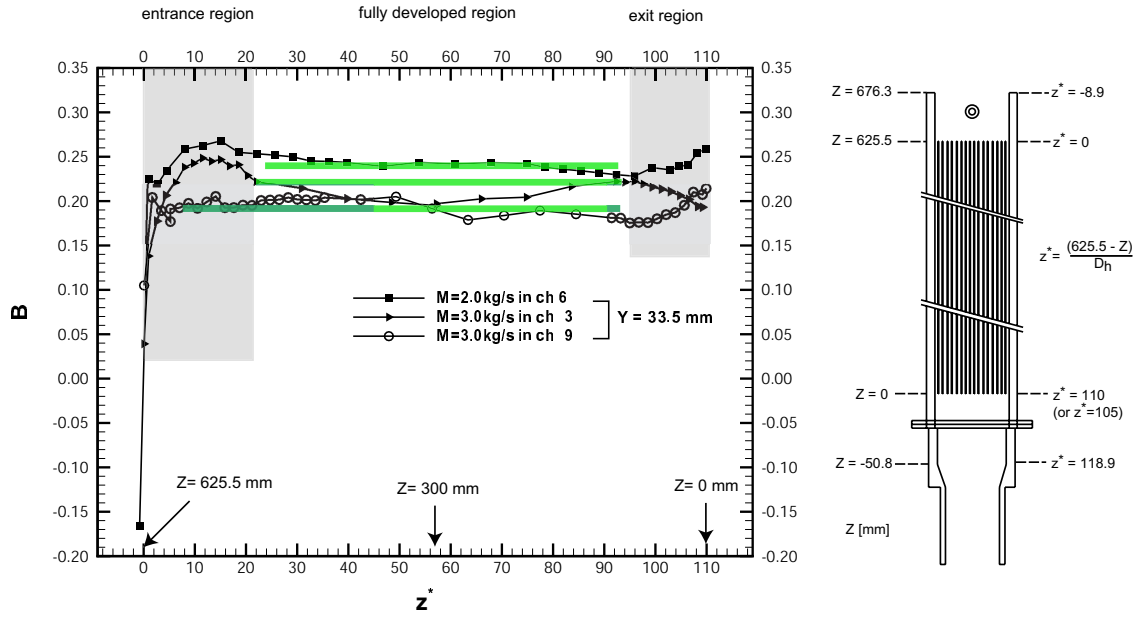
6.4.2 Fully-developed region and exit region

A fully developed flow is attained downstream after the entrance length in the channels. The velocity profile remains relatively constant in the fully developed region in both cases except for channel 3 where the slight decrease and then increase of the velocity down to the exit region is detected in the present experiment. This unexpected profile in channel 3 may result from the error of locating the measurement points precisely at its thickness-wise center in the width-wise direction (Appendix C.2). The velocity profiles show a slightly different trend near the channel exit in both cases. The exit region length is comparatively different; $12D_h$ in the present experiment, but $1D_h$ in Yu's numerical simulation. The present experiment shows that the velocity is slightly increased in the central channels (i.e., channels 6 and 9) whereas the velocity is decreased in the outer channels (i.e., channel 3). This may result from the combined exit effect of sudden expansion in the plate-free duct and abrupt contraction in the bottom end fitting (see Fig. 4.4 and 4.5). However, Yu's numerical simulation shows that the velocities in both outer channel 2 and central channel 8 only near the channel exit are significantly decreased. To examine this phenomenon further, the velocity profile at the fully developed region ($Z=300$ mm)

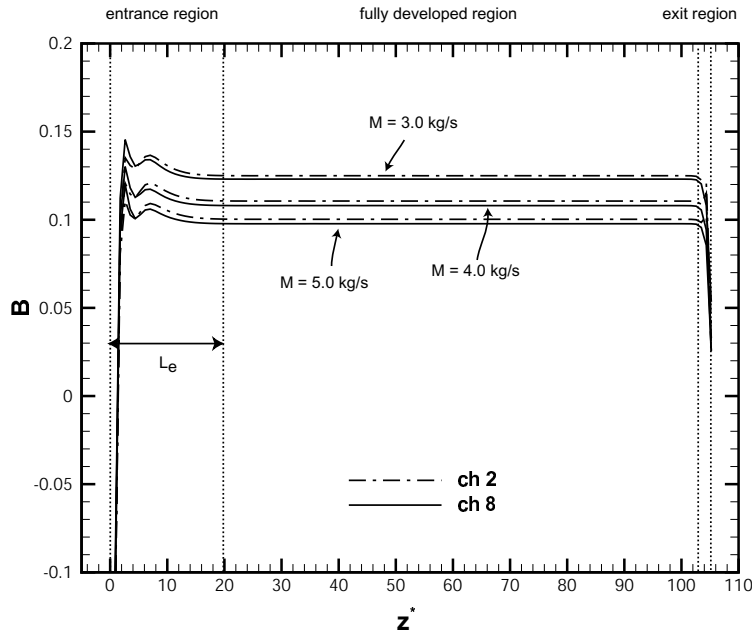
will be compared to that near the channel exit ($Z=1$ mm) in Section 6.6.2, and the visualization of the flow behavior in the plate-free duct is discussed in Section 9.3.

6.4.3 Summary

The development of axial velocity profile shows the existence of three main regions along the channels: the entrance region, the fully-developed region, and the exit region both in the present experiment and in Yu's numerical simulation. In the entrance region, the fully developed flow is attained approximately around $z^*=21$ (or $L_e = 21D_h$) in the present experiment. This is in good agreement with the predictions of a simple correlation and Yu's numerical simulation. The velocity profile remains relatively constant in the fully developed region, but is slightly influenced near the channel exit by the exit effect. In addition, channel 9 shows slightly different flow development in the entrance region from channels 3 and 6 possibly due to the handle effect.



(a) present experiment



(b) Yu's numerical simulation

FIGURE 6.7: Development of the axial velocity profiles with non-dimensionless channel length from the channel inlet

6.5 Symmetry of velocity distribution through the assembly channels

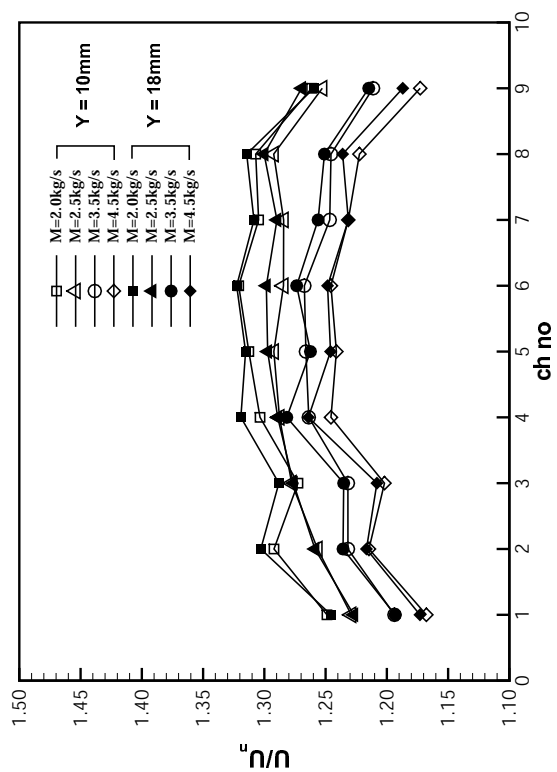
The test section is geometrically symmetric (see Section 5.1). This should lead to symmetric flow through the 17 channels in the test section with symmetric upstream flow above their inlets as discussed in Section 6.3. In order to examine the flow symmetry from one channel to another, velocity was measured at certain points from channels 1 to 17 with the handle at $M=3.5$ to 5.0 kg/s. The velocity measurement in each channel is limited only at the thickness-wise (X) center due to the difficulty in positioning the LDV measuring volume in the narrow channel ($t_w = 2.97$ mm) (see Appendix C.2). The velocity, U was non-dimensionalized by the nominal average velocity, U_{avg} , which is calculated at given flow rate as discussed in Appendix C.2.

The dimensionless velocity profiles at various measurement points at $Z=300$ mm are shown from one channel to another in Fig. 6.8. The shaded rectangular bar in the figure indicates the handle location 38.1 mm above the top ends of the plates in the top end fitting. The profiles are observed nearly symmetric centered about channel 9. The velocity in middle channel 9 is slightly lower than those of their adjacent channels and the velocity in outermost channels 1 and 17 is, on the whole, lower than that in the other channels. In addition, the overall shape of the profiles is very similar to the blunted dumbbell-shape velocity profile upstream above the inlets of all the channels in the top end fitting (see Appendix D). The flow of this profile from the top end fitting may lead directly to this similar profile from one channel to another in the fully developed region of the assembly. Therefore, the flow in the fully developed region in the assembly can be assumed symmetric from channels 1 to 17.

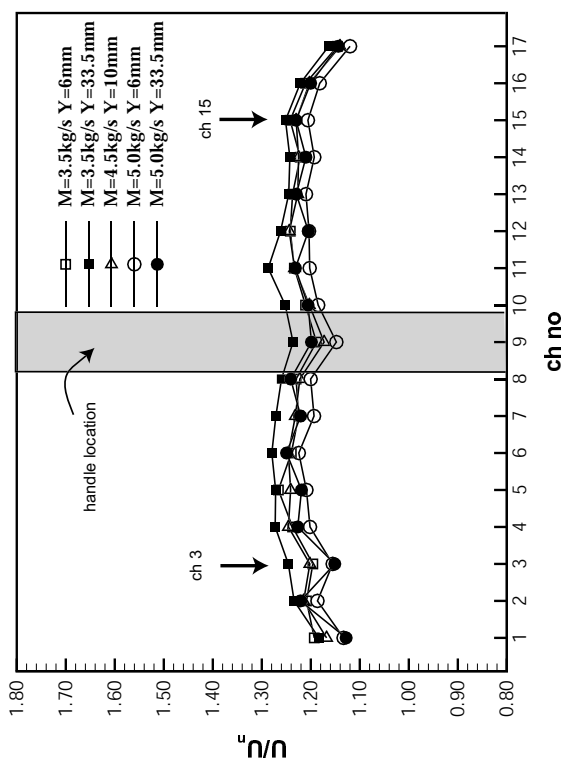
It is observed in Fig. 6.8 (a) that the velocity in channel 3 is slightly lower than that even in channel 2 except for $M=3.5$ kg/s and $Y=33.5$ mm. However, this trend is not observed at its geometrically corresponding channel 15. To investigate this trend in more detail, the dimensionless velocities from channel 1 to 9 at $Y=10$ and 18 mm at $M=2.0$ to 4.5 kg/s are plotted in Fig. 6.8 (b). This trend is not consistently observed; it is not clearly observed at $M=2.5$ and 3.5 kg/s, while it is slightly visible at $M=2.0$ and 4.5 kg/s. The vertical velocity distributions only in channel 3 showed a

slight decrease and increase in the fully developed region in Figure 6.7. Thus, it may be associated with the measurement error from locating LDV measuring volume at the thickness-wise center in channel 3 at $Z = 300$ mm. This could cause the velocity measurement point to be sensitively deviated from the thickness-wise center in the Y-direction in the channel. Hence, the measured velocity may be slightly lower than the maximum velocity at the thickness-wise center in channel 3.

In summary, the dimensionless velocity distribution from channel 1 to 17 in the test section shows symmetric centered about channel 9. It results from the geometrical symmetry of the assembly and the nearly symmetric flow upstream of the inlets of the channels. This suggests that the velocity measurement in one-half of the channels (i.e., a 1/4 cross-section) is sufficient for the hydraulic study in the whole channels.



(b) profile from channel 1 to 9



(a) profile from channel 1 to 17

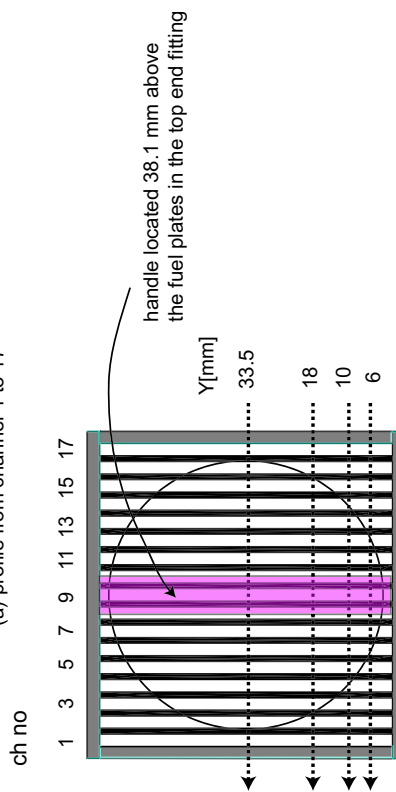


FIGURE 6.8: Symmetry of dimensionless velocity profiles through the channels in the test section

6.6 Velocity profiles in the 18-plate assembly

The previous Sections 6.3 and 6.5 show that the velocity distributions in the bottom of the calming length and from channel 1 to 17 in the test section are symmetric. Thus, the velocity only in the 1/4 cross-sectional area of the assembly was measured to study the hydraulic study in the whole channels. The axial velocities were measured at $Z=1$ and 300 mm in the width-wise (Y) direction at the thickness-wise (X) center from channel 1 to 9 using a single beam LDV at $M = 2.0$ to 5.0 kg/s (i.e., $U_n=0.59$ –1.48 m/s). Single measurement at the thickness-wise (X) center was undertaken because the channel thickness is too small for several velocity measurements (see Fig. 5.8 and Appendix C.2). The velocity profile at $Z=300$ mm was to investigate the hydraulic characteristics of the flow through the channels in the hydraulically fully developed region (Sections 6.6.1 and 6.6.2). In addition, the flow near the bottom ends of the plates was influenced due to the exit effect in Section 6.3.3. To examine this exit effect on the velocity distribution, the velocity profile at $Z=300$ mm was compared to the profile at $Z=1$ mm (Section 6.6.3).

6.6.1 Velocity profile in fully-developed region

Axial velocity was non-dimensionalized by the assembly average velocity in the manner as discussed in Appendix C.2. The dimensionless velocity profiles in the hydraulically fully developed region of the channels at $M = 2.0$ to 4.5 kg/s are shown in Fig 6.9. Note that the thickness-wise velocity gradient (X) in every individual channel was not considered since only the width-wise (Y) velocity was measured in the channels. Although the velocity measurement was undertaken in only 1/4 cross-sectional area in the test section, the profiles were projected for the other 3/4 cross-sectional area using the measured velocity data in 1/4 cross-sectional area, based on the symmetric velocity distribution from channel 1 to 17 centered about channel 9 in Section 6.5.

The dimensionless velocity profiles in the assembly are generally observed similar for all the cases. The velocities in outer channels 1 to 3 and middle channel 9 are slightly lower than the velocities in between these channels. The velocity in middle

channel 9 is consistently lower than those in its adjacent channels (i.e., channels 4 to 8). As discussed in Section 6.5, this may be mainly associated with the effect of the handle presence in the top end fitting because the lower velocity flow into the inlet of channel 9 due to the wake underneath the handle may lead to the relatively lower velocity in its fully developed region. Correspondingly, the higher velocity flow into its adjacent channels may result from the higher velocity in their inlets due to the effect of the gradual contraction and expansion by the handle. The comparatively lower velocities in the outer channels may result both from the low velocity flow into their inlet due to both the boundary layer development from the sidewalls and the exit effect of the possibly larger hydraulic resistance of the flow stream bending to the bottom end fitting pipe.

In summary, the velocity profiles in the fully developed region of the assembly shows similar shapes, on the average, for all the cases. The lower velocity in middle channel 9 is consistently observed due to the handle in the top end fitting, which may cause the slightly higher velocities in its adjacent channels. The comparatively low velocities in the outer channels result from the boundary layer from the sidewalls in the top end fitting and the exit effect. In addition, the handle effect and exit effect on the flow in the assembly are discussed in Sections 6.8 and 6.6.3, respectively.

6.6.2 Width-wise (Y) velocity profile in each channel

To examine the velocity distribution in the individual channels, the width-wise (Y) dimensionless velocity is plotted against normalized channel width in Fig. 6.10. Note that the channel width was normalized simply by $y^* = \frac{Y}{W/2}$.

The profiles show very similar curve in all the channels over the experimental range. Substantially low velocity is observed in the immediate proximity of the side-plate wall (60–80% of the average velocity at $y^*=0.03$ ($Y=1$ mm)) in every channel where three walls provide the frictional resistance. Slightly deeper into the channels at $y^*=0.09$ – 0.18 ($Y=3$ – 6 mm) where additional frictional resistance by the side plates starts to be diminished, the velocity is increased to 90–100%, and then the velocity remains fairly constant at 100–105% at $y^*=0.30$ – 1.00 ($Y=10$ – 33.5 mm) where only

the two fuel-plates' walls provide the frictional resistance, similarly to flow between parallel plates. Thus, the viscous shear-layer region solely due to the frictional resistance by the side plates is confined within $y^*=0-0.18$ ($Y=0-6$ mm) in each channel. This agrees well with the previous research of Harnett, et. al[12], as shown in Appendix E. The viscous shear layer is confined only in the immediate proximity to the side-plates wall and the wide central region in the channel shows a similar velocity profile to that of flow between parallel plates. This suggests that the flow in the channels can be approximated simply as flow between parallel plates.

6.6.3 Exit effect on velocity profile

The vertical velocity distribution in Fig. 6.7 showed that the velocity near the channel exit was influenced by the exit effect of abrupt expansion in the plate-free duct and abrupt contraction in the bottom end fitting. As stylized in Fig. 4.4, the flow from the peripheral sub-channels in the channels should bend slightly or severely to enter the circular entrance, whereas the flow from the central sub-channels should enter directly downward. The hydraulic resistance from this flow stream bending is dependent on the channel location and its properties of the sub-channels (central or peripheral) (see Appendix A.1). To study this exit effect on the flow near the channel exit, the velocity profiles near the channel exit at $Z = 1$ mm were compared to those in the fully developed region at $Z = 300$ mm in Fig. 6.11. Note that the vertical dotted line in each figure denotes the approximate circumferential line of the bottom end fitting pipe; the left-hand side is the peripheral sub-channel and the right-hand side is the central sub-channel.

It is generally noticed that the velocity profiles at $Z=1$ mm is slightly deflected compared to those at $Z=300$ mm. Overall, the velocities in the peripheral sub-channels are slightly decreased, whereas the velocities in the central sub-channels are increased in all the channels. The velocities are decreased approximately by 3–10% in the peripheral sub-channels, and are increased by 2–8% in the central sub-channels, respectively. The exit effect may be responsible for this profile deflection. For the peripheral sub-channels in the outer channels (2 and 3 in the figure), the distance from the corner of these peripheral sub-channels to the circular pipe is relatively long. The

flow streams should bend considerably and travel longer to reach the circular pipe. This can result in a relatively higher hydraulic resistance, and thus a relatively larger velocity decrease. For the peripheral sub-channels in the central channels (7 and 9 in the figure), however, that distance is relatively short and thus the flow streams need to bend slightly and have a short distance to travel to enter the circular tube. Thus, this relatively smaller hydraulic resistance leads to the smaller velocity decrease therein.

It is evident that the velocities in the central sub-channels of all the channels are slightly increased due to the continuity in the channels. The multiple streams especially from the peripheral sub-channels of the outermost channels should compete to enter the narrower circular pipe. This leads to the slight velocity decrease in even the peripheral sub-channels of the central channels.

In summary, the velocity near the channel exit is slightly influenced by the exit effect. The velocities in the central sub-channels are slightly increased, whereas the velocities in the peripheral sub-channels are slightly decreased in all the channels by different extent. This depends on the magnitude of the hydraulic resistance of the flow streams bending to enter the narrower bottom end fitting pipe, depending on the channel location and the properties of its sub-channels. However, **this exit effect on the velocity profile near the channel exit is not significant.**

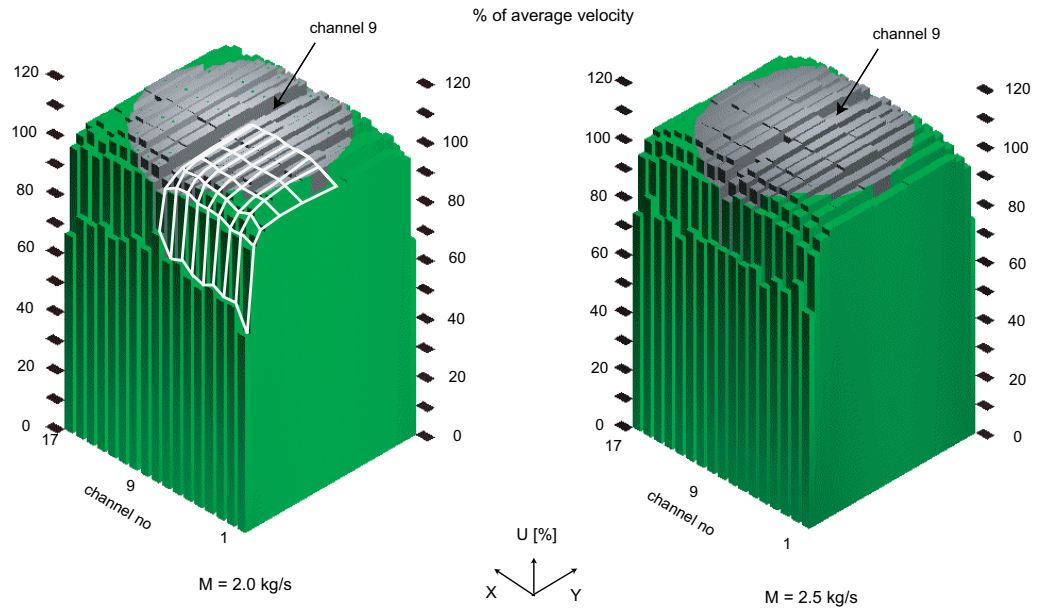
6.6.4 Summary

The velocity profiles in the assembly are examined in detail. The discussion can be summarized as follows:

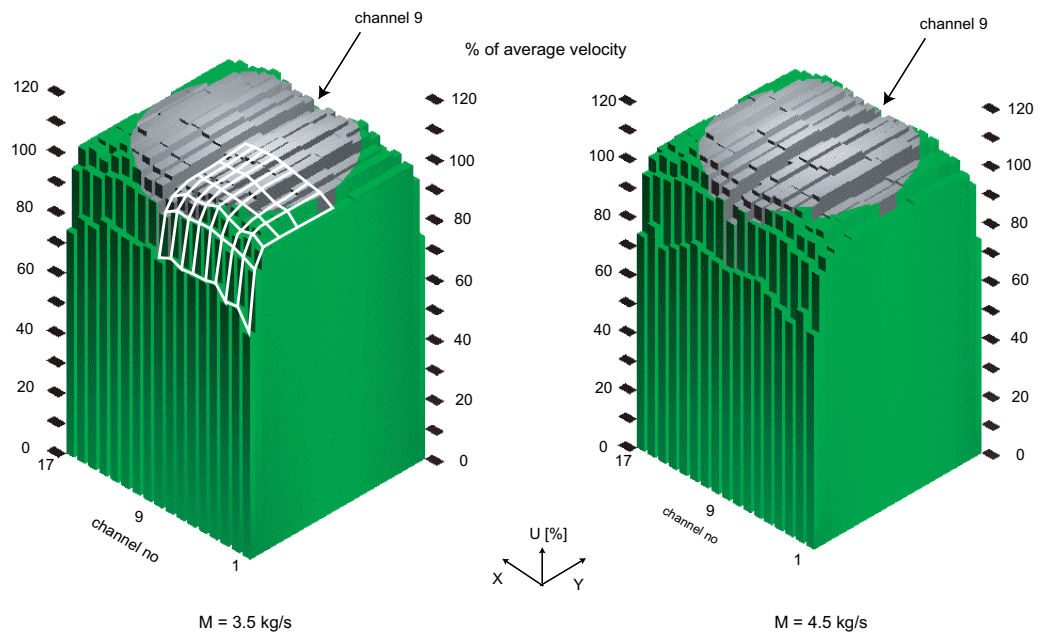
1. The velocity profiles in the hydraulically fully developed region of the assembly show, on the whole, constant.
2. The width-wise velocity profiles in the individual channels are very close to flow profile between parallel plates. The viscous shear layer is confined to the close proximity to the side-plates wall and a large central region in the channel has nearly constant velocity distribution. Therefore, the flow in the individual

channels can be approximated as parallel-plate flow except for their outermost corners.

3. The velocity profiles near the channel exit are slightly influenced due to the bottom end fitting, compared to those in the fully-developed region. Generally, the velocities in the central sub-channels are slightly increased, whereas those in the peripheral sub-channels are correspondingly decreased. However, this exit effect on the velocity profile near the channel exit is not significant.



(a) $M=2.0$ and 2.5 kg/s



(b) $M=3.5$ and 4.5 kg/s

FIGURE 6.9: Dimensionless velocity profiles with the handle on at $Z=300$ mm at $M=2.0$ – 4.5 kg/s

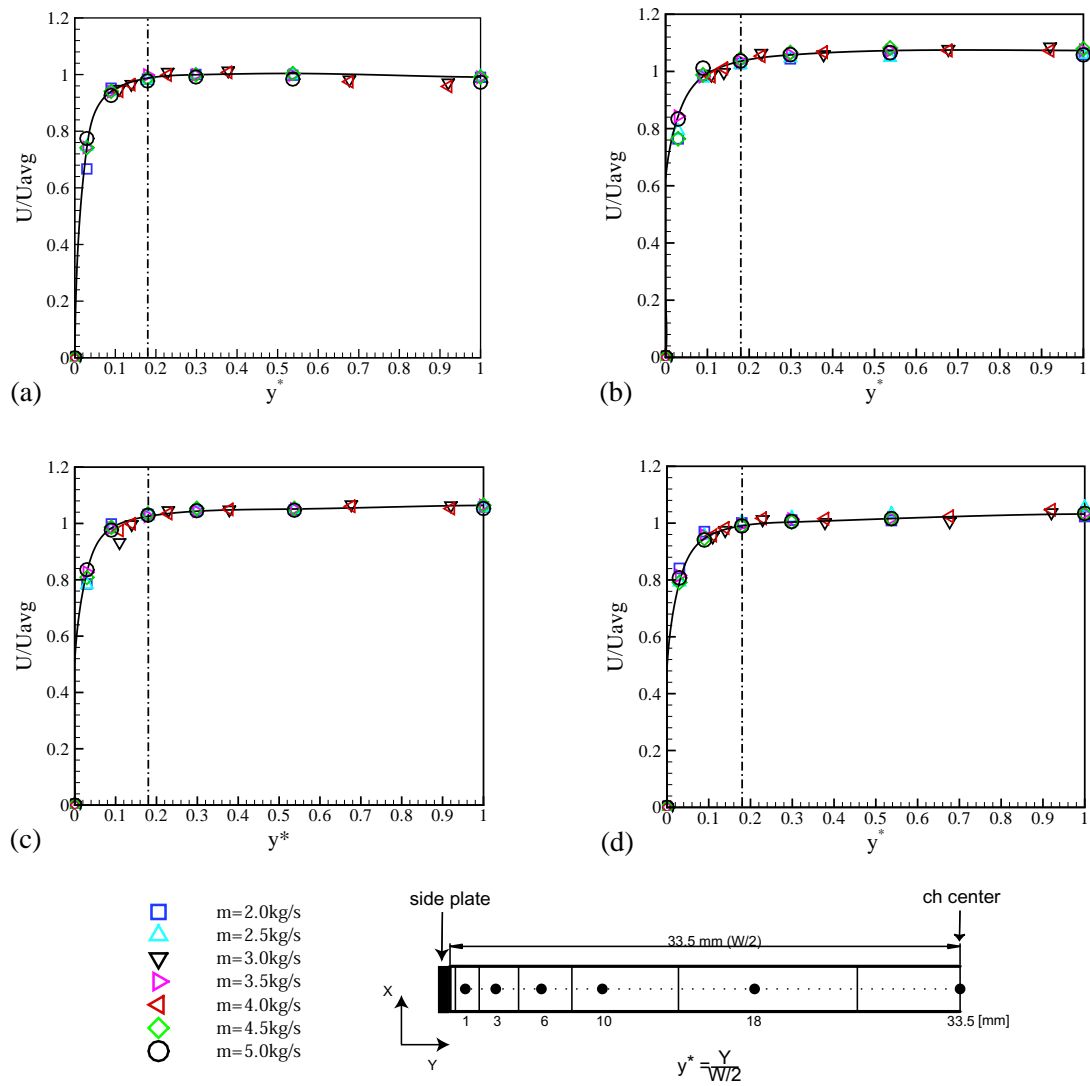


FIGURE 6.10: Widthwise velocity profile in the channels: (a) channel 1, (b) channel 4, (c) channel 7, (d) channel 9

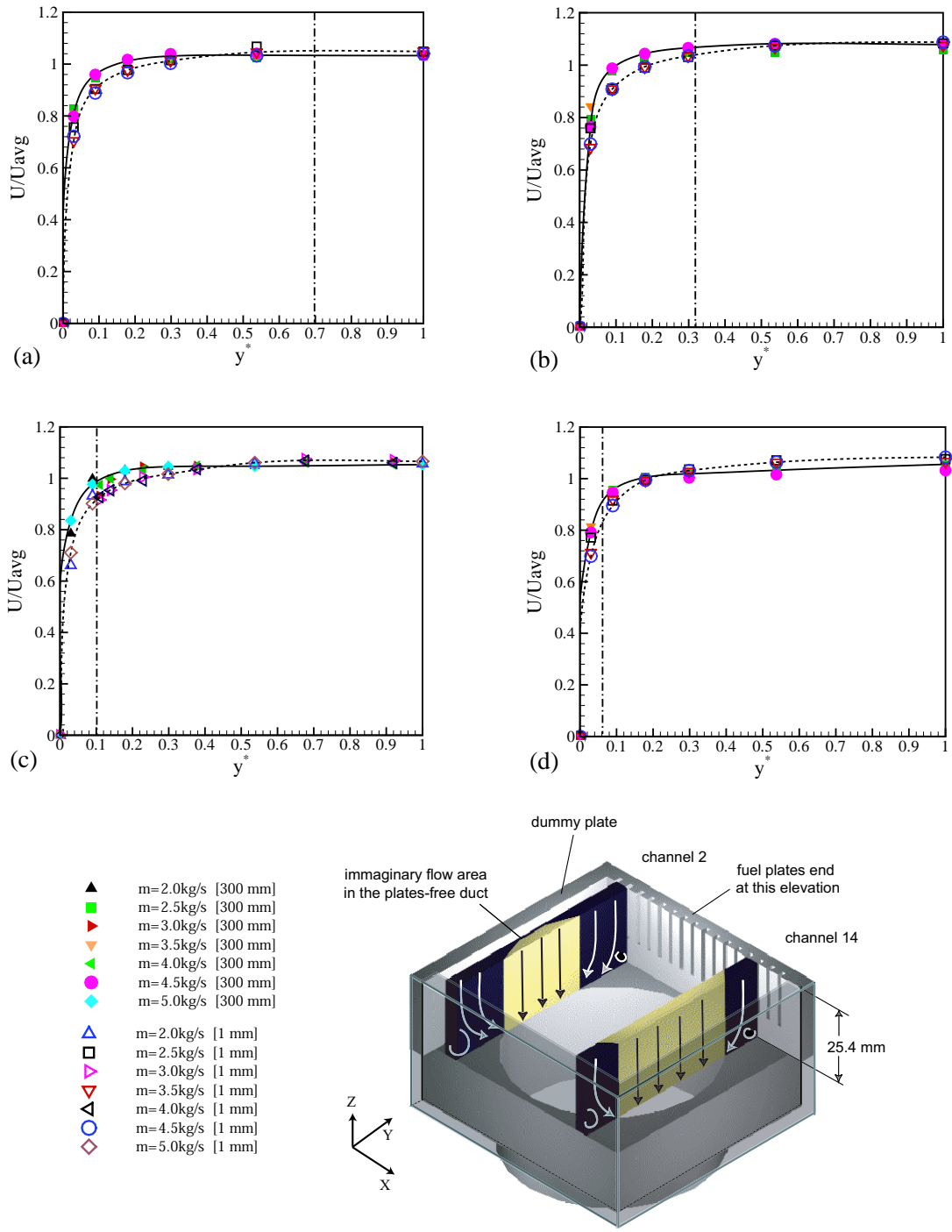


FIGURE 6.11: Exit effect on the velocity profile in the channels: (a) channel 2, (b) channel 4, (c) channel 7, (d) channel 9, dash-dotted line denotes approximate circumferential line of the circular pipe in the bottom-end fitting (peripheral sub-channels (left) and central sub-channels (right))

6.7 Flow distribution in the assembly

The previous Section 6.6 discussed the velocity distribution in the channels. Herein, the channel-to-channel flow distribution is discussed. The average velocity in each channel at given flow rate is calculated from the local velocities measured at 6 points in every channel at $Z=300$ mm with the handle. The average flow in every channel is evaluated from this average velocity, and the channel-to-channel flow distribution is obtained. The channel-to-channel flow distributions at all the experimental conditions are shown in Fig. 6.12. Note that the channel average flow is calculated by dividing the channel average velocity with the assembly average velocity at given flow rate.

The channel-to-channel flow distributions at all the experimental conditions generally show very similar curve. The average flow is distributed substantially uniformly from one channel to another: 95–100% of the assembly average flow in outer channels 1 to 3, 101–105% in central channels 4 to 8 and 98–101% in middle channel 9. There is a relatively lower average flow both in the outer channels and in the middle channel, and a slightly higher average flow in between these channels. This distribution is very similar to the channel-to-channel velocity profile (Fig. 6.8) and consistent with the velocity profiles in the fully developed region in Figure 6.9. Hence, the handle effect should account for this flow distribution. However, its extent is only small; the average flow in channel 9 is only less than 3% smaller than the assembly average. In addition, the channel average flow is only slightly increased toward middle channel 9 although the large decrease in the hydraulic resistance due to the exit effect is expected. This also suggests that the exit effect on the flow through the channels be not significant.

In summary, the average flow from one channel to another is shown fairly uniformly-distributed at $M = 2.0$ to 5.0 kg/s with the handle. Only slightly low average flow in the outer channels and middle channels, and slightly high average flow in between these channels are observed. This may result mainly from the handle effect in the top end fitting. In addition, the handle effect on the flow is discussed in more detail in the next section 6.8.

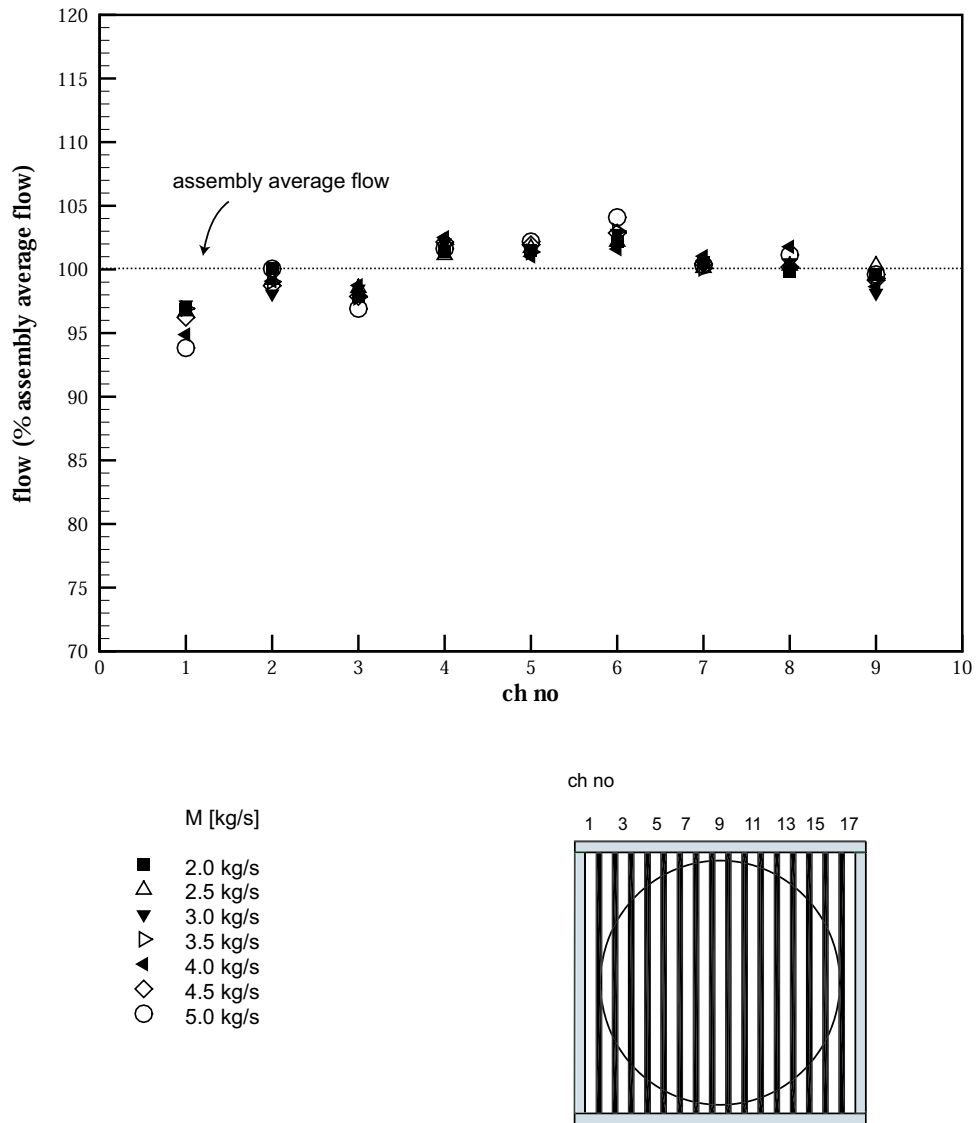


FIGURE 6.12: Channel-to-channel flow distribution in the assembly

6.8 Handle effect on the flow in the assembly

The nearly uniform and symmetric flow from the calming length should be disturbed above the channel inlet due to the wake past the handle in the top end fitting, as stylized in Fig. 4.3. To examine this handle effect on the flow in the hydraulically fully developed region, the velocity was measured at $Z=300$ mm in the test section with and without the handle at $M=2.0$ and 5.0 kg/s. The velocity profile (Section 6.8.1) and the channel-to-channel flow distribution (Section 6.8.2) are compared in both cases.

6.8.1 Handle effect on Velocity Profile

The velocity profiles generally show a slightly different shape in both cases at $M=2.0$ and 5.0 kg/s in Fig. 6.13(a) and 6.13(b). From the grid line of the profiles in the figures, the velocity, especially in channel 9, is slightly lower than that in their adjacent channels with the handle. The profile shows slight undershoot near channel 9 with the handle. This was clearly observed in Fig. 6.8, which showed the flow symmetry centered about channel 9 from channel 1 to 17 in Section 6.5. However, the profiles without the handle do not show this undershoot but a smooth increase toward middle channel 9. The difference of these profiles in both cases should be related to the handle in the top end fitting.

With the handle, the flow distribution in the channel inlet may be similar to a blunted dumbbell-shape due to the wake past the handle (Appendix D). This may lead to a slight undershoot profile near channel 9. Without the handle, however, the flow developing from the calming length can be further developed toward the fully developed profile down to the channel inlet. This should lead to the smooth profile near middle channel 9 in the fully developed region. In addition, the velocity profiles in outer channels 1 to 3 have a similar shape in both cases. They are not influenced by the handle because they are located relatively far away from the handle.

In summary, the velocity profiles with and without the handle show a slightly different profile, especially near middle channel 9. The profiles with the handle show

a slight undershoot near middle channel 9, while those without the handle do not show this undershoot. The velocities in the outer channels are not influenced by the handle presence in the top end fitting.

6.8.2 Handle effect on flow distribution

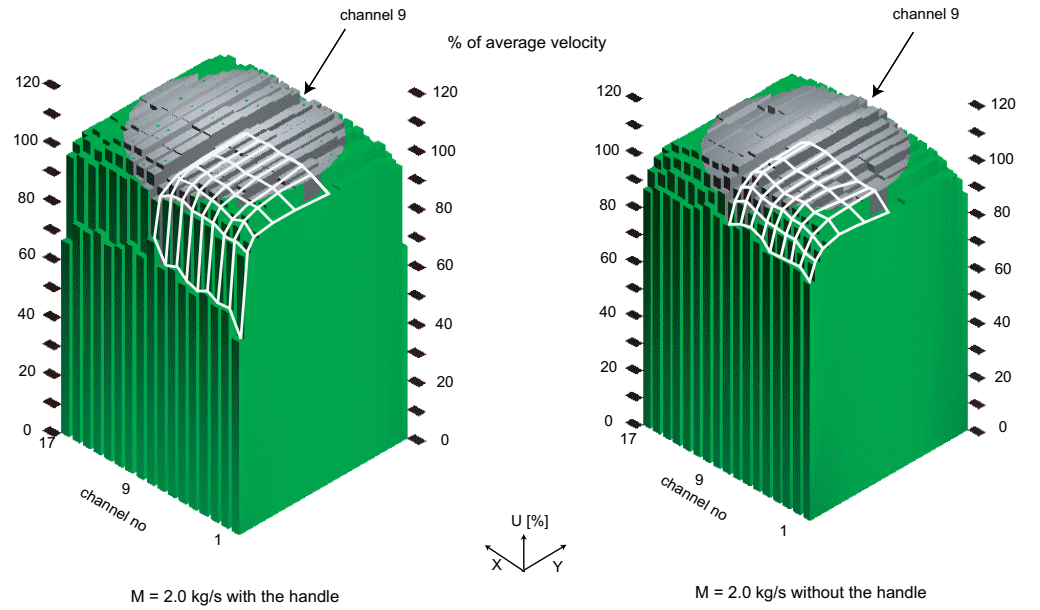
The channel-to-channel flow distributions with and without the handle at $M = 2.0$ and 5.0 kg/s are compared in Fig. 6.14. It is clearly shown that the influence of the handle on the flow distribution is evident near middle channel 9. The channel average flow with the handle is slightly decreased toward middle channel 9, whereas it is slightly increased without the handle. Correspondingly, the average flow in its adjacent channels 4 to 6 is also slightly different; the with-handle case shows slightly higher channel average flow than the without-handle case. The handle should be responsible for this difference, as discussed for the velocity profile in the previous section. However, this difference is generally less than 5%. In addition, it is observed that the flow distribution in outer channels 1 to 3 shows a similar profile in both cases, in the same manner as for the velocity profile.

In summary, the handle in the top end fitting shows a slight influence on the channel-to-channel flow distribution, in the same manner as for the velocity profile. There is slightly less average flow in the middle channels, and correspondingly slightly more average flow in their adjacent channels with the handle. However, this trend is not observed without the handle. The handle effect on the channel-to-channel flow distribution is not significant; less than 5% of the assembly average flow.

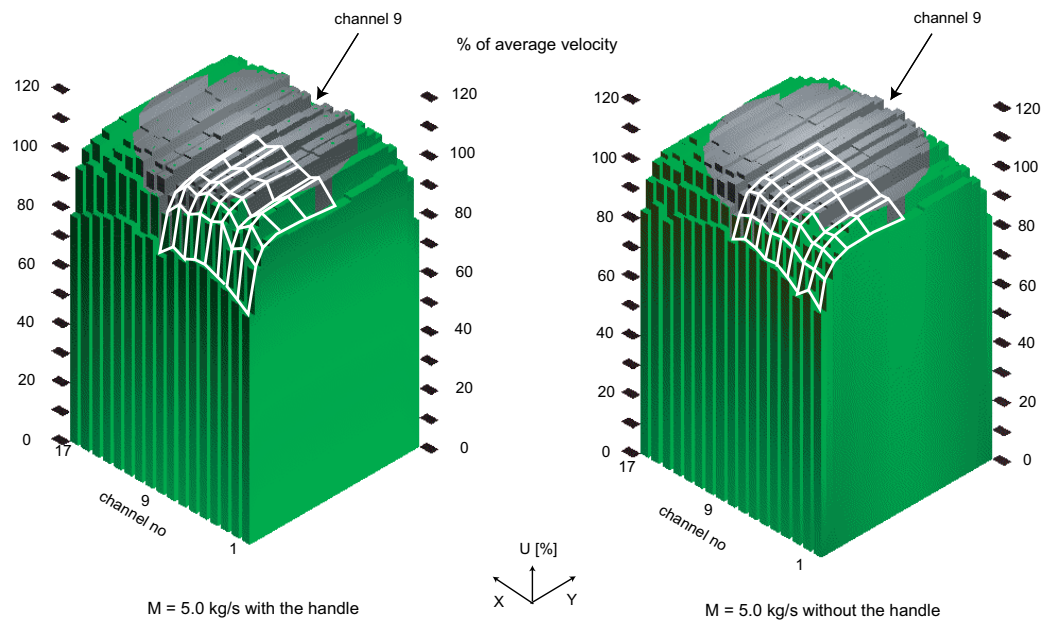
6.8.3 Summary

The influence of the handle in the top end fitting on the velocity profile and the channel-to-channel flow distribution is evident from the comparison of the experiments both with and without the handle. The velocity distribution and the channel-to-channel flow distribution with the handle are slightly decreased near middle channel 9. Correspondingly, they are slightly increased in its adjacent channels. This is very

close to the dumbbell-shape flow distribution in the channel inlet past the handle. However, this trend is not observed without the handle because the nearly symmetric and uniform flow from the calming length can be further developed down to the channel inlet. This results in the smooth profiles of the velocity and the average flow from one channel to another. In addition, both profiles at outer channels (1 to 3) are not influenced by the handle. The handle effect is limited only near middle channel 9 and its extent is also only small. Thus, **the handle effect on the velocity profile and the channel-to-channel flow distribution in the assembly is not significant.**



(a) $M=2.0$ kg/s



(b) $M=5.0$ kg/s

FIGURE 6.13: Handle effect on dimensionless velocity profiles at $Z=300$ mm at $M=2.0$ and 5.0 kg/s

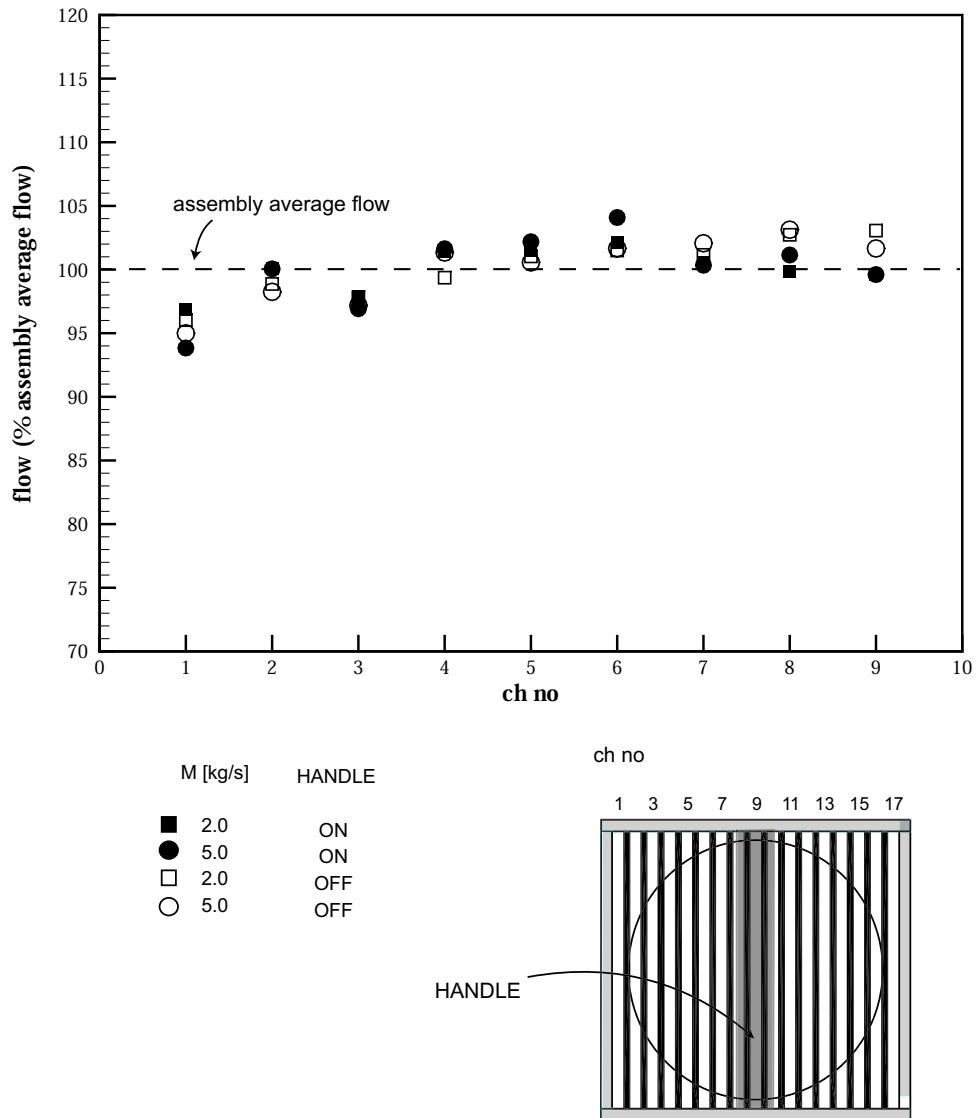


FIGURE 6.14: Handle effect on the channel-to-channel flow distribution at $M=2.0$ and 5.0 kg/s

6.9 Comparison of flow distribution with previous studies

Among the several previous studies on the thermal-hydraulics in the MNR fuel assembly, the present experimental result is compared to those of Rummens' experiment (Section 6.9.1) and Blahnik's engineering calculation (Section 6.9.2), and Yu's numerical simulation (Section 6.9.3), especially on the channel-to-channel flow distribution in the 18-plate assembly. Note that Rummens' experiment and Blahnik's engineering calculation were conducted in the standard 18-plate assembly but Yu's numerical simulation was conducted in the simulated 18-plate assembly in the same geometry as the present experiment. In addition, the flow distribution from channel 10 to 17 in the present experiment is produced, based on the symmetric flow distribution from channel 1 to 17 centered about channel 9 (see Fig. 6.8).

6.9.1 Comparison of flow distribution with Rummens' experiment

Rummens et. al [4] investigated the thermal-hydraulics in the standard 10-plate and the 18-plate fuel assembly by measuring the pressure drop in the channels in the laminar regime. The relative average velocity in the channels was deduced from this measured pressure drop, and the channel-to-channel flow distribution was obtained. The flow distribution only in the 18-plate assembly is compared to the result of the present experimental here.

The flow distributions of Rummens' experiment and the present experiment for laminar regime are compared in Fig. 6.15. Note that $Q=0.5$ and 1.2 L/s in Rummens' experiment are equivalent to $M=0.5$ and 1.2 kg/s by assuming the experimental temperature of $T = 15$ °C. Both results show significantly different distributions. Consistently, the average flow is lower in outer channels (1 to 3) and higher in central channels (6 to 12) than that in the present experiment at $M=1.2$ kg/s. The difference ranges from 10 to 17%. This large difference may be due to two reasons:

- the geometrical difference between the standard 18-plate assembly and the simulated one,

- the different simulation of the inlet flow to the top end fitting of the both assemblies (entrance effect).

The standard assembly is geometrically different from the simulated assembly (Section 5.1). The properties of the sub-channels (area of the peripheral sub-channels and central sub-channels) and the area in the flow channels blocked by the handle are different in both cases (see legend in the figure). The difference in the sub-channel properties can lead to the different magnitude of the exit effect in the plate-free duct, depending on the channel location. The handle can also slightly influence the flow distribution in the central channels. However, the present experiment shows that both of the handle effect and the exit effect on the channel-to-channel flow distribution are not significant (Sections 6.8 and 6.9.2) for turbulent flow. This suggests that the large difference of the channel-to-channel flow distributions should result mainly from the different entrance effect in both cases.

The present experiment used the calming length duct to simulate the uniform velocity flow into the top end fitting for the central assemblies in the MNR core (Sections 4.2 and 5.2). The velocity distribution in the bottom of the calming length was found nearly symmetric and uniform (Section 6.3). However, Rummens et al used the different simulation of the inflow to the top end fitting of the standard assembly (see Fig. 4 in Reference [5]). The standard assembly was positioned in a large Al container and its top end fitting was completely open to a large pool. Therefore, the velocity distribution of the inflow to the top end fitting may be significantly different from that in the present experiment. The flow separation (entrance effect) from the inner surface of the top end fitting walls close behind the inlet by inertial force may occur when it enters from the large outer container into the smaller top end fitting [15]. The flow separation may lead to a large decrease in the jet cross-section of uniform velocity core (i.e., jet contracta). For instance, the area ratio of the jet contracta to the entire duct can be with as much as 0.5 for turbulent flow [11]. This implies that the flow separation may cover the wide near-wall region of the top end fitting, while the undisturbed core flow may be limited to its small core-region. In addition, the length (L) of the top end fitting may not be long enough for this separated flow to be reattached and for the induced eddy to disappear before the channel inlet: $L=2.0$ in.

(50.8 mm), $L/D_{h,TP} \approx 0.74$. This entrance effect due to the two side plates is not important since it equally covers from channel 1 to 17. However, the two dummy plates of the top end fitting in the standard assembly were curved in exactly the same manner as the fuel plates. This may cause the slight different entrance effect (due to the two curved dummy plates) from one channel to another: especially in the outermost channels 1 and 17. Therefore, the entrance effect, especially due to the two dummy plates, may disturb the flow in the outer channel inlet, and may lead to the substantially lower velocity flow. However, the central channels' inlet may be exposed to high core velocity flow. This may cause the relatively high average flow in the central channels and the relatively low average flow in the outer channels in both sides.

The flow distribution in Rummens' experiment was not symmetric, whereas the present experiment showed symmetric flow (see Fig. 6.8). The relative average flow in outer channels 1 to 3 was slightly higher than that in corresponding channels 15 to 17 by 3–12%. This difference may also be related to the magnitude of the entrance effect on the surfaces of the two dummy plates in the top end fitting. Slightly different flow development into the top end fitting may be expected due to the curvature of the dummy plates. The entrance effect due to the flow separation in the top end fitting may be bigger on the surface of the dummy plate curving toward the handle (above channels 1 to 3) than on that curving away from the handle (above channels 15 to 17). Therefore, the velocities in the inlets of channels 1 to 3 may be smaller than those in the inlets of channels 15 to 17. This may lead to slightly lower average flow in outer channels 1 to 3 than that in outer channels 15 to 17. In addition, the exit effect may slightly enhance this trend although it does not show the significant effect on the flow distribution from the present experiment.

The flow distribution in the central channels 6 to 12 is also different in both cases by 7–14%. The average flow in the present experiment with the handle is as much as 5.5% lower than the assembly average, while the average flow in Rummens' experiment is about 7–8% higher. This suggests that the handle effect in Rummens' experiment was not considered.

In summary, the channel-to-channel flow distribution of the present experiment is

substantially different from that of Rummens' experiment mainly due to the entrance effect. The different simulation of the inlet flow to the top end fitting in both cases leads to this significantly different flow distribution. This entrance effect mainly due to the two dummy plates caused substantially low average flow in the outer channels and high in the central channels in Rummens' experiment. In the present experiment, however, the nearly uniform and symmetric flow in the channel inlet from one channel to another leads to nearly uniform channel-to-channel flow distribution.

6.9.2 Comparison of flow distribution with Blahnik's engineering calculation

Blahnik [5] computed the conservative flow profile from published hydraulic resistance data by assuming discrete sub-channels within the physical coolant channels that extend into the transition volume below the fuel plates in laminar and turbulent regimes. To estimate the pressure drop in all the individual channels at given flow rate, the entry loss from the top end fitting to the channel inlet, the frictional loss in the plate region, and the exit loss in the plate-free duct were separately considered, depending on the channels' location and their sub-channels' properties (area and perimeter of the peripheral sub-channels and central sub-channels). The channel-to-channel flow distribution was calculated from this computed pressure drop in every channel. Blahnik deduced the average flow profile from this computed channel-to-channel flow distribution for the turbulent regime. Note that the handle effect in the top end fitting was not considered in Blahnik's engineering calculation.

Fig. 6.15 and 6.16 compare the computed channel-to-channel flow distributions with that of the present experiment in laminar and turbulent regimes, respectively. For the laminar regime in Fig. 6.15, the flow distribution of Blahnik's calculation agreed qualitatively well with that of Rummens' experimental. However, it is different from the flow distribution of the present experiment but this difference is within about 5% except for outermost channels 1 and 17 and central channels 9 to 11. On the other hand, for the turbulent regime in Fig. 6.16, both results also agree qualitatively well except for outermost channels 1 and 17 (see average flow profile). However, the channel-to-channel flow distributions at $M=3.5$ and 5.0 kg/s are slightly different

from the present experiment. The average flow in channels 3 to 8 is very close in both cases (within 4%), but a slightly larger difference (5–10%) is detected in channels 9 to 15 and about 20% in outermost channels 1 and 17. This difference in both cases may be mainly related to the estimation of the exit loss in the plate-free duct.

For the estimation of the pressure drop in the channels, the entry loss and the frictional loss were not significantly different from one channel to another (see Appendix A in the reference [5]). However, the exit loss due to the hydraulic resistance of the flow stream bending to enter the bottom end fitting and the flow stream merging from the multi-channel in the plate-free duct is different depending on the channel location since the sub-channel properties are significantly different (Appendix A.1). This exit loss was estimated from the published data, depending on the channel location and the sub-channel properties; note that the minor loss coefficient of the flow stream bending and merging in the peripheral sub-channels is much larger than that in the central sub-channels. This leads to substantially lower average flow in the outermost channels than the present experiment since these channels completely consist of the peripheral sub-channel. However, the area ratio of the peripheral sub-channels in the channel decreases toward middle channel 9, and the contribution of the exit loss to the overall loss should also decrease. This results in the relatively uniform flow distribution in the central channels. In addition, the present experiment in the simulated assembly with flat plates showed that the exit effect (loss) is not an important factor on the flow distribution (Section 6.6.3). Therefore, Blahnik's calculation may overestimate the exit loss in the plate-free duct. This leads to the large different average flow in the outermost channels.

The channel-to-channel flow distribution in Blahnik's engineering calculation was not symmetric. The average flow in the first half of channel 1 to 8 is slightly lower than that in the other half of channel 9 to 17. This is related to the non-symmetric standard assembly (see Fig. A.1 and A.2). The area of the peripheral sub-channels in the first half is slightly larger than that in their corresponding channels in the other half. On the other hand, the channel-to-channel flow distribution for the turbulent regime both in the present experiment and Blahnik's calculation generally shows a comparatively more uniform profile through the channels than that for the laminar regime.

In summary, the channel-to-channel flow distribution of Blahnik's calculation agrees qualitatively well with that of the present experiment except for the outermost channels where the substantially low average flow is observed due to the overestimation of the exit loss in the plate-free duct. Blahnik's non-symmetric flow distribution centered about channel 9 may result from the non-symmetric properties of the sub-channels in the standard assembly.

6.9.3 Comparison of flow distribution with Yu's numerical simulation

Yu [6] conducted a numerical simulation on the thermal-hydraulics in the same geometry of the 18-plate assembly as the present experiment without considering the handle in the top end fitting. This channel-to-channel flow distribution is compared to the result of the present experiment in Fig. 6.17.

Generally, both results show excellent agreement with the present experiment. The average flow is fairly uniformly-distributed from channel 1 to 8; 97–103% of the assembly average flow in Yu's simulation and 95–103% in the present experiment. This good agreement may be related to the similar inlet flow distribution (entrance effect) of the channels in the top end fitting. The present experiment showed a nearly uniform and symmetric velocity distribution in the bottom of the calming length (or at the top of the top end fitting, see Section 6.3), and Yu's simulation assumed the uniform flow at the inlet of the top end fitting. Thus, the flow distribution above the inlet of channels 1 to 17 in Yu's simulation should be very similar to that of the present experiment without the handle. This suggests that the inlet flow distribution from one channel to another in the top end fitting (entrance effect) is a very influential factor on the channel-to-channel flow distribution.

The handle was not considered in Yu's simulation. Thus, the figure shows that Yu's result agrees with the present experiment more accurately without the handle than with the handle. However, the difference between Yu's simulation and the present experiment with the handle is very small (i.e., within 2%). This is consistent because the present experiment showed that the handle effect was not significant on the channel-to-channel flow distribution (Section 6.9.2).

In summary, the channel-to-channel flow distribution of Yu's numerical simulation agrees excellently with the present experiment. This good agreement may result from very similar inlet flow distribution of channel 1 to 17 in both cases.

6.9.4 Summary

The channel-to-channel flow distribution of the present experiment was compared to the previous studies of Rummens' experiment and Blahnik's engineering calculation in the standard assembly, and Yu's numerical simulation in the simulated assembly.

1. Rummens' experiment shows significantly different channel-to-channel flow distribution mainly due to the different simulation of the inlet flow to the top end fitting in both cases (entrance effect).
2. Blahnik's calculation generally agrees well with the present experiment except for the outermost channels in which the slight overestimation of the exit effect is responsible for this large difference.
3. Yu's simulation shows excellent agreement with the present experiment since both have very similar flow distribution in the inlet of the channels in the top end fitting (entrance effect).

Therefore, the entrance effect is one of the most influential factors on the channel-to-channel flow distribution in the assembly from these comparisons. This suggests that the channel-to-channel flow distribution may be significantly different, depending on the location of the assemblies in the MNR core (i.e., outermost assemblies or central assemblies). In addition, the previous studies did not include the handle effect on the flow distribution but the present experiment showed that it was not an influential factor. The handle effect in the standard 18-plate assembly should be slightly smaller than in the simulated assembly of the present experiment because the flow area obstructed by the handle in the standard assembly is more distributed in the middle channels (8 to 10) than in the simulated assembly (see legends in Fig. 6.15 and 6.16). This suggests that the handle effect should not be an influential factor on the flow distribution in the standard assembly.

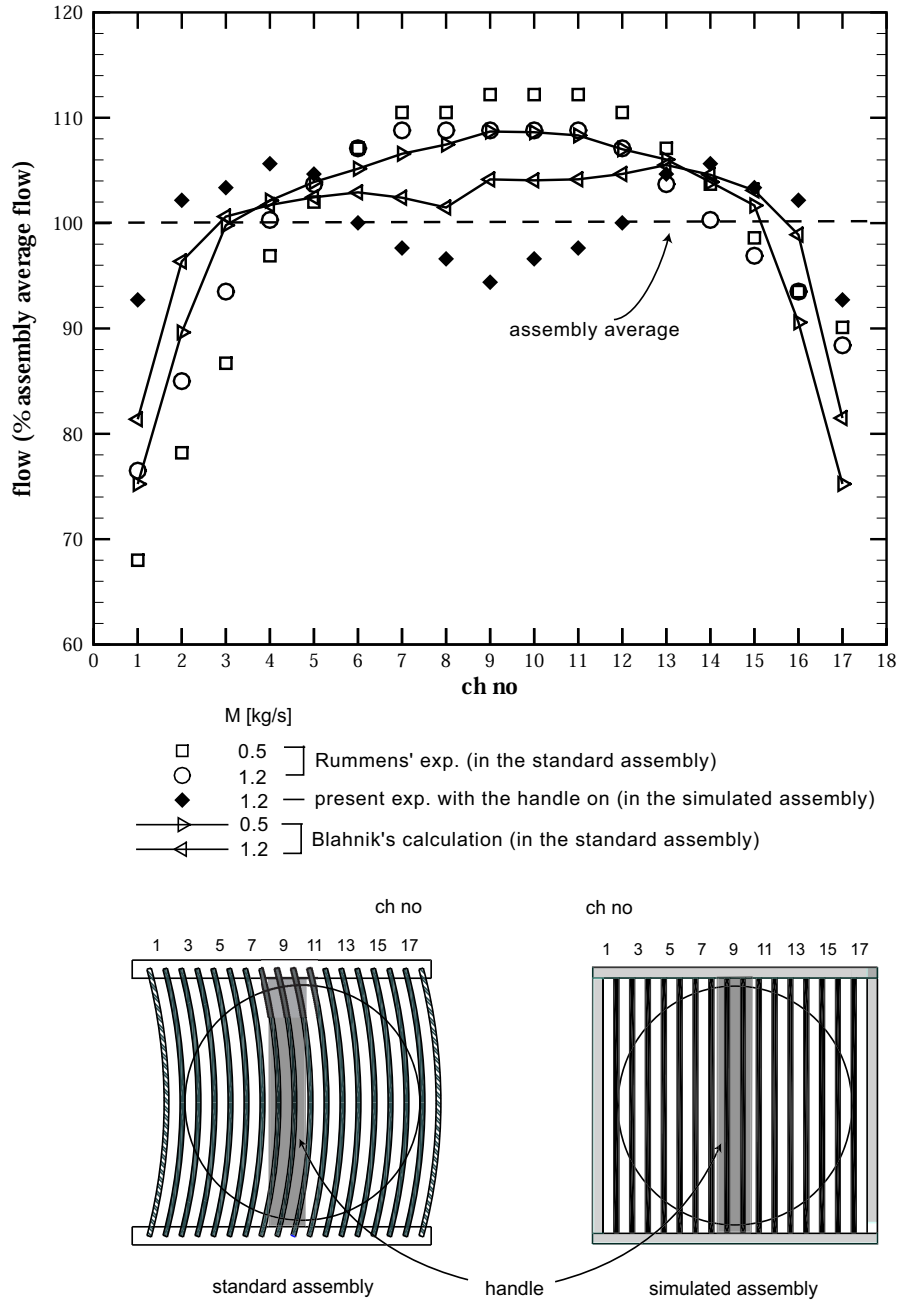


FIGURE 6.15: Comparison of the channel-to-channel flow distribution of the present experiment in the simulated assembly at $M=1.2$ kg/s, Rummens' experiment and Blahnik's engineering calculation in the standard one at $M=0.5$ and 1.2 kg/s

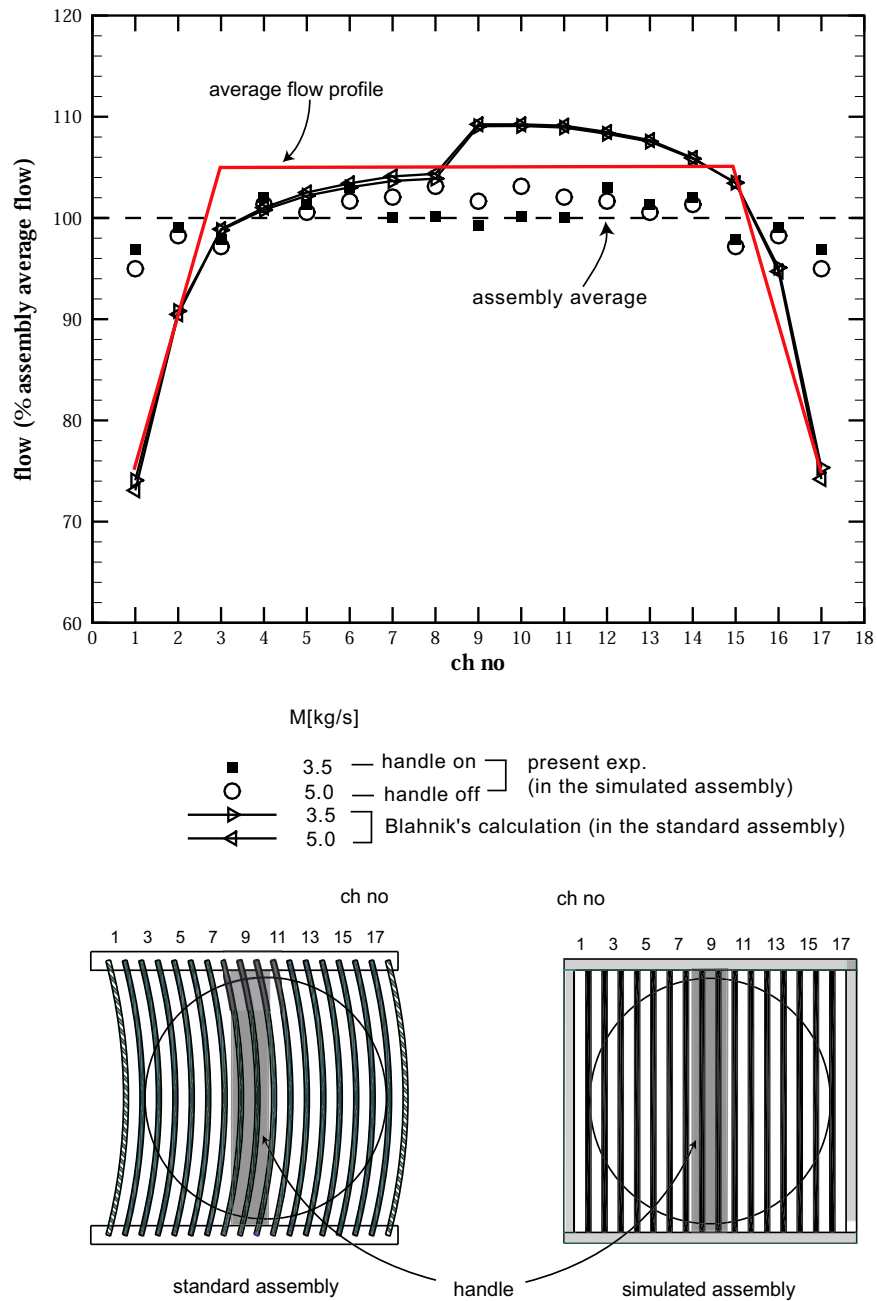


FIGURE 6.16: Comparison of the channel-to-channel flow distributions of the present experiment and Blahnik's engineering calculation at $M=3.5$ and 5.0 kg/s

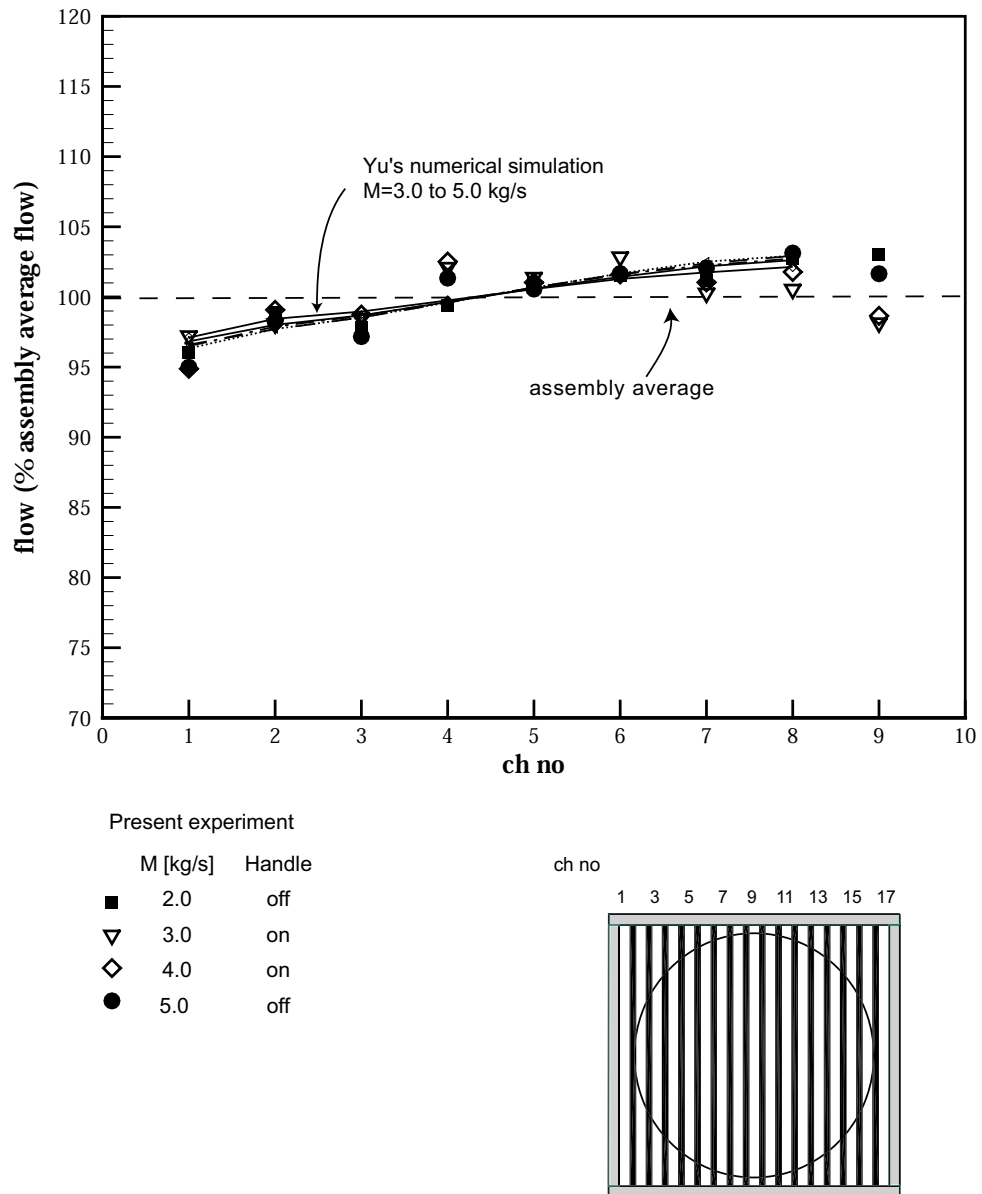


FIGURE 6.17: Comparison of the channel-to-channel flow distribution of the present experiment and Yu's numerical simulation. Note that Yu's simulation was conducted in the simulated assembly with same inner dimension as the present experiment

6.10 Evaluation of flow rate through 18-plate assembly during experiment

To confirm the flow rate through the test section from measured quantities, the flow rate was evaluated from the measured width-wise (Y) velocity distribution at the thickness-wise (X) center in the channels. This flow rate was evaluated only from the width-wise velocity distribution with the assumption of the uniform thickness-wise velocity distribution in the channels should be slightly overestimated. To correct this overestimation of the flow rate, the thickness-wise velocity gradient in each channel was considered, using the logarithm law for turbulent flow by Eq. (4.8). The detailed calculation of these flow rates is attached in Appendix F. These flow rates were compared to the nominal flow rates in Fig. 6.18. Note that the nominal flow rate was measured within a 1.5% error (Appendix H).

Fig. 6.18 shows that the flow rates evaluated from only the width-wise velocity distribution in the channels are overestimated approximately by 15–25% of the nominal flow rates. This is reasonable because the average velocity calculated from only the width-wise velocity distribution in each channel must be slightly higher than the actual average velocity, which includes both the thickness-wise (X) and width-wise (Y) velocity gradient over the entire cross section of the channel. This large error is reduced with increasing flow rate (i.e., increasing velocity or Re) from 25% at $M=2.0$ kg/s ($Re=4281$) to 15% at $M=5.0$ kg/s ($Re=10545$). This is also anticipated because the flow may be slightly in the transition region at the low flow rate of $M=2.0$ kg/s and becomes more turbulent with increasing flow rate. Thus, the assumption of the uniform thickness-wise velocity distribution for the estimation of the channel average velocity in the channels becomes more realized with increasing flow rate.

To correct this large overestimation, the thickness-wise velocity gradient was considered using the logarithm law by Eq. 4.8. After this correction is applied, a closer agreement between the nominal flow rate and the corrected one is observed; the difference is significantly reduced from 15–25% to -2–6%. This difference decreases with increasing flow rate. This is reasonable since the logarithm law is valid for turbulent

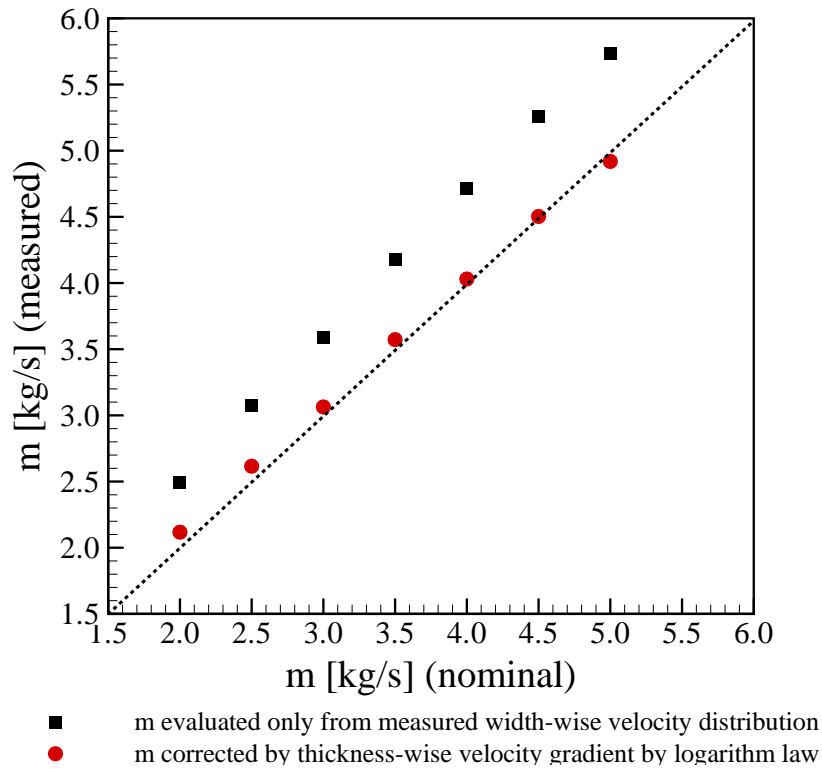


FIGURE 6.18: Comparison of the nominal flow rates and the flow rates evaluated from the measured width-wise velocity distribution in each channel at $M=2.0$ to 5.0 kg/s

flow and the flow becomes more turbulent with increasing flow rate. Considering the experimental error of positioning the measuring volume exactly at the thickness-wise (X) center in the Y-direction in the channel (see Section 8.1), the agreement is excellent. This suggests that the width-wise velocity measurement was undertaken accurately at the thickness-wise center in the channels.

In summary, the flow rate evaluated with only the measured width-wise velocity in the test section is slightly overestimated but the corrected flow rates by considering the thickness-wise velocity gradient in the channels are predicted within only 6% of the nominal flow rate. Therefore, this good agreement with the nominal flow rate can confirm that the flow was circulated through the test section at the nominal flow rate during experiment.

6.11 Summary

To investigate the hydraulic characteristics of coolant flow in one of the standard 18-plate assemblies in the central region of the MNR core, velocity was measured at two elevations in the simulated 18-plate assembly by using LDV. The velocity profiles in each channel and in the assembly and the channel-to-channel flow distribution were investigated.

1. The calming length duct on the top of the simulated 18-plate assembly successfully simulated the inlet flow condition to the central assemblies in the MNR core from the pool to the reactor core. The fully developed profile in the bottom of the calming length duct wasn't completely attained due to the relatively short length of the calming length. However, the profile was nearly symmetric and uniform enough in the duct-core to simulate the uniform velocity flow into the top end fitting of the central assemblies in the MNR core.
2. Good agreement for the entrance length of the individual channels in the assembly between the experimental and prediction by a simple 1-D correlation was observed for the turbulent regime. The fully developed channel flow in the assembly channels was attained around $z^*=21D_h$ over the experimental range of $M=2.0-5.0$ kg/s ($Re=4281-10545$), which also agrees closely with the result of Yu's numerical simulation.
3. The symmetric velocity profile from channels 1 to 17 centered about channel 9 was observed due to the symmetric geometry of the simulated assembly as expected. The velocity profile in the fully developed region ($Z=300$ mm) showed a relatively constant profile at $M=2.0-5.0$ kg/s. The velocity was relatively low in outer channels 1 to 3, high in central channels 4 to 8, and low in middle channel 9 due to the handle effect. It was observed that the flow in individual channels can be approximated as flow between parallel plates. The viscous shear layer due to additional frictional resistance by the side plates was confined only in the immediate proximity of the side-plate walls. The exit effect was not significant on the velocity profile from the comparison of the velocity profiles at $Z=1$ and 300 mm. The velocity in the peripheral sub-channels in the outer

channel was slightly decelerated whereas that in the central sub-channels in the central channels is slightly accelerated, due to the magnitude of the exit effect of the flow bending, depending on the channel location.

4. The channel-to-channel flow distribution in nine channels in the present experiment showed virtually constant and uniform profile at $M=2.0-5.0$ kg/s; a relatively low channel average flow about 95–100% in outer channels 1 to 3, high about 103–105% in central channels 4 to 7, and low around 100% in middle channels 8 and 9. This result agreed very closely with the profile of Yu's numerical simulation in the simulated assembly. Among the previous hydraulic studies in the standard assembly, Blahnik's engineering calculation generally agreed well with the present experiment except for outermost channels 1 and 17 where the exit effect was overestimated. However, Rummens' experiment showed a significantly different profile: comparatively low in the outermost channels and high in the central channels, in addition to a non-symmetric profile. This is because it was conducted in the standard assembly probably without the handle and especially in the different inlet flow condition to the top end fitting (entrance effect).
5. The handle effect on the velocity profile and the channel-to-channel flow distribution was observed to be slight. Both distributions was similar to the velocity profiles (slight dumbbell-shape profile) above the channel inlet past the handle; especially slightly low velocity and average flow in middle channels 8 to 9, high in between these channels. Without the handle, however, these distorted profiles were not observed.

The present chapter 6 discussed in detail the velocity profile in each channel and the channel-to-channel flow distribution in the assembly. The next chapter 7 will discuss the pressure drops in the assembly.

Chapter 7

Pressure drop in 18-plate assembly

Pressure drop was measured using differential pressure transmitters in the test section to evaluate the pressure drops in the plate region and the bottom end fitting (Fig. 5.9). The pressure drop through the plate region (DPFUL), the pressure drop through the bottom end fitting (DPOUT), and the overall pressure drop through the whole assembly (DPTS=DPFUL+DPOUT) are shown in Fig. 7.1 to 7.3. Note that the measurement of these pressure drops was independently undertaken. Each pressure transmitters were calibrated (see Appendix B.2 for their calibration data) and all the pressure drops in the assembly were measured within a 2% error (Section 8.2). The measured pressure drops are compared to the prediction by a simple 1-dimensional correlation. The detailed calculation of these pressure drops is attached in Appendix G.

7.1 Pressure drop through the channels

The pressure drop through the plate region in the test section (DPFUL, region 0→2 in Fig. 4.6) is measured. Its result is compared to the result of Yu's numerical simulation [6] and the prediction by the 1-D correlation of Eqs. (4.9) and (4.10) in Fig. 7.1. Note that there is no significant difference in the pressure drops of the experiment with and without the handle. The pressure drop without the handle is slightly higher than that with the handle (<3%).

Generally, it is observed that the measured pressure drop agrees well with the result of Yu's numerical simulation. Its error decreases with increasing flow rate (or Re); the pressure drop of Yu's simulation is about 16% higher at M=3.0 kg/s and 8% at M=3.5 kg/s than that of the present experiment but its difference is further

reduced reduced (<4%) at the higher flow rate. This is reasonable since complete turbulent flow through the plate region was assumed in Yu's simulation but the flow at relatively lower flow rate may not be completely turbulent (see Table 5.2).

The 1-D correlation of Eqs. (4.9) and (4.10) predicted the DPFUL accurately (<6%). This error increases with increasing flow rate probably because the pressure tap in the corner of the plate-free duct was exposed to the separated flow (eddy formation) at the contraction step due to the bottom-end fitting (see Fig. 9.4 and 9.5). This was confirmed from the vertical pressure distribution of along the assembly Yu's simulation (see Appendix G. 5). Thus, the measured pressure drop should partially include the minor pressure loss due to the abrupt contraction in the bottom end fitting but the correlation of Eqs. (4.9) and (4.10) does not include this loss. In addition, the flow separation at the contraction step in the plate-free duct may be enhanced with increasing flow rate because the flow at the lower flow rate is possibly in the transition region: $Re=3164-10545$ at $M=1.5-5.0$ kg/s. This may lead to the increasing error with increasing flow rate.

In summary, good agreement of the pressure drop through the plate region between the experimental data and the result of Yu's numerical simulation is observed. The 1-D correlation of Eqs. (4.9) and (4.10) also predicts the pressure drop through the plate region accurately. The error between the experiment and the 1-D correlation may be related mainly to the flow separation at the contraction step in the plate-free duct.

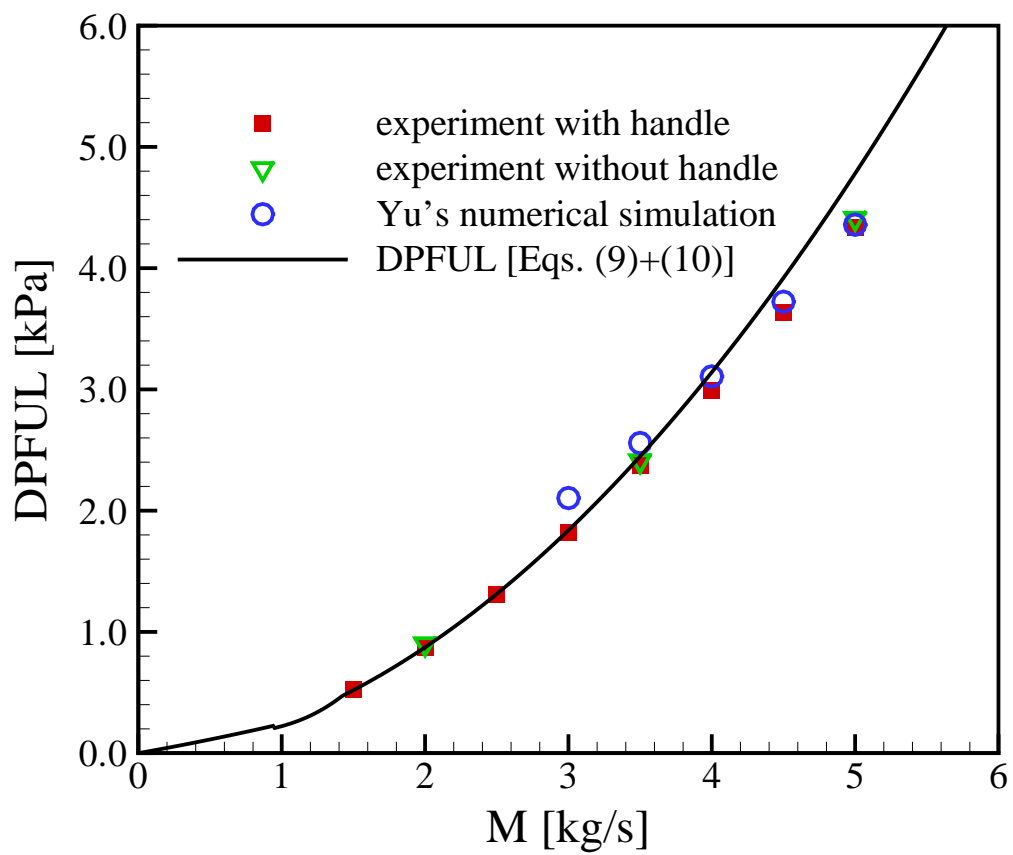


FIGURE 7.1: Pressure drop through the plate region in the assembly

7.2 Pressure drop through the bottom end fitting

The pressure drop through the bottom end fitting (DPOUT) was measured (Fig. 5.9). This is compared to the curve predicted by a 1-D correlation in Fig. 7.2. Note that DPOUT evaluated by Eqs. (4.11) and Eqs. (4.12) consists of two part: the pressure drop due to the abrupt contraction (DPOUT 1, region 2→3) and the pressure drop due to the gradual contraction (DPOUT 2, region 3→4) (see Fig. 4.6), respectively. They are arithmetically summed to estimate DPOUT. Note that the pressure drop without the handle is slightly higher than that with the handle (<5%), similar to the pressure drop in the plate region. In addition, the measured pressure drop at $M=2.5$ kg/s is corrected based on the fact that $DPTS=DPFUL+DPOUT$ since it only showed slightly different trend from the other data points, probably due to the experimental error (probably due to trapped air bubbles in the pressure tap tube).

The DPOUT curve evaluated by Eqs. (4.11) and (4.12) accurately predicted the pressure drop through the bottom end fitting (<8% error). As discussed in DPFUL, the pressure tap could be slightly influenced by the flow separation at the contraction step in the plate-free duct. This could be partially responsible for the lower DPOUT prediction than the experiment. On the other hand, DPOUT includes the complete minor pressure losses due to both the abrupt contraction and the gradual contraction. The separated flow due to the abrupt contraction may not be completely recovered downstream but the correlation includes this minor pressure loss. However, most of the minor pressure loss may occur at the front of the contraction step (the plate-free duct) and at the vena contracta (short downstream from this step). This results in a relatively small error.

The pressure loss in this region consists of minor loss and frictional loss. The minor loss consists of the pressure losses due to the abrupt contraction and the gradual contraction. From the DPOUT prediction, DPOUT 1 contributed to DPOUT by approximately 36 % at $M=1.5-5.0$ kg/s due to its relative short length (25.4 mm compared to 196.8 mm of the whole bottom-end fitting). However, the minor pressure losses are about 70 % of DPOUT. This suggests that the pressure drop in this region may result mainly from the minor pressure loss, rather than the frictional loss.

In summary, the pressure drop through the bottom end fitting can be relatively accurately predicted by the 1-D correlations. The pressure drop in this region may result mainly from the minor pressure losses.

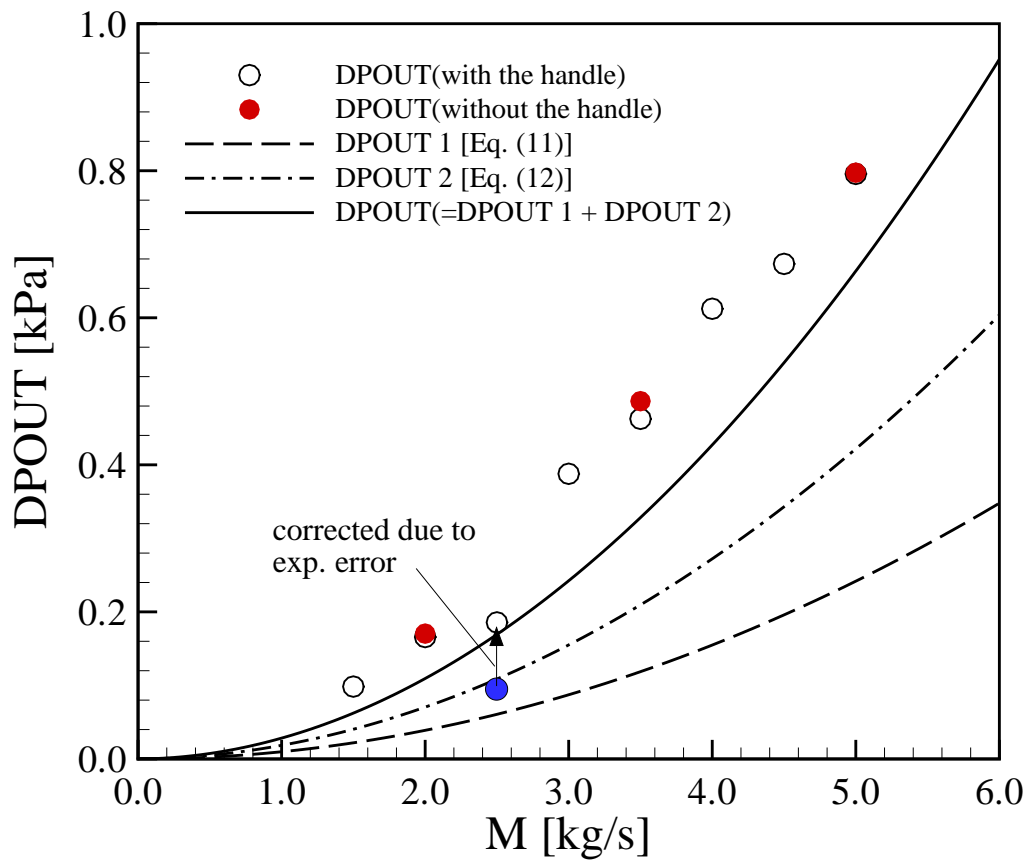


FIGURE 7.2: Pressure drop through the bottom end fitting in the assembly

7.3 Overall Pressure Drop

The pressure drops through the whole assembly, the plate region, and the bottom end fitting are shown in Fig. 7.3. The overall pressure drop (DPTS, region 0→4 in Fig. 4.6) consists of the pressure drop through the plate region (DPFUL) and the pressure drop through the bottom end fitting (DPOUT) (see Fig. 5.9). Thus, DPTS can be predicted simply by the summation of DPFUL and DPOUT from a 1-D correlation. However, DPTS was measured independently of DPFUL and DPOUT in the experiment. Note that the pressure drop without the handle is also slightly higher than that with the handle (<2%), similar to DPFUL and DPOUT in the previous sections.

The simple 1-D correlation predicted accurately DPTS (<4 % error except for 7 % at $M=5.0\text{kg/s}$). The experiment shows that DPFUL contributes to DPTS by more than 60 % due to the relative long length; the length of the plate region is 625.5 mm and that of the bottom-end fitting is 196.8 mm. Correspondingly, the pressure drop from the plate-free duct (including the abrupt flow expansion loss) to the bottom-end fitting should be responsible for less than 40 % of DPTS. From the DPTS prediction, the minor pressure losses along the assembly are less than 13 % of DPTS. This suggests that the pressure drop through the assembly occur mainly due to the frictional loss, especially through the plate region, rather than the minor losses. Therefore, the error of estimating the minor loss coefficients should not lead to a significant error of the pressure drop estimation through the whole assembly.

In summary, the 1-D correlation accurately predicted the pressure drop through the assembly (<8% error). The pressure drop through the whole assembly occurs mainly due to the frictional loss rather than the minor losses.

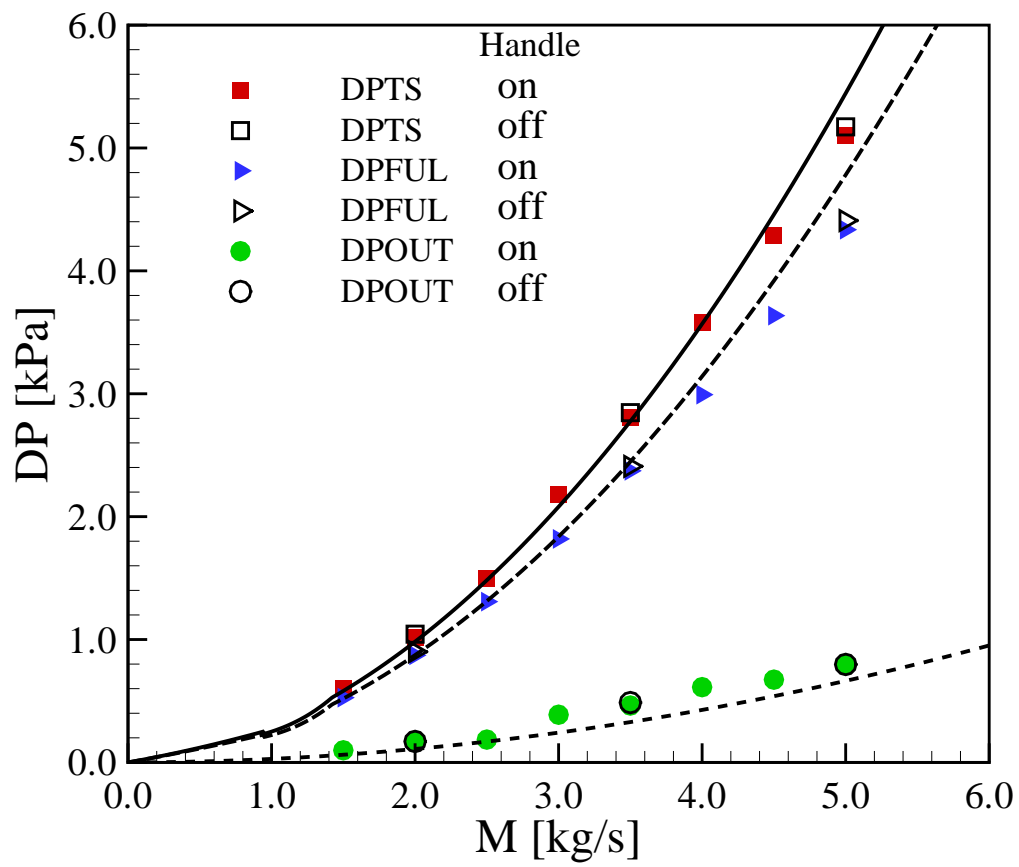


FIGURE 7.3: Pressure drops through the assembly

7.4 Summary

The pressure drops through the 18-plate assembly were measured and compared to a simple 1-D correlation. Generally, this comparison showed that the pressure drop through the 18-plate assembly can be predicted by a simple 1-D correlation accurately.

1. The experiment of the pressure drop through the plate region in the assembly agrees with the numerical simulation.
2. The simple 1-D correlation could accurately predict the pressure drop through the assembly: the plate region, the bottom end fitting and the whole assembly.
3. The pressure drop in the assembly is mainly due to the frictional loss, especially in the plate region but the minor pressure losses in the plate-free duct and the bottom-end fitting are not considerable.

Based on this information, the pressure drop in the various assemblies in the core can be predicted by 1-D correlation so that the assembly-to-assembly flow distribution in the core can be accurately evaluated.

The chapters 6 and 7 discussed the velocity profile in the channels and the channel-to-channel flow distribution from the velocity measurement, and the pressure drops through the assembly. The measurement error in these measured quantities will be analyzed in the following chapter 8 in detail.

Chapter 8

Measurement uncertainty

The simulation of the flow through the 18-plate assembly was conducted through the MNR flow simulator as described in Chapter 5. The velocity in the assembly channels, the pressure drop through the assembly, and the temperature and the flow rate through the experimental loop were measured, respectively. In this chapter, the uncertainty in the measurement of these parameters is individually analyzed, following the procedure of the ANSI/ASME Standard on Measurement Uncertainty [33].

8.1 Uncertainty in local velocity measurement in narrow channel

Laser Doppler Velocimetry (LDV) was used to measure the velocity in the 18-plate assembly. Since the LDV beam light scattered by moving particles in the flow is Doppler-shifted and Doppler shift frequency is directly proportional to the velocity of these particles, no calibration for the velocity measurement is required. Data acquisition errors and data reduction errors are very small, and thus they are neglected here. In the present experiment, therefore, the largest error in the velocity measurement is essentially associated with the error from positioning of the LDV measuring volume (a relatively long and narrow ellipsoidal shape) at the projected location in the narrow channels of the assembly. The measuring volume was controlled by the LDV traversing system (Section 5.3.1). It was positioned at the projected measurement point in the narrow rectangular channels (see Figures 5.8 and C.2). Since the channel thickness is very small (2.97 mm), however, it was very difficult to position the measuring volume at the exact projected locations, especially at the thickness-wise

(X) center in the channels. Thus, it is possible that the measuring volume can be sensitively deviated from the thickness-wise center due to its narrow thickness and the difficulty in controlling the traversing system. Although the traversing system was firmly positioned on the building floor, a slight movement from side to side at its upper part is possible. This can induce a relatively large deviation from the exact measurement points in the very narrow channels. For example, it was extremely difficult to re-position the measuring volume at the same point (especially at the thickness-wise center) in the channels by adjusting the traversing system. Thus, the traversing system and visual observation were normally used together to position the measuring volume at the measurement points.

8.1.1 Uncertainty in measurement of the width-wise velocity distribution

The width-wise (Y) velocity distribution in the channels at $M=2.0$ and 5.0 Kg/s with the handle is shown in Fig. 8.1. Note that the several velocity measurements at the same point were conducted.

Generally, the error bar shows that a relatively large error in the velocity measurement is limited to the channel corner, especially in the immediate proximity of the side plate. Only a small error is consistently observed in the wide region far away from the side plate. The error is generally less than 9%, but it is further reduced to less than 3% except at $Y=1$ mm. It is possible that the measuring volume was not positioned exactly at 1 mm away from the side-plate wall in the channel by adjusting the LDV traversing system to set the Y coordinate. This may lead to the relatively large error at $Y = 1$ mm. On the other hand, the error in channel 3 (less than 9% measurement error) is slightly larger than in channel 6 (less than 7%) in both cases. This may be related to the consistent observation of the slightly lower velocity in channel 3 for the velocity distribution through the channels (see Sections 6.5, 6.6 and 6.8). The measuring volume in channel 3 may be slightly deviated from its thickness-wise center in the Y direction. Note that the width-wise velocity measurement also contains the measurement error due to positioning the measuring volume at the thickness-wise center in the channel.

8.1.2 Uncertainty in velocity measurement at thickness-wise (X) center

Another factor contributing to the error in velocity measurement arises from positioning the measuring volume at the thickness-wise center in the channel. Fig. 8.2 shows the thickness-wise velocity distribution at three points in the channels. Note that the measuring volume was positioned only at 3 points near the thickness-wise center since the velocity at the thickness-wise center in the width-wise direction in the channels was to be measured in the present experiment.

The velocity distribution shows a reasonable trend for all the cases; the velocity at the thickness-wise center is generally measured higher than that at its adjacent points, as expected. The velocity at $x^* = \pm 0.33$ ($x = \pm 0.5$ mm) is less than 5% lower than that at the thickness-wise center ($x^* = 0.0$ ($x = 0.0$ mm)): $x^* = \frac{x}{h}$. However, Yu's numerical simulation showed that the velocity at $x^* = \pm 0.32$ ($x = \pm 0.47$ mm) is about 12% lower (Figure 5.23 [6]). Therefore, it can be deduced that the measuring volume at $x^* = 0$ in the present experiment was located probably near the thickness-wise center. It suggests that the method of the LDV traversing system with the aid of visual observation is sufficiently accurate to locate the measuring volume at the thickness-wise center in every channel.

The other way to evaluate the uncertainty in the velocity measurement at the thickness-wise center in the width-wise (Y) direction in the channels is to compare the nominal flow rate with the flow rate evaluated from the measured width-wise velocity distribution. This flow rate was very close to the nominal flow rate by considering the thickness-wise velocity distribution in the channels from the logarithm law (Section 6.10); its difference was less than 6%. This suggests that the velocity in the channels was generally measured very close to the thickness-wise center of the narrow channel in the Y direction despite the slight possibility for the measuring volume to be deviated from the channel center, such as in channel 3.

8.1.3 Summary

The error due to positioning the measuring volume at the projected velocity measurement point along the thickness-wise center in the width-wise direction is not large; a

relative large error is only limited to the channel corner. The velocity in the narrow channel was measured very close to its thickness-wise center from the observation of both the width-wise (Y) and thickness-wise (X) velocity-distributions in the channels. This is confirmed from the comparison of the nominal flow rate and the flow rate evaluated from the measured width-wise velocity distribution in the channels.

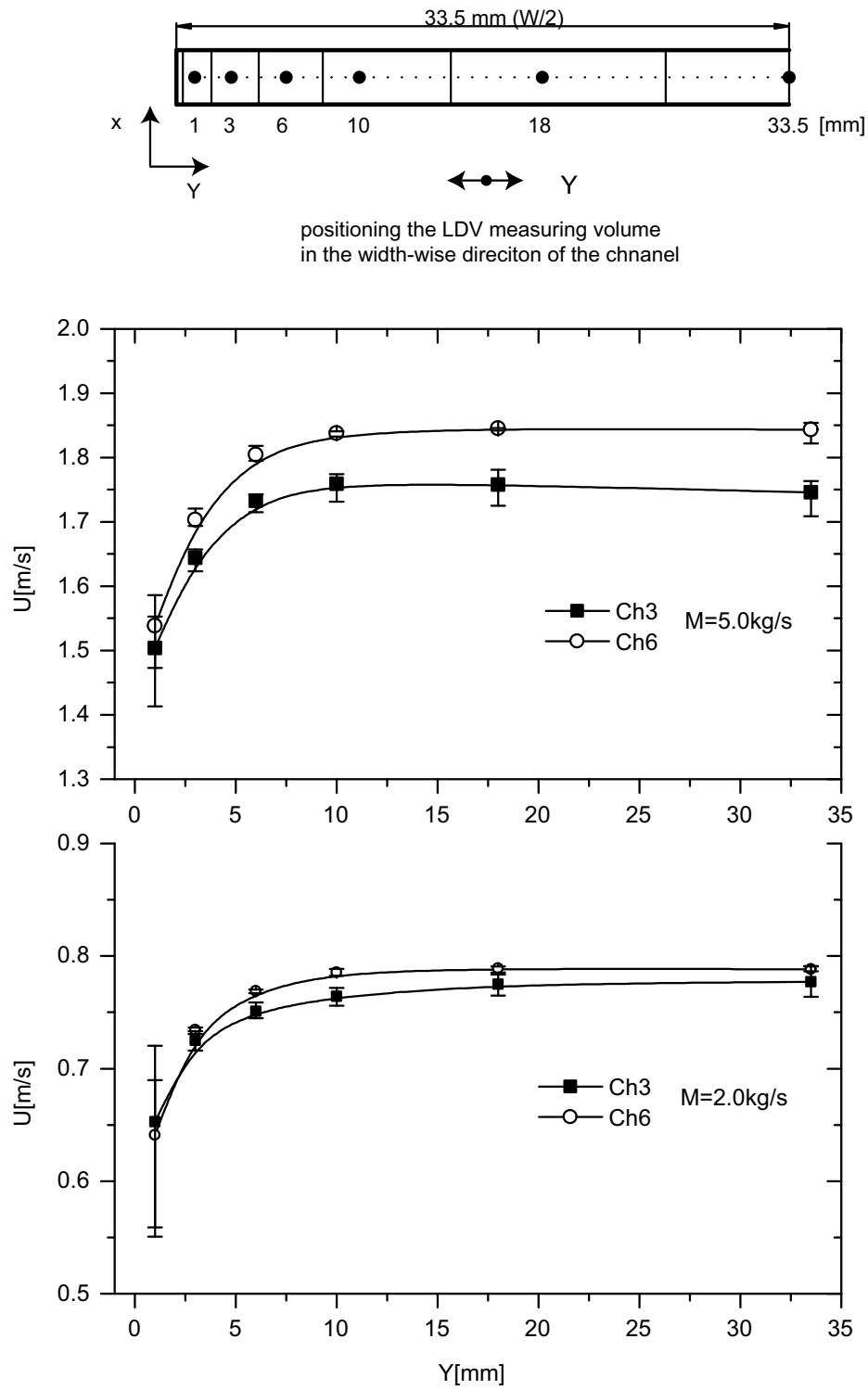


FIGURE 8.1: Widthwise (Y) velocity distribution in the channels

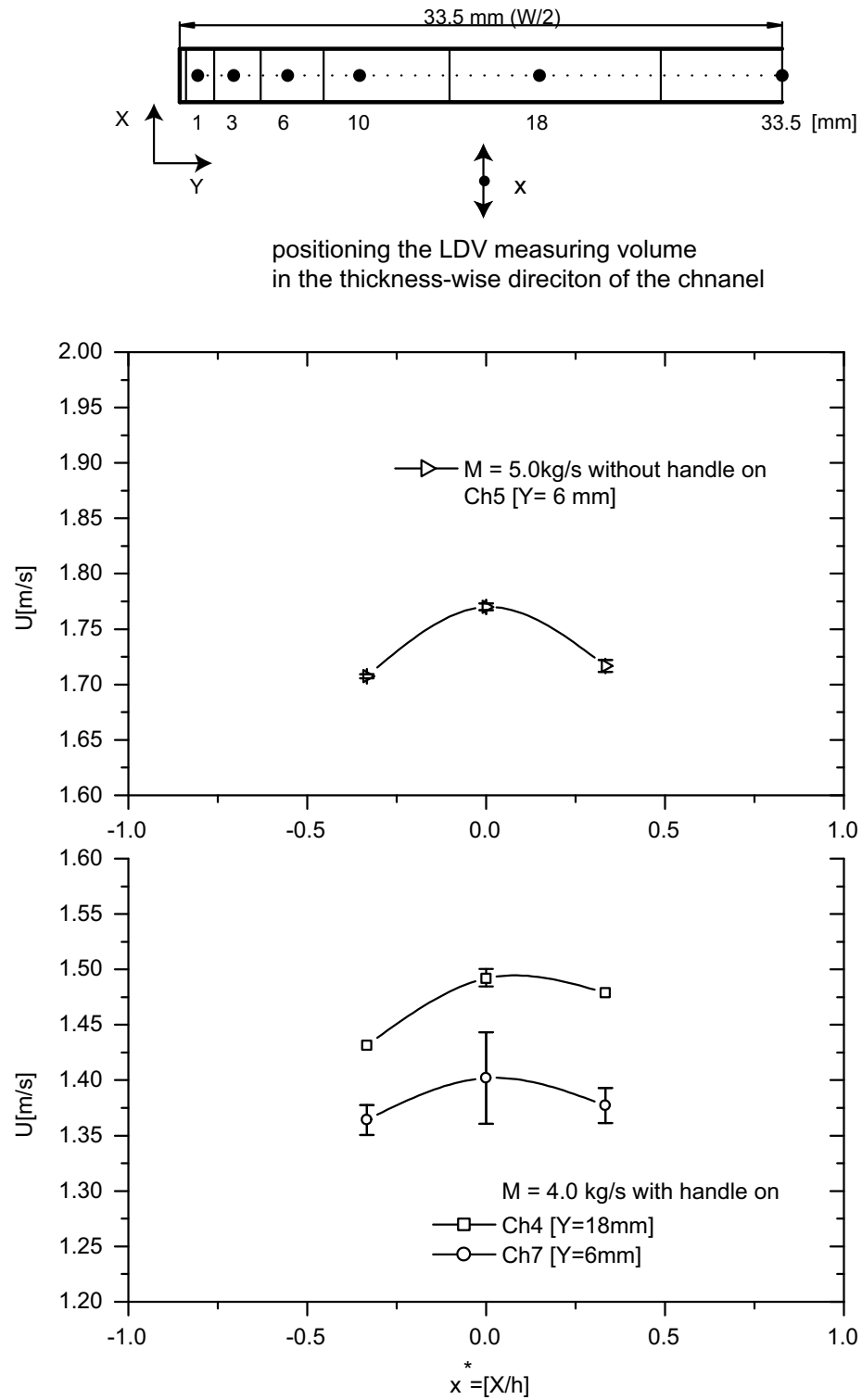


FIGURE 8.2: Thickness-wise (X) velocity distribution in the channels

8.2 Uncertainty in pressure drop measurement

The pressure drops through the 18-plate assembly and across the orifice meter were measured by the differential pressure transmitters from Rosemount Inc. All the pressure transmitters used were separately calibrated and their results are listed in Appendix B.2. The individual pressure transmitters have an overall uncertainty as shown in their calibration data. The result of the individual pressure drop measurement in the assembly is shown in Fig. 7.1 to 7.3 (Chapter 7). Its measurement error was calculated in each case. The uncertainty of the pressure drop measurement is conducted at the 95% confidence level (see Appendix H). These results are summarized in Table 8.1.

Generally, the measurement of all the pressure drops was very accurately conducted by the differential pressure transmitters within approximately $\pm 2\%$ with 95% confidence level except for the DPOUT measurement (the pressure drop through the bottom end fitting) at $M = 2.5\text{kg/s}$, which shows about 16% error. In that one case, there is a large difference between DPOUT and the quantity of DPTS minus DPFUL. This is related to the experimental error, probably due to trapped air bubbles in the pressure tap tube (see Section 7.2). Therefore, it can be concluded that the pressure measurement was conducted very accurately both in the 18-plate assembly and across the orifice meter within the uncertainty of $\pm 2\%$.

8.3 Uncertainty in flow rate measurement by orifice meter

A nominal mass flow rate through the MNR flow simulator was set by a combination of circulating pump, flow orifice, and flow control valve settings (Section 5.3.3). The uncertainty analysis in the flow rate measurement by the orifice meter was conducted at the 95% confidence level (Appendix H).

The flow rate measured by the orifice meter is a function of several parameters (Eq. B.5). The individual parameter errors may be propagated into the flow rate measurement. Since the errors due to the measurement of the diameters of the orifice meter, the experimental loop tube, and the temperature through the loop is very

TABLE 8.1: Summary of uncertainty analysis of the measurement of the pressure drop and the flow rate in the assembly

M[kg/s]	DP [kPa]	DPFUL [kPa]	DPOUT [kPa]	DPTS [kPa]	U_{rss} [%] of M
1.5	1.819 ± 0.009	0.527 ± 0.004	0.323 ± 0.002	0.830 ± 0.007	1.23
2.0	3.217 ± 0.017	0.900 ± 0.005	0.570 ± 0.004	1.443 ± 0.008	1.23
2.5	5.035 ± 0.041	1.308 ± 0.007	0.515 ± 0.081	2.119 ± 0.012	1.27
3.0	7.312 ± 0.031	1.819 ± 0.009	1.278 ± 0.027	3.075 ± 0.024	1.22
3.5	9.926 ± 0.047	2.395 ± 0.044	1.685 ± 0.008	4.056 ± 0.046	1.23
4.0	12.987 ± 0.053	2.993 ± 0.020	2.211 ± 0.012	5.175 ± 0.027	1.22
4.5	16.304 ± 0.163	3.635 ± 0.033	2.697 ± 0.021	6.313 ± 0.048	1.30
5.0	20.028 ± 0.391	4.410 ± 0.056	3.271 ± 0.057	7.670 ± 1.103	1.50

DP=pressure drop across the orifice meter,

DPTS=DPFUL+DPOUT,

U_{rss} is the relative overall uncertainty,

M=2.0, 3.5, 5.0 kg/s without the handle,

M=1.5, 2.5, 3.0, 4.5 kg/s with the handle.

small, their contribution is neglected here. The errors only due to the orifice meter discharge coefficient and the pressure drop measurement across the orifice meter was considered. The relative uncertainty in the flow rate measurement was calculated and its result is tabulated in Table 8.1. It is shown that the flow rate was measured within approximately 1.5% for all the cases. The largest error is only 1.50% at M=5.0 kg/s. Note that the largest contributor to the uncertainty is the discharge coefficient, C of the orifice meter; its error is 1.21%. It can be concluded that the flow rate measurement was conducted very accurately within the uncertainty of approximately $\pm 1.5\%$.

8.4 Uncertainty in temperature measurement

Temperature was measured in three locations along the experimental loop (Section 5.3.4), and the temperature was to be maintained at approximately constant temperature of 30 °C during the measurement. The result of the temperature measurement over the experimental range is shown in Fig. 6.3. The uncertainty in temperature measurement is also analyzed at the 95% confidence level (Appendix H). It is found that all the temperatures of T1, T2, and T3 through the experimental loop were measured within the uncertainty of ± 1.5 °C. Considering a known uncertainty of about 1 °C over the operating range of the T type thermocouple used, which was guaranteed by its manufacturer, the temperatures were very accurately measured.

8.5 Summary

The velocity in the channels, the pressure drop through the assembly, and the temperatures and the flow rate through the through the experimental loop were measured very accurately. The uncertainty analysis in these measurements shows:

1. The velocity measurement in the assembly channels was conducted very close to the thickness-wise center in the width-wise direction in the channels, from the analysis of the thickness-wise and width-wise velocity-distributions. This is confirmed from the comparison of the nominal flow rate and that evaluated from the width-wise velocity distribution, considering the thickness-wise velocity gradient in the channels.
2. The pressure drops through the 18-plate assembly and across the orifice meter were measured within an uncertainty of approximately $\pm 2\%$.
3. The uncertainty in the flow rate measurement evaluated from the measured pressure drop across the orifice meter is approximately $\pm 1.5\%$.
4. The temperatures along the experimental loop were measured within an uncertainty of ± 1.5 °C.

Chapter 9

Flow visualization in 18-Plate assembly

A direct flow visualization technique (DFV) was used to visualize the flow behavior in the assembly at low flow rates of $M = 0.8$ to 1.8 kg/s, using a chemical indicator (Section 5.6). The flow behavior was captured by photographic and video method by means of visual contrast. The flow visualization in the calming length duct, the top end fitting, and the plate-free duct just above the bottom end fitting is shown in Fig. 9.1 to 9.5.

9.1 Flow visualization in calming length

The calming length duct was inserted on the top of the simulated 18-plate assembly to simulate the inlet flow condition to the top end fitting in the central assemblies of the MNR core. To observe the flow development from the experimental loop to the calming length, flow behavior was visualized in the entire calming length.

The flow behavior in the calming length at $M=1.2$ kg/s is shown in the course of time in Fig. 9.1. The flow color changed from “Blue” to “Yellow” from the top of the calming length. The flow color changed slightly faster in the right-hand side of the duct but slower in its left-hand side from the figures (a) to (c). This suggests that the flow may be slightly deflected to the right-hand from the top of the calming length. It may be related to the diffuser and bell-mouth effect of 90° -flow stream change upstream of the calming length (Section 6.3). This slightly deflected flow to one direction at the inlet of calming length should be gradually recovered downstream. From the figures (d) to (f), however, the flow still shows a dark color in the left corner in its bottom. Thus, fully developed flow may not be completely attained.

In summary, flow visualization shows that the flow in the calming length has a slightly deflected development to one direction from its top, and may be developing toward the fully developed profile toward its bottom. However, a dark region in the left corner in its bottom shows that fully developed flow was not completely attained.

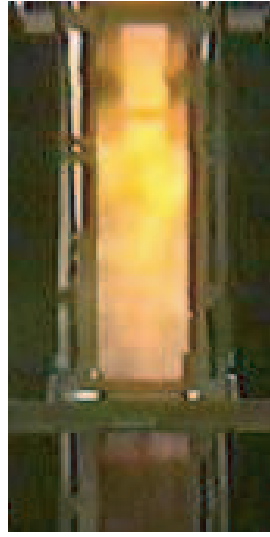
(a) $t = 0.0$ ms(b) $t = 7.8$ ms(c) $t = 23.4$ ms(d) $t = 39.0$ ms(e) $t = 54.6$ ms(f) $t = 93.6$ ms

FIGURE 9.1: Flow visualization in the course of time in the calming length duct at $M=1.2$ kg/s. Flow color changed from “Blue” to “Yellow”.

9.2 Flow visualization in top end fitting

The handle was positioned in the top end fitting of the assembly. It obstructed the flow path and should disturb the nearly symmetric and uniform flow from the calming length before the inlets of the channels (see Fig. D.1). To study this flow redevelopment past the handle, the flow behavior in the junction of the calming length and the top end fitting was visually captured. Fig. 9.2 and 9.3 show the flow behavior in this region at $M = 0.8$ and 1.2 kg/s. The white circle in the figures simply denotes the handle location.

Generally, the flow color change is fairly symmetric in both sides. This agrees well with the nearly symmetric and uniform velocity distribution at the bottom of the calming length ($Z = 725$ mm) in Fig. 6.5. The flow should be further developed downstream to the top end fitting. Thus, it can be deduced that the velocity distribution is virtually symmetric and the fully-developed flow may be nearly attained just above the top end fitting (Section 6.5).

Different flow behavior is observed in the top end fitting since the flow should be severely disturbed by the handle (Appendix D). This is visualized as relatively slower flow color change directly underneath the handle and faster change around the center of each half side. The flow color started to change first around the center of each half side but did not change for a while just underneath the handle around the duct center (see the figures (b) to (e)). This is similar to the possibly dumbbell-shape velocity distribution redeveloping past the handle through the inlets from one channel to another. This suggests that it be reasonable to assume a dumbbell-shape velocity distribution past the handle in the inlets of the channels. This flow entered the channels and led to the similar profile of the channel-to-channel flow distribution in the experiment with the handle (Sections 6.7 and 6.8.2).

In summary, it is shown that the flow in the top end fitting is nearly symmetric at the bottom of the calming length. Due to the handle in the top end fitting, the flow is considerably disturbed and redeveloping possibly to the dumbbell-shape velocity distribution past the handle. This flow development is clearly visualized as the flow color change.

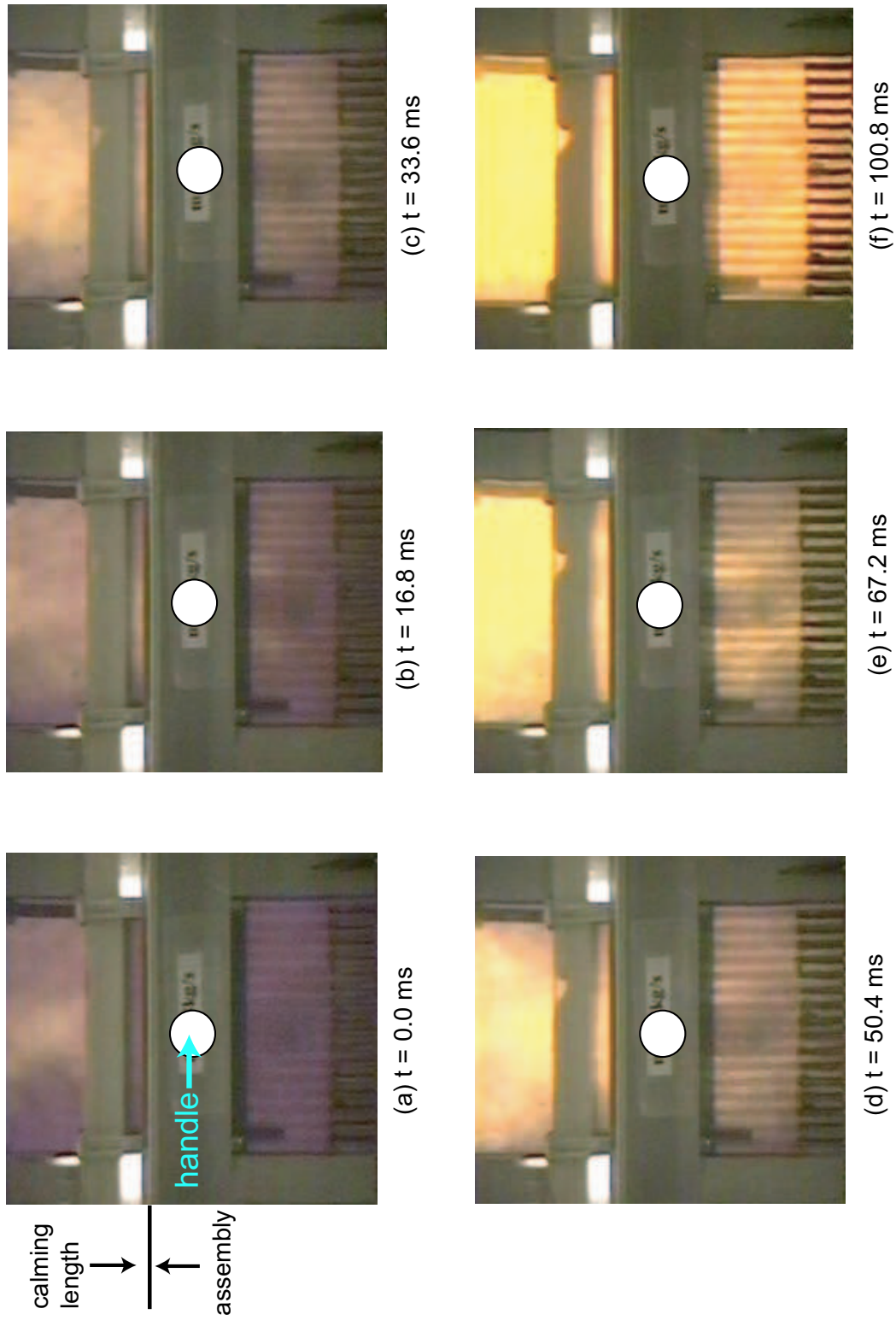


FIGURE 9.2: Flow visualization in the course of time in the junction of the calming length duct and the top end fitting at $M=0.8$ kg/s. Flow color changed from “Blue” to “Yellow”. While circle denotes the handle location

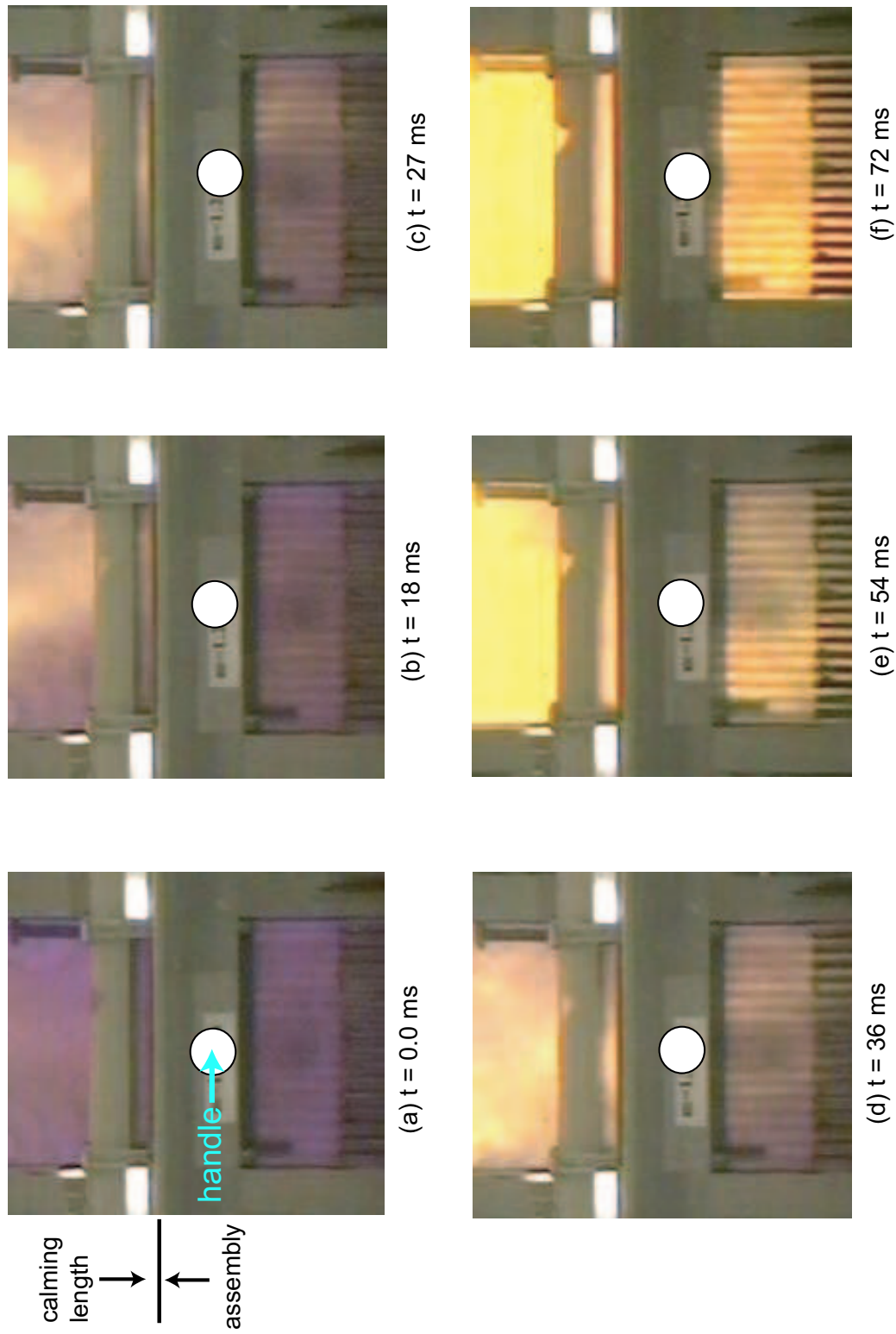


FIGURE 9.3: Flow visualization in the course of time in the junction of the calming length duct and the top end fitting at $M=1.2$ kg/s. Flow color changed from “Blue” to “Yellow”. While circle denotes the handle location

9.3 Flow visualization in plate-free duct

The flow in the plate-free duct undergoes the complex path of abrupt expansion from the plate region (multi-channel) to the plate-free duct and then abrupt contraction from this larger rectangular duct to the smaller circular bottom end fitting over a short length. This complex flow behavior in the plate-free duct was visualized to study the exit effect. Fig. 9.4 and 9.5 show the flow behavior in the plate-free duct at $M=0.8$ and 1.5 kg/s. The detailed behavior is not clearly visualized at the relatively high flow rate of $M=1.5$ kg/s, probably due to the limitation of the DFV technique, compared to the flow visualization at $M=0.8$ kg/s.

Both figures show that the flow in the plate-free duct is fairly symmetric. The flow color changed relatively slowly underneath the middle channels (8 to 10) and the outer channels (1 to 2 and 16 to 17). This is clearly observed as the remaining dark region in the course of time especially in Fig. 9.4 (a)–(c). However, the flow color changed more quickly underneath in between these channels. The relatively slower flow color change underneath the middle channels should result mainly from the possible dumbbell-shape velocity distribution (handle effect) because the middle channels should have the smallest exit loss (due to flow stream bending). The lower velocity just underneath the handle entered the middle channels and eventually should lead to the slower velocity in the multi-channel exits and the plate-free duct. By contrast, the slower flow color change underneath the outer channels in both sides may be associated with the lower velocity flow from the top end fitting due to the boundary layer near the side-plate walls and the relatively larger exit loss.

The flow stream bending from the outer channels is clearly visualized in the corners of both sides in the figures (a) to (c). The four corners in the plate-free duct consist of the large peripheral sub-channels whereas there are the large central sub-channels under the central channels. The flow from these peripheral sub-channels should bend severely to enter the bottom end fitting pipe, whereas the flow from the central sub-channels is directly downward to the bottom end fitting (see Fig. 4.4). This is visualized as relatively slower flow color change inside (or under) about a 45-degree imaginary line in the figures, whereas there is the relatively faster change outside this line. The remaining dark color even at $t=24$ ms of Fig. 9.4 (c) implies the eddy

formation in this corner-region. Its size may be large in the corners of the duct but small under the central channels where there are only small peripheral sub-channels.

Jet streams may form from the channel exit due to the abrupt expansion from the plate region to the plate-free duct. They were persistently observed as a series of clear color in between long dark bands under the plates in Fig. 9.4. These dark bands consequently enhanced the visualization of the jet stream from the channel exit and visualized the formation of vortex pairs in between the jets under the cross-sectional area of the plates due to abrupt expansion. These dark bands were preserved almost down to the circular bottom end fitting entrance underneath the central channels but became vague downstream of the outer channels. This may be because the jet streams (in between the dark bands) from the outer channels should bend to enter the pipe and those especially from the outermost channels may overlap from the angle of the camera. This produced the vague (mixed) flow color. The jet streams underneath the central channels (5 to 13) are visually observed to be straight downward. The initial region of these jets may be preserved almost down to the bottom end fitting, and seemed to interact with their adjacent jets near the bottom end fitting entrance. This was visualized as a series of relatively clear color in between the dark bands even near the bottom end fitting entrance in Fig. 9.4. However, the jet streams underneath the outer channels bent severely to enter the bottom end fitting due to the abrupt contraction and thus their length is shorter compared to the jet streams from the central channels. In addition, the extent of these jet streams bending is not significant in the central channels but slightly increased toward the outermost channels. Its relatively sharp bending is observed only in the small outermost corners of the plate-free duct. Thus, it can be assumed that the jet streams from the channel exit may be almost preserved in the plate-free duct before the bottom end fitting. This may reduce the pressure drop due to the sudden expansion from the multi-channel to the plate-free duct so that the 1-D correlation without considering this pressure loss may accurately predict the overall pressure drop (see Fig. 7.3).

In summary, the flow visualization in the plate-free duct clearly shows the complicated flow behavior between the plate region and the bottom end fitting. The flow is fairly symmetric from one channel to another, and the handle effect was clearly shown as the relatively slower flow color change under the middle channels (8 to 10). The

eddy formation in the corners of the duct and the flow stream bending (especially from the outer channels) are observed. In addition, the formation of the jet streams from the channels' exit is visualized and these jet streams are almost preserved down to the bottom end fitting entrance.

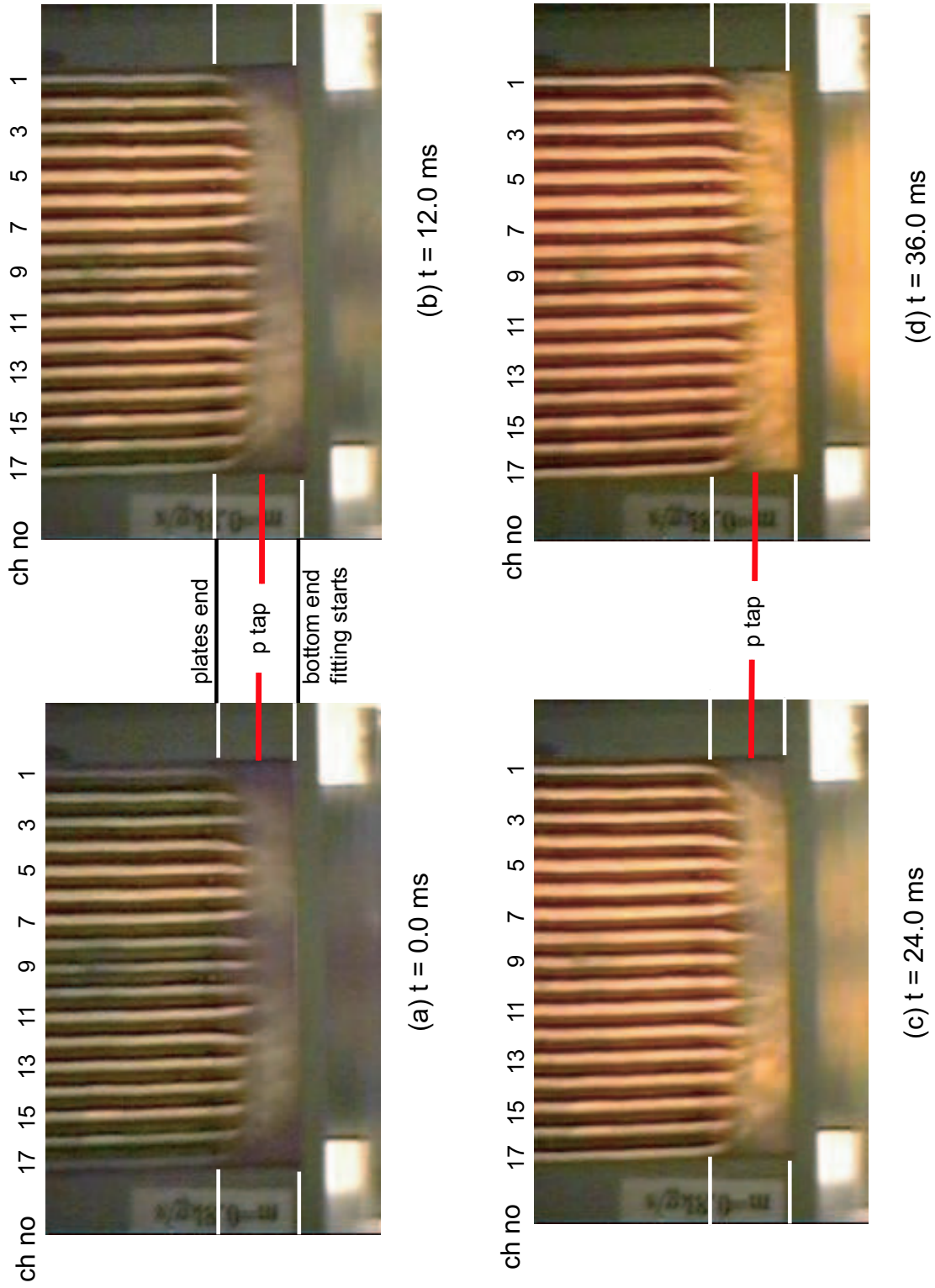


FIGURE 9.4: Flow visualization in the course of time in the plate-free duct at $M=0.8$ kg/s. Flow color changed from “Blue” to “Yellow”.

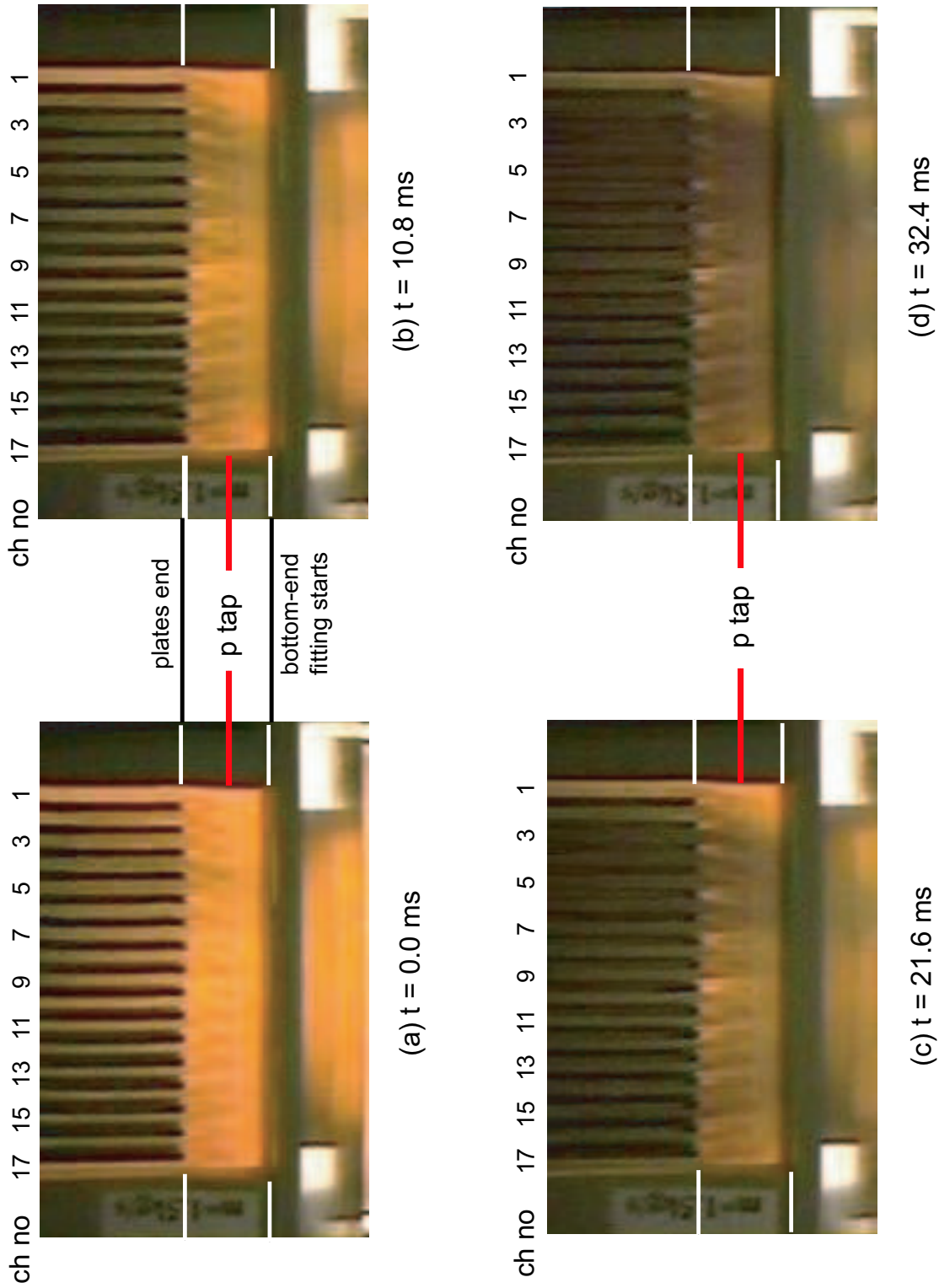


FIGURE 9.5: Flow visualization in the course of time in the plate-free duct at $M=1.2$ kg/s. Flow color changed from “Yellow” to “Blue”.

9.4 Summary

The flow visualization in the calming length duct, in the top end fitting, and in the plate-free duct by the DFV technique shows the detailed flow behavior.

1. The flow development in the calming length is slightly deflected to one side but nearly symmetric flow is attained downstream just above the top end fitting.
2. The flow past the handle is severely disturbed and redevelops to a possibly dumbbell-shape velocity profile in the inlets of the channels (handle effect).
3. The flow in the plate-free duct is symmetric from one channel to another. The handle effect on the flow through the channels, the flow stream bending (especially from the outer channels), and the jet stream formation from the channel exit are clearly visualized. These jet streams are almost preserved down to the bottom end fitting entrance.

Chapter 10

Conclusions

The hydraulic characteristics of the coolant flow in the standard 18-plate fuel assembly in the central region of the McMaster Nuclear Reactor core was investigated in the 18-plate assembly simulator by direct velocity measuring technique (LDV) from $M=2.0$ to 5.0 kg/s (i.e., $U_n=0.59\text{--}1.48$ m/s). The important results of the present study can be summarized as follows:

1. The calming length duct on the top of the simulated 18-plate assembly successfully simulated the inlet flow condition to the central assemblies in the MNR core from the pool. The velocity distribution in its bottom (just above the top end fitting) was sufficiently symmetric and uniform.
2. The entrance length in the channels is experimentally determined to be around $z^* = 21D_h$, which is accurately predicted by a simple 1-D correlation for turbulent regime. This also agrees well with the result of Yu's numerical simulation.
3. Evidence of a symmetric velocity profile through the 17 assembly channels due to the symmetric geometry of the simulated assembly is observed. The velocity distribution in the fully developed region ($Z=300$ mm) showed a relatively constant profile for $M=2.0\text{--}5.0$ kg/s. The width-wise velocity distribution in each channel shows a similar profile to parallel-plate flow and thus the flow in each channel can be approximated as flow between parallel plates. The comparison of the velocity profiles at $Z=1$ mm (near the channel exit) and at $Z=300$ mm (fully developed region) shows that the exit effect (flow stream bending due to the bottom end fitting on the velocity profile) is not significant. The velocity in the peripheral sub-channels in the outer channel is slightly decelerated, while the velocity in the central sub-channels in the central channels is slightly accelerated.

4. The channel-to-channel flow distribution in the present experiment shows a virtually constant and uniform profile at $M=2.0-5.0$ kg/s within a 5% difference. This agrees well with the flow distribution of Yu's numerical simulation in the same simulated assembly as in the present experiment. Among the previous hydraulic studies in the standard assembly, Blahnik's engineering calculation shows good agreement with the present experiment except for outermost channels 1 and 17 where the exit effect was overestimated. However, Rummens' experiment shows a significantly different profile: comparatively low in the outermost channels (1 and 17) and high in the central channels, in addition to a non-symmetric profile. This is because this study was conducted in the standard assembly probably without the handle and especially with a different inlet flow condition at the top end fitting.
5. The handle effect (its presence in the top end fitting) is not significant on the velocity profile in the channels and the channel-to-channel flow distribution. The velocity and average flow in the middle channels (8 to 10) with the handle was only slightly lower than those without the handle. Both distributions with the handle showed a similar profile to their dumbbell-shape velocity profile in the top end fitting.
6. The pressure drop through plate region in the present experiment also agrees well with that of Yu's numerical simulation. The pressure drop along the 18-plate assembly could be accurately predicted by a simple 1-D correlation. The pressure drop in the assembly is mainly due to the frictional loss, especially in the plate region but the minor pressure losses in the plate-free duct and the bottom-end fitting are not considerable (<13%). Based on this information, the pressure drop in the various assemblies in the core can be predicted by 1-D correlation so that the assembly-to-assembly flow distribution in the core can be accurately evaluated.
7. Flow visualization through the assembly at low flow rates by the DFV technique shows the velocity profile development in the calming length, the handle effect on the velocity distribution in the top end fitting, and the flow behavior in the plate-free duct. The velocity profile in the calming length duct is not uniformly

developed due to the flow stream change from the test loop and the abrupt expansion but it is nearly symmetric near its bottom. The handle in the top end fitting disturbs this nearly symmetric flow so that a slightly dumbbell-shape velocity distribution above the channel inlet is observed. The symmetric flow in the plate-free duct was observed and its profile is similar to the dumbbell-shape profile in the top end-fitting: lower velocity below middle channels 8 to 10 is clearly visualized. The jet streams forming from the channel exit and the formation of eddies in the corner of the plate-free duct are clearly observed. These jet streams are preserved almost down to the inlet of the bottom end fitting pipe.

Based on the present experiment, the velocity profile and the channel-to-channel flow distribution in a single assembly are influenced by 3 major factors: the entry loss from the reactor pool into the top end fitting (entrance effect), the handle presence in the top end fitting (handle effect), and the bottom end fitting (exit effect). Among these factors, the present experiment shows that both the handle effect and the exit effect were not significant. However, the handle effect in the standard 18-plate assembly should be slightly smaller than in the simulated assembly since the flow area obstructed by the handle is more distributed in the middle channels (8 to 10) (see legend in Fig. 6.15 and 6.16). Therefore, the most influential factor is the entrance effect. This is also confirmed from the comparison of the channel-to-channel flow distributions of Rummens' experiment, Blahnik's engineering calculation and Yu's numerical simulations. This suggests that the hydraulic characteristics through the individual assemblies could be significantly different depending on their type and especially their location in the MNR core.

From the present experimental results in the simulated 18-plate fuel assembly, in addition, the approximate channel-to-channel flow distribution in the 10-plate assemblies in the reactor core can be estimated by using certain weighting value without a detailed calculation.

Chapter 11

Recommendation for future work

The hydraulic characteristics through the 18-plate assembly were investigated in the simulated 18-plate assembly. It should be kept in mind that the present study was focused on the hydraulics in the standard 18-plate assembly in the central assemblies of MNR core, using the simulated 18-plate assembly with flat plates instead of the actual curved ones. Thus, the following improvements are recommended to be performed.

- It was found that the entrance effect on the velocity distribution and the channel-to-channel flow distribution in the assembly was significant. The present experiment simulated the inlet flow from the MNR pool into the assembly only for the central assemblies in the MNR core. However, the inlet flow condition may vary significantly depending on the location of the various assemblies in the MNR core, as illustrated in Fig. 4.1 (a). It is thus instructive to simulate the possible various inlet flow conditions to the assemblies for more complete investigation. To simulate various inlet flow conditions into the assemblies, for example, several (minimum 9 assemblies) can be placed in a large container, similar to the experimental setup of Rummens' (see Fig. 4.1 in Reference [4]). In this arrangement with several different types of assemblies (10-plate, control rod assemblies, etc), the outer 8 assemblies may sufficiently simulate various inlet flow conditions in the core.
- The present experiment did not include the curvature effect on the flow in the 18-plate assembly. Slightly different flow behavior may occur in the plate-free duct due to this curvature although the present study showed that the exit effect was not important factor. Thus, it is necessary to investigate the flow in

the assembly with the curved plates to study the difference of this exit effect due to the curvature of the plates.

- The hydraulic characteristics only in the 18-plate assembly were investigated in the present study. For safety analysis in the MNR, the flow in the other types of the assemblies (i.e., 10-plate assembly, irradiation sites, and etc) should be examined since the core flow distribution from one assembly to another should be affected by their relative flow resistance depending on their location in the core and their type.

In addition, the present study did not consider the temperature effect on the flow in the channels in the 18-plate assembly. In nominal operation of the MNR, however, the coolant temperature in the channels will slightly increase from their top to bottom. The axial temperature profile along the channels should affect the coolant properties (viscosity and density): the viscosity and density of the coolant should decrease with the temperature increase for liquid phase. This should lead to the slight increase of the Reynolds number and the coolant velocity in the channel since $\Delta p_{\text{ext}} \sim \mu^{0.25} \rho^{0.75} u^{1.75}$ with $f = 0.316/Re^{0.25}$ ($4000 < Re < 10^5$) for a given fixed external pressure difference (Δp_{ext} , driving force of the coolant flow). In contrast, the buoyancy force effect (upward flow force compared to the downward coolant flow) due to the density decrease may not be significant before boiling in the parallel flow channels occurs. These facts suggest that the flow velocity in these channels should be slightly higher and the flow should be slightly more turbulent than in the present study at the given mass flow rate. However, this temperature effect on the flow should not be significant because both of the slight velocity increase and the buoyancy force effect should compensate each other. Thus the result of the present study should be valid before boiling in the channels occurs.

Based on the good agreement between the experimental data and the prediction by a 1-D correlation, the pressure drop in various assemblies (10-plate assemblies, control rod assemblies, etc.) from their plate region to bottom end fitting can be approximately estimated by using an appropriate 1-D correlation for the given assemblies. However, it should be noted that the entrance effect should be included for the estimation of the total flow resistance, depending on the location of the vari-

ous assemblies in the core. These estimations can be used to estimate the core flow distribution from one assembly to another in the core.

References

- [1] S. E. Day, “Power-Peaking Factors in MNR”, MNR TN-2001-07-04, 2001.
- [2] P. C. Ernst, “MNR Heat Transfer Calculations for 5 MW Operation”, MNR TR-1972, 1972.
- [3] S. I. Osamusali, J. S. Chang, and P. Ernst, “Heat transfer and flow studies of mcmaster nuclear reactor fuel element”, Proceedings of the 12th Simulation Symposium on Reactor Dynamics and Plant Control (CNS), Paper No. 2A-5, 1986.
- [4] H. E. C. Rummens, J. S. Chang, and P. Ernst, “Thermalhydraulic Simulation for McMaster Nuclear Reactor”, CNS 14th Annual Nuclear Simulation Symposium Proceedings, April 25–26, 1988.
- [5] C. Blahnik, “Assessment of MNR Core Flow Distribution Tests”, MNR TN-2001-06, 2001.
- [6] R. Yu, “The Numerical Investigation of Turbulent Flow and Heat Transfer in the 18-plate Nuclear Fuel Assembly in McMaster Nuclear Reactor”, Master Thesis, McMaster University, 2002.
- [7] P. J. Kreyger, W. A. Essler, and W. Dellmann, 1970. “In-core Heat Transfer in MTR Plate Type Fuel Elements”, Nucl. Eng. Des. 12, 231–248.
- [8] McMaster Nuclear Reactor, “Mcmaster Nuclear Reactor safety report”, MNR-1972, 1972.
- [9] Wm. J. Garland, “Thermalhydraulic Modeling of the McMaster Nuclear Reactor”, MNR TR-97-04, 1997.
- [10] S. E. Day, “MNR Core Component Technical Specifications”, MNR TR-98-01-Rev. 1, 1998.
- [11] I. E. Idelchik, “Handbook of Hydraulic Resistance”, 2nd Ed., Hemisphere Publishing, 1986.
- [12] J. P. Harnett, J. C. Y. Koh, and S. T. McComas, “A comparison of predicted and measured friction factors for turbulent flow through rectangular ducts”, Int. J. of Heat Transfer, pp. 82–88, February, 1962.

- [13] F. M. White, "Fluid Mechanics", 2nd Ed., New York: McGraw-Hill, 1994.
- [14] H. Schlichting, "Boundary Layer Theory", 7th Ed., McGraw-Hill, 1978.
- [15] R. D. Blevins, "Applied Fluid Dynamics Handbook", Van Nostrand Reinhold, 1984.
- [16] R. K. Shah, "A comparison of laminar hydrodynamic entry length solutions for circular and noncircular ducts", *J. of Fluids Engineering*, vol. 100, pp. 177–179, 1978.
- [17] G. Beavers, E. Sparrow, and R. Magnuson, "Experiments on hydrodynamically developing flow in rectangular ducts of arbitrary aspect ratio", *Int. J. of Heat Transfer*, vol. 13, pp. 689–702, 1970.
- [18] W. J. Garland, "Single phase friction factors for MNR thermal-hydraulic modeling", MNR-TR 98-02, 1998.
- [19] O. C. Jones, "An Improvement in the Calculation of Turbulent Friction in Rectangular Ducts", *J. of Fluids Engineering*, pp. 173–181, 1976.
- [20] M. S. Quraishi and T. Z. Fahidy, "Indicator and precipitation technique for direct flow visualization", *Proceedings of the 3rd International Symposium on Flow Visualization*, pp. 71–75, 1983.
- [21] M. S. Quraishi and T. Z. Fahidy, "A flow visualization technique using analytical indicators: Theory and some applications", *Chemical Engineering Science*, vol. 37, no. 5, pp. 775–780, 1982.
- [22] A. Klein, "Review: Turbulent developing pipe flow", *J. of Basic Engineering*, vol. 103, 1981.
- [23] A. R. Barbin and J. B. Jones, "Turbulent Flow in the Inlet Region of a Smooth Pipe", *J. of Basic Engineering*, pp. 29-33, March 1963.
- [24] E. Logan Jr., and J. B. Jones, "Flow in a Pipe Following an Abrupt Increase in Surface Roughness", *J. of Basic Engineering*, pp. 35-40, March 1963.
- [25] W. M. Kays, "Loss Coefficient for Abrupt Changes in Flow Cross Section with Low Reynolds Number Flow in Single and Multiple-Tube Systems", *Transactions of the ASME*, pp. 1067-1074, November 1950.
- [26] R. P. Benedict, N. A. Carlucci, and S. D. Swetz, "Flow Losses in Abrupt Enlargements and Contractions", *J. of Engineering for Power*, pp. 73-81, January 1966.

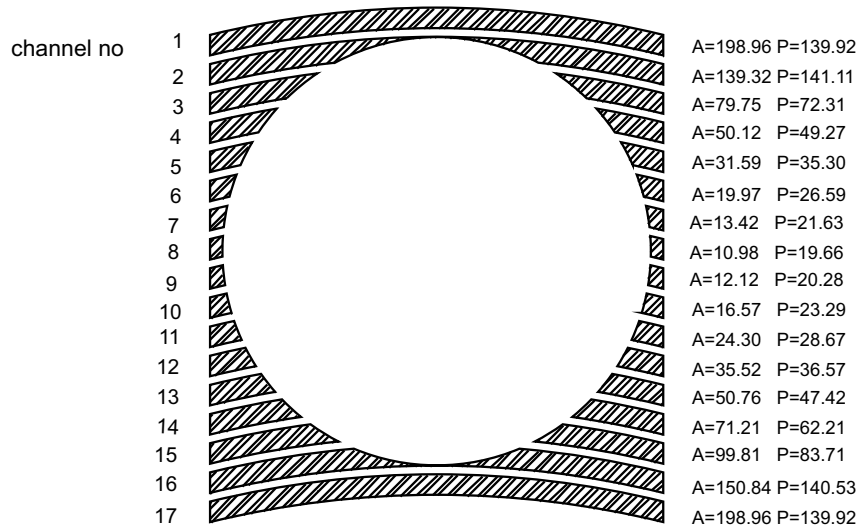
- [27] G. A. Whan and R. R. Rothfus, "Characteristics of Transition Flow Between Parallel Plates", *A.I.Ch.E. Journal*, Vol. 5, No. 2, pp. 204-208, 1959.
- [28] J. Vlachopoulos, "Fundamentals of Fluid Mechanics", Dept. of Chemical Engineering, McMaster University, Hamilton, Canada.
- [29] M. S. Quraishi, D. Koroyannakis, and W. F. Waters, "A study of combined forced and natural convection flow using an analytical indicator flow visualization technique", *Proceedings of the 3rd International Symposium on Flow Visualization*, pp. 743-747, 1983.
- [30] V. Saph and E. H. Schoder, "An Experimental Study of the Resistance to the Flow of Water in Pipes", *Trans. ASCE* 51 (1903) 944.
- [31] D. Wilkie, M. Cowin, P. Burnett, and T. Burgoyne, "Friction Factor Measurements in a Rectangular Channel with Walls of Identical and Non-Identical Roughness", *Int. J. Heat Mass Transfer*, Vol. 10, pp. 611-621, 1967.
- [32] C. Blahnik, "Coolant Flow Assessment within 18-Plate Fuel Assembly for MNR", MNR TR-2000-15, 2000.
- [33] ANSI/ASME PTC 19.1, Supplement to Performance Test Codes, Instruments and Applications. Part I: Measurement Uncertainty, The American Society of Mechanical Engineer, 1985.
- [34] E. I. Dekam and J. R. Calvert, "Pressure loss in sudden transitions between square and rectangular ducts of the same cross-sectional area", *Int. J. Heat and Fluid Flow*, vol. 9, no. 1, 1988.

Appendix A

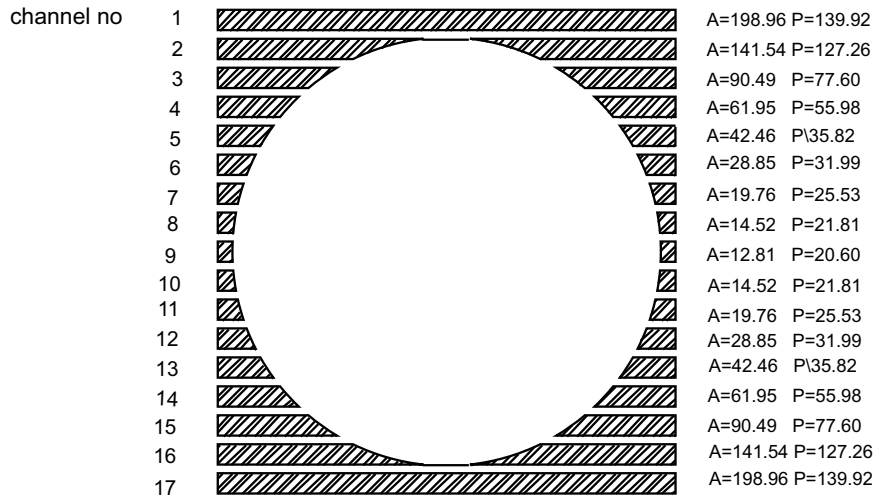
18-Plate assembly flow simulator

A.1 Comparison of standard 18-plate assembly and simulated 18-plate assembly

The standard 18-plate assembly is compared to the simulated one in detail. The physical channels in both assemblies can be divided into two parts as shown in Fig. A.1 and A.2. The “central” sub-channels are those aligned with the circular entrance into the bottom end fitting, while the “peripheral” sub-channels are not aligned with this entrance, as illustrated in Fig. 4.4. The cross-sectional area (A) and the wetted perimeter (P) of the central and peripheral sub-channels in all the channels were calculated from a scaled drawing as shown in Fig. A.1 and A.2. Their A and P in the standard assembly are compared with those in the simulated one in Fig. A.3. For the “central” sub-channels, A in the simulated assembly are slightly larger in channels 2 to 8 and slightly smaller in channels 10 to 16 than A in the standard one, and vice versa for the “peripheral” sub-channels. The difference is only within 1–6%. P for “central” sub-channels in the simulated assembly are slightly longer in channels 2 to 8 and slightly shorter in channels 10 to 16 than in the standard one, which is very similar to A comparison. However, for the “peripheral” sub-channels, P of channels 2, 5 and 16 in the simulated assembly are shorter ($\approx 10\%$) than P in the standard one, but the other sub-channels shows the same tendency as the A comparison.

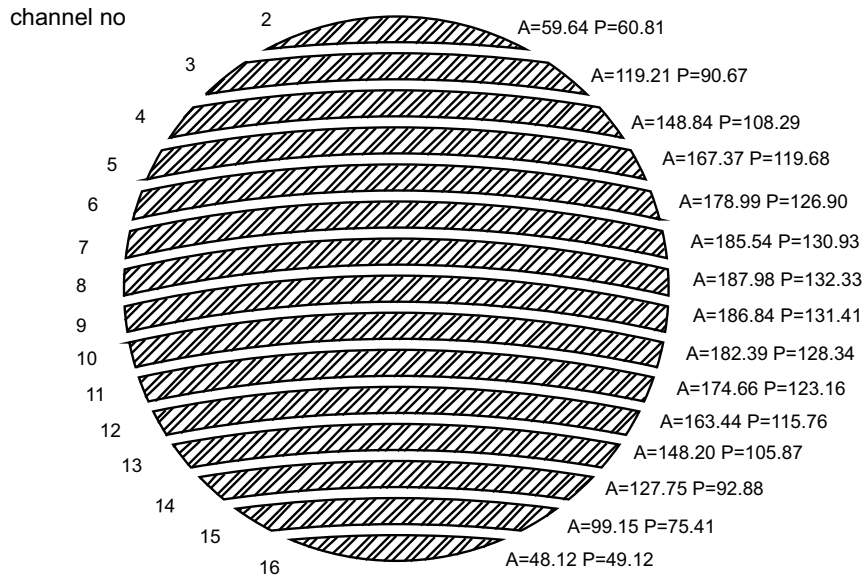


(a) peripheral channels in standard 18-plate fuel assembly

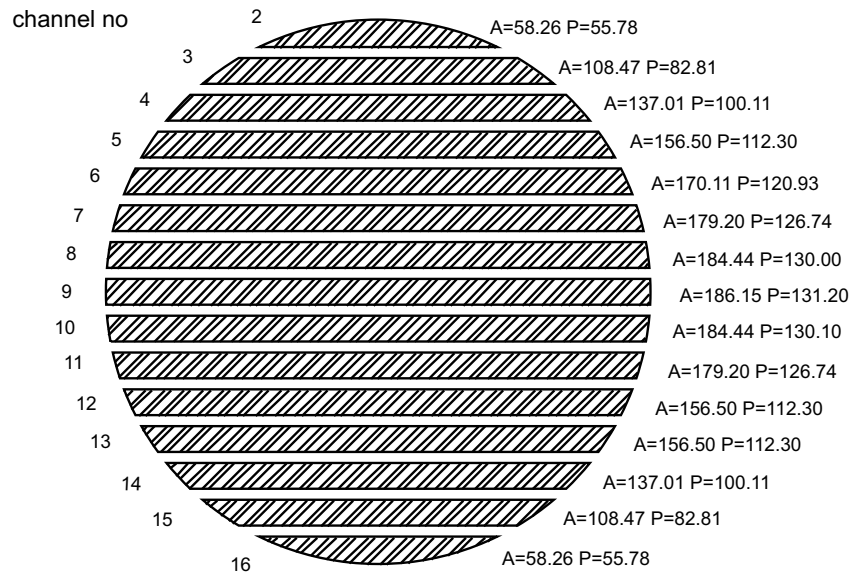


(b) peripheral channels in simulated 18-plate fuel assembly

FIGURE A.1: Comparison of cross-sectional areas (A) and wetted perimeters (P) in the peripheral sub-channels of the standard assembly and the simulated assembly.



(a) central channels in standard 18-plate fuel assembly



(b) central channels in simulated 18-plate fuel assembly

FIGURE A.2: Comparison of cross-sectional areas (A) and wetted perimeters (P) in the central sub-channels of the standard assembly and the simulated assembly

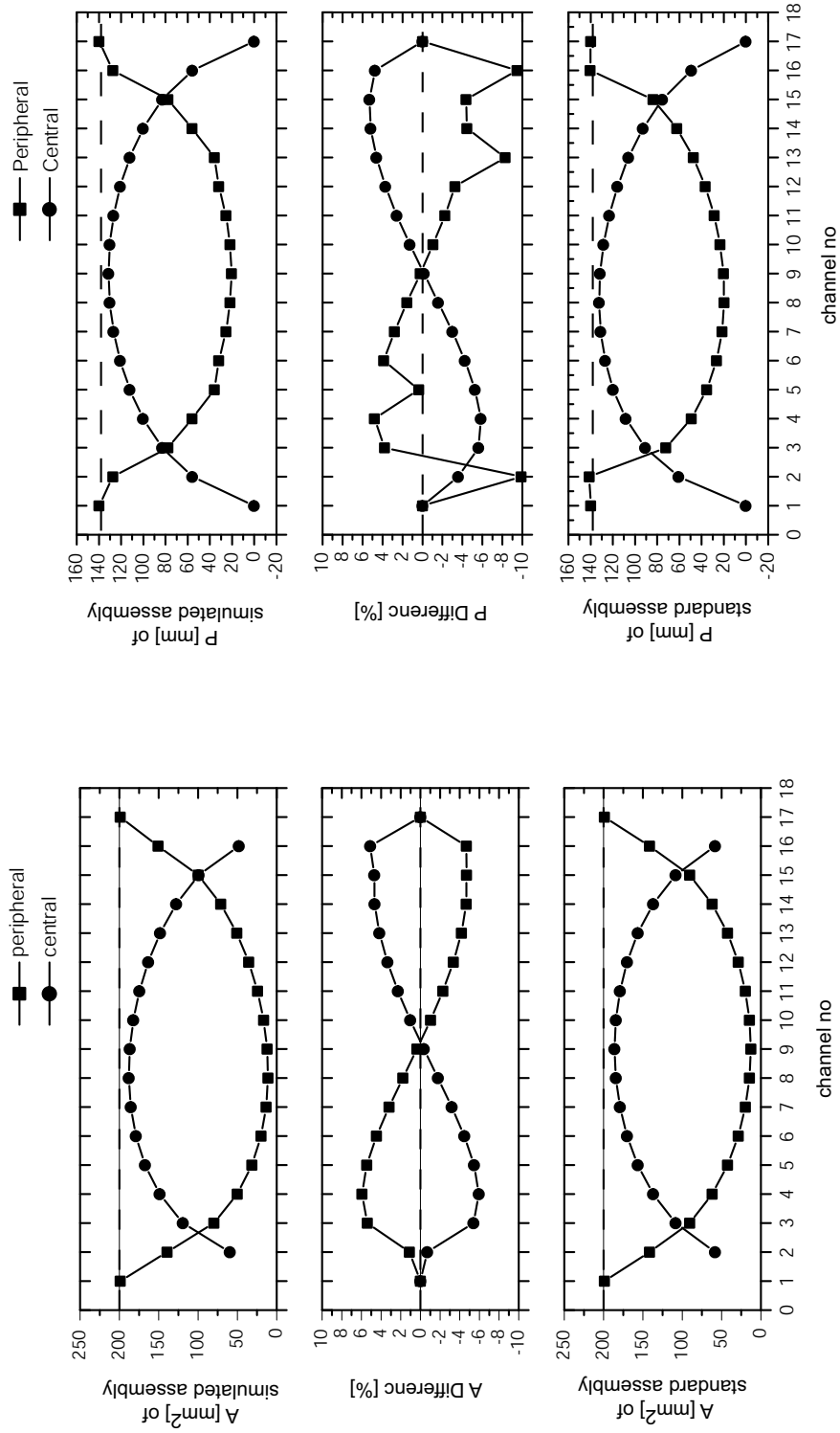


FIGURE A.3: Comparison of the standard assembly and the simulated assembly: (A) cross-sectional area and (B) wetted perimeter of the central and the peripheral sub-channels

A.2 Inspection of test section

The Al plates for 16 fuel plates, the acrylic sheets for two side plates, and two dummy plates were inspected before assembling the test section. This inspection result of the Al plates' thickness is shown in Fig. A.4. The thicknesses of the Al plates were ranged from 1.24 to 1.27 mm, which is within its specification of 1.27–0.05 mm. Their width was measured 73.35 to 73.38 mm, and their height was measured 625.0 to 626.0 mm, which is only slightly longer than its specification of 625.5 ± 0.4 mm. The distribution of the thickness, width, and length was uniform, and their surface condition was acceptable without severe scratches. For the acrylic sheets, their thickness was measured at several spots in every side plate. Its distribution in each side plate was uniform. The two acrylic sheets of the most uniformly-distributed thickness were selected for the side plates of the test section because the LDV beam should pass through those side plates. The others were used for the calming length duct and the two dummy plates of the assembly.

After assembling the side plates and the dummy plates for the calming length duct and the test section, the 16 Al plates were inserted into the test section. The dimension of the flow area in the calming length and in the test section was measured. The channel thicknesses of the 17 individual flow channels was also measured at their top end and bottom end as shown in Fig. A.5 and A.6. The measured dimensions are very close to the specified one within 0.5% error except the length in the calming length, which is only less than 0.7% shorter. The thickness of the flow channels was measured as 2.97 to 3.02mm, which is within its specification of 3.00 mm ($0.289 \text{ mm} (\text{min}) \leq t_w \leq 3.16 \text{ mm} (\text{max})$).

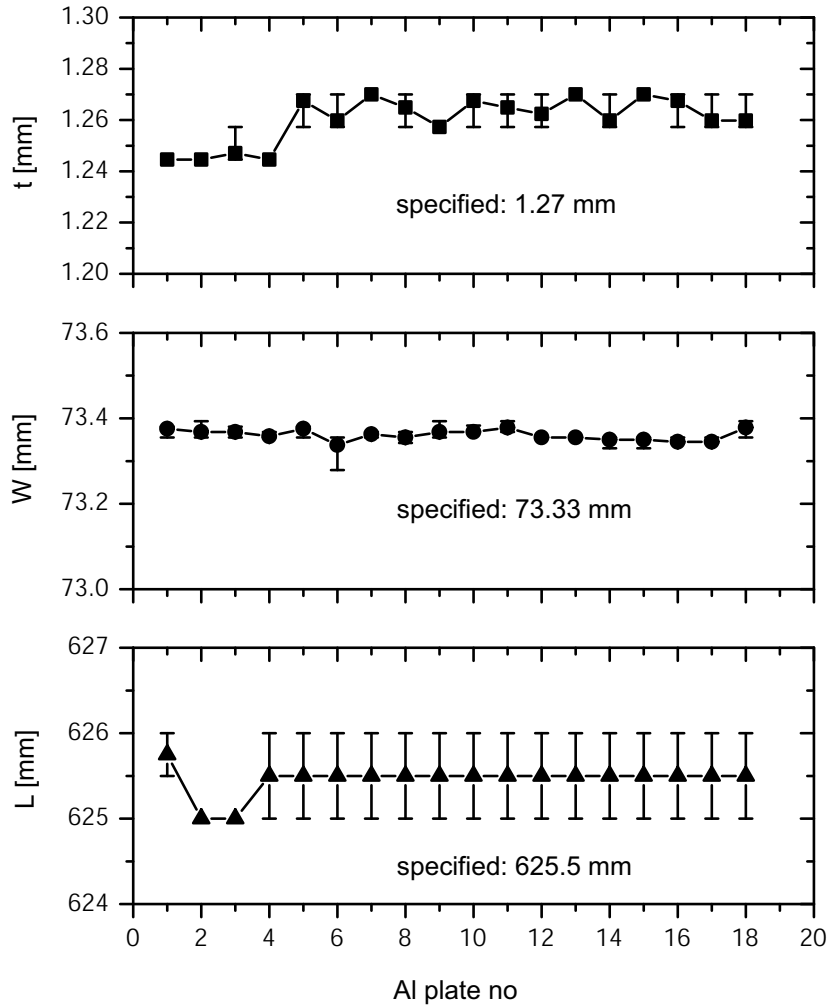
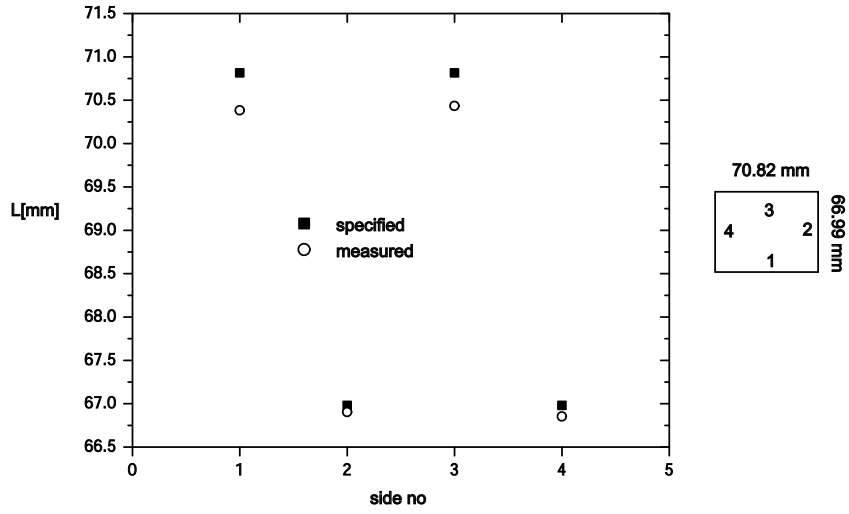
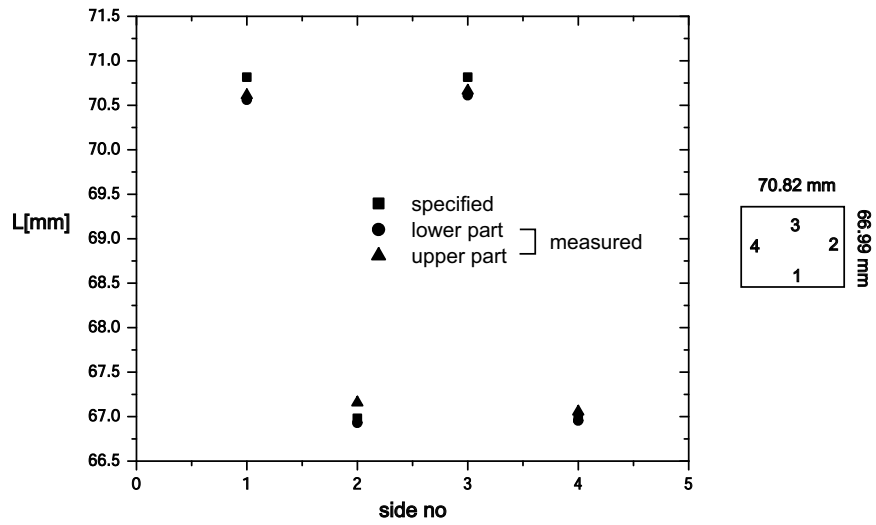


FIGURE A.4: Result of the thickness (t_w), width (W), and height (L) measurements of 17 Al plates in the simulated 18-plate assembly



(a) Dimension in calming length



(b) Dimension in test section

FIGURE A.5: Inspection result of the calming length and test section

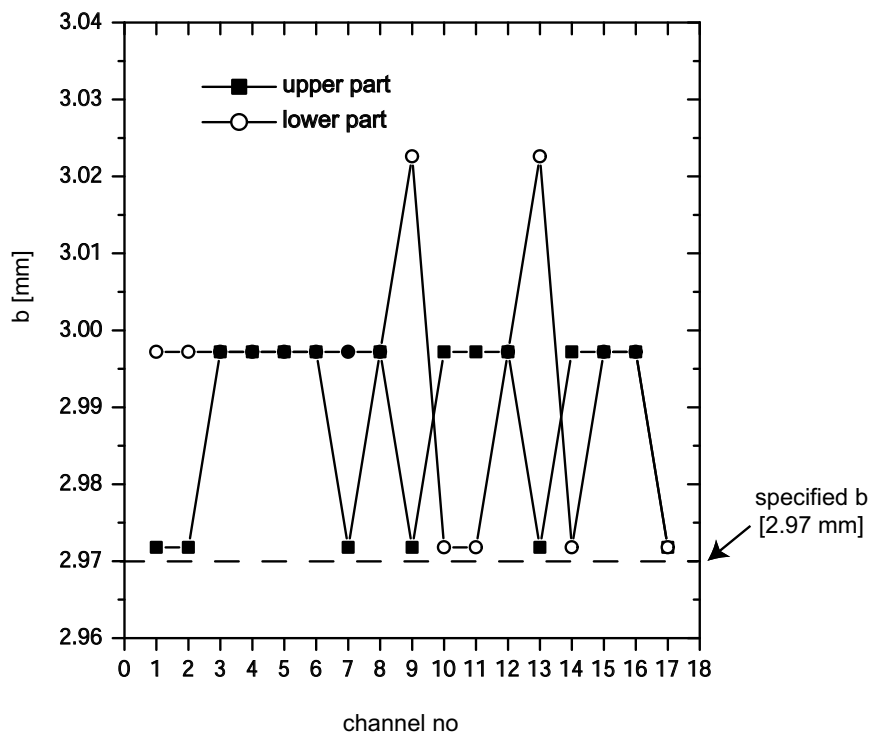


FIGURE A.6: Possible inflow streams to the top end fittings of the assemblies from the reactor pool and power density distribution in the reactor core

Appendix B

Measurement instruments

B.1 Laser Doppler Velocimetry

The single beam LDV used in the present study consisted of a 2 watt Lexel 95-2 Argon-Ion Laser unit, TSI focussing (120, 250, and 600 mm focal length) and receiving optics, a TSI signal processor (counter type), photodetector, and oscilloscope. Its layout is illustrated in Figure B.1. Argon-ion was used as a laser source and the laser beam was connected to the optic unit by fiber cable. The on-axis backscattering method was employed due to the limitation in experimental facility; the test section was attached to a large frame of additional structure and therefore laser beam could not penetrate through this structure for forward scattering method. Thus transmitting optics and receiving optics were placed on the same side of the test section. The oscilloscope was linked on-line to the signal processor, and several key parameters were set to obtain optimum signal during preliminary testing. The output frequency of the LDV measurement was input to the data acquisition system for further processing.

To measure the velocity of the coolant flow in the channels in the test section, the laser beams must pass through a window before focusing as depicted in Figure B.2. Hence, the focal distance must be slightly changed. To find the new focal distance, F , the following equation is derived from the theory of optics:

$$F = F_D \frac{\tan \varphi_1}{\tan \varphi_3} + t_w \left[1 - \frac{\tan \varphi_2}{\tan \varphi_3} \right] + d_f \left[1 - \frac{\tan \varphi_1}{\tan \varphi_3} \right] \quad (\text{B.1})$$

where, F =actual focal distance [mm]; F_D =focal distance of lens, $F_D=250$ mm; t_w =thickness of the window, Plexiglas in present study $t_w=12.7$ mm; d_f =distance from the front of the lens to the window, [mm]; η_1 =reflective index of the medium between the transmitting lens and the window, for air, $\eta_1=1.00$; η_2 =reflective index of the window, for

Plexiglas $\eta_2=1.49$; η_3 =refractive index of the fluid, for water $\eta_3=1.33$; φ_1 =angle the incident beam makes with the optical axis, $\varphi_1 = 5.52^\circ$ (half angle of lens); φ_2 =angle the beam within the window makes with the optical axis; φ_3 =angle that the beam within the fluid makes with the optical axis The angles of φ_2 and φ_3 can be calculated from Snell's law:

$$\eta_1 \sin\varphi_1 = \eta_2 \sin\varphi_2 = \eta_3 \sin\varphi_3 \quad (\text{B.2})$$

Therefore, the actual focal distance can be calculated from the measurement of d_f by Eq. B.1. In actual application, the LDV measuring volume in the flow channels in the test section was manually positioned at the desired points in the Y direction, which controlled the d_f . The X and Z coordinates were controlled by the X-Z coordinate controller with its position on display as discussed in Section 5.3.1.

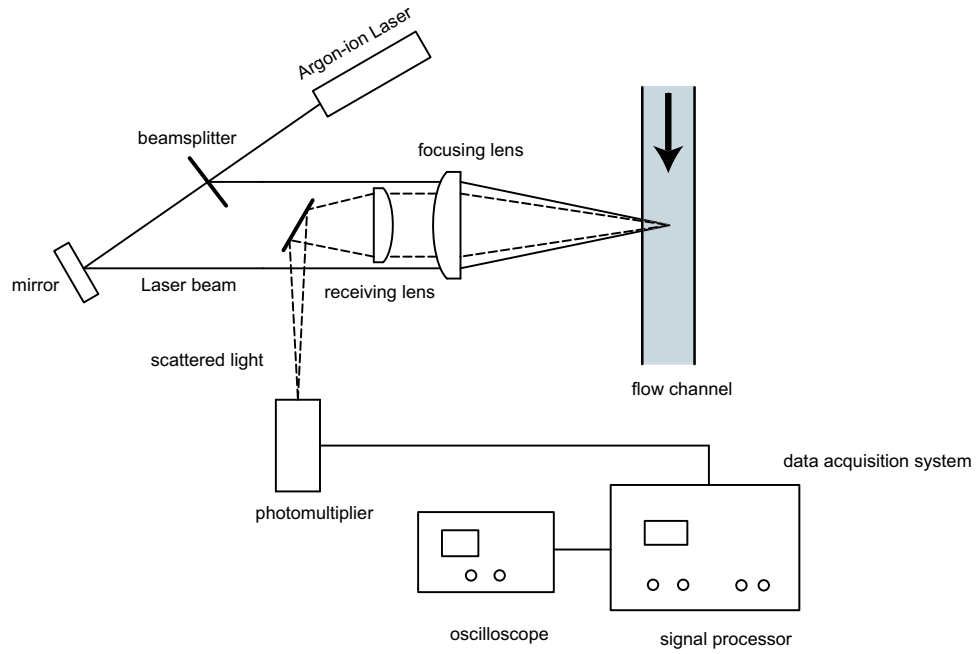


FIGURE B.1: Schematic of single beam LDV system.

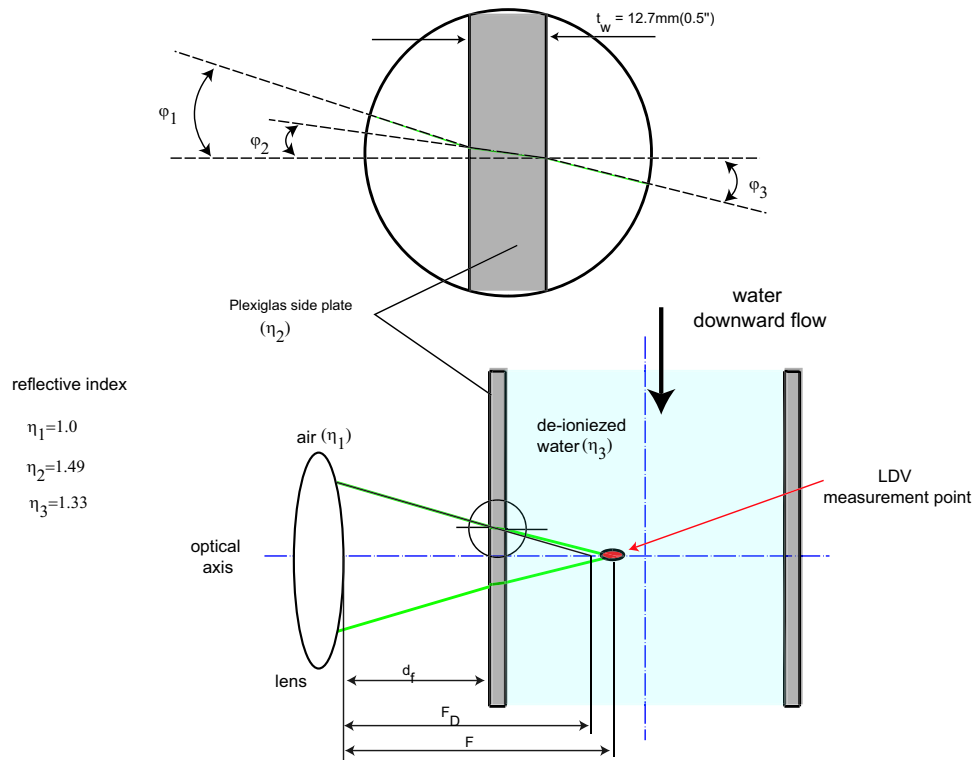


FIGURE B.2: Schematic of positioning of the LDV measuring volume (measurement point) in the channel

TABLE B.1: Pressure transmitters and their application

Device Make, type	Model	Serial number	Range calibrated	Measurement application
Rosemount DP Transmitter	C1151DP3 E12B1C6	R-C37686	0–7 kPa	DPFUL
Rosemount DP Transmitter	C1151DP3 E12B1C6	R-C37694	0–7 kPa	DPOUT
Rosemount DP Transmitter	C1151DP4 E12B1C6	R-C37529	0–35 kPa	DPTS
Rosemount DP Transmitter	C1151DP5 E12B1C6	R-C384674	0–70 kPa	PRTS
Rosemount DP Transmitter	C1151DP4 E12B1C6	R-C42371	0–35 kPa	Flow orifice meter

B.2 Differential pressure transmitter

The pressure transmitters used to measure pressure drop are listed in Table B.1. The calibration of these individual pressure transmitters was separately undertaken by Stern Laboratories (SL).

For Rosemount pressure transmitters, the following equation is used to calculate pressure:

$$P = A + B(V - V_{\text{offset}}) + C(V - V_{\text{offset}})^2 \quad (\text{B.3})$$

where P =pressure, [Pa]; V_{offset} =measured zero-offset voltage when the transmitter is equalized, [V]; V =measured voltage signal from the transmitter, [V]; A, B, C =SL calibration constants. The constant A in the above equation is set to zero during calibration. It is then used to store the sense line static head correction for the absolute pressure measurements and the manufacturer's correction factor, K , for a span shift for the differential pressure measurements.

Differential pressure transmitters are calibrated at atmospheric pressure, but they are used at higher static pressures, causing a span shift in the instrument. The

span shift is corrected by a correction factor, K , for each measurement. This factor represents the percentage shift of the reading per 6.895 MPa (g), and varies from -0.55 to -1.75% depending on a model of the transmitter. Since the span shift is negative, the measured voltage at high line pressure must be decreased to account for the fact that the pressure cell is calibrated at atmospheric pressure. Compensation for the span shift is made using the following equation:

$$\Delta V_{\text{correction}} = \frac{(V_{\text{zero}} - V_{\text{measured}}) P_s K}{1 + P_s K} \quad (\text{B.4})$$

where $V_{\text{correction}}$ =correction to be applied to measured voltage, [V]; V_{measured} =measured output from transmitter, [V]; P_s =line pressure, [psig]; K =correction factor.

B.3 Flow orifice meter

The flow orifice meter with the differential pressure transmitter was calibrated by SL. The average value of the discharge coefficient of this orifice meter was determined; $C_d=0.617$. Its calibration data are shown below. The mass flow rate (M) calculation for the orifice is given by:

$$M = C_d E F_a \varepsilon (\pi/4) d^2 (2DP\rho)^{1/2} \quad (\text{B.5})$$

where C_d =discharge coefficient; E =velocity approach factor, $E = \frac{1}{\sqrt{1-\beta^4}}$; β =diameter ratio, $\beta = \frac{d_{\text{orifice}}}{D_{\text{tube}}}$; F_a =thermal expansion factor, ρ =density of fluid, kg/m^3 ; d =orifice meter diameter in meter; ε =expansion factor, $\varepsilon=1$ for water; DP =measured differential pressure difference across the orifice meter in kPa.

B.4 Type T thermocouple

To convert measured thermocouple output voltage to its corresponding temperature, the type T thermocouple equation of 7th order inverse polynomial was developed by SL over a range of -270 to 400 °C. This equation is based on the standard table developed by the National Institute of Science and Technology (NIST):

$$T(^{\circ}\text{C}) = f(mV + 2.7110) \quad (\text{B.6})$$

TABLE B.2: Coefficients of 7th order inverse polynomial for the temperature conversion of thermocouple output voltage to temperature

Coefficient	mV<0	mV \geq 0
A_1	2.5949192E+01	2.592800E+01
A_2	-2.1316967E-01	-7.602961E-01
A_3	7.9018692E-01	4.637791E-02
A_4	4.2527777E-01	-2.165394E-03
A_5	1.3304473E-01	6.048144E-05
A_6	2.0241446E-02	-7.293422E-07
A_7	1.2668171E-03	0

where f=7th order inverse polynomial, $f(x) = A_1x + A_2x^2 + A_3x^3 + A_4x^4 + A_5x^5 + A_6x^6 + A_7x^7$; mV = measured thermocouple output voltage; 2.7110 = equivalent millivolt value for the SL reference temperature of 65.56 °C. The coefficients of 7th order inverse polynomial are summarized in Table B.2.

Appendix C

Calculation of average velocity

Velocity measurement was undertaken in the bottom section of the calming length duct to examine the flow condition in the top end fitting and vertically at two elevations of $Z = 1$ and 300 mm in the flow channels. Average velocity was estimated from the time-averaged local velocity, in order to calculate the flow rate and the channel-to-channel flow distribution through the assembly.

C.1 Calculation of average velocity in calming length

In order to check the inlet flow condition to the top end fitting, axial velocity measurement was undertaken at 66 points (11 (X) x 6 (Y) points) in the calming length, as shown in Fig. C.1. It is only half of the cross-sectional area of the rectangular duct due to its geometric symmetry and the velocity measurement difficulty in the other half from the excessive light reflection of laser beam by the other side plate. To calculate the average velocity in the cross-sectional area of the duct, it is assumed that the velocity in the cell area around each measurement point is uniform as shown in figure. Hence, the average velocity in the calming length, $U_{\text{avg,CL}}$, can be calculated:

$$U_{\text{avg,CL}} = \frac{\sum_{i,j} U_{i,j} A_{i,j}}{\sum_{i,j} A_{i,j}} \quad (\text{C.1})$$

where, $U_{i,j}$ =local time-averaged velocity at the measurement point; $A_{i,j}$ =cell area around the measured local velocity.

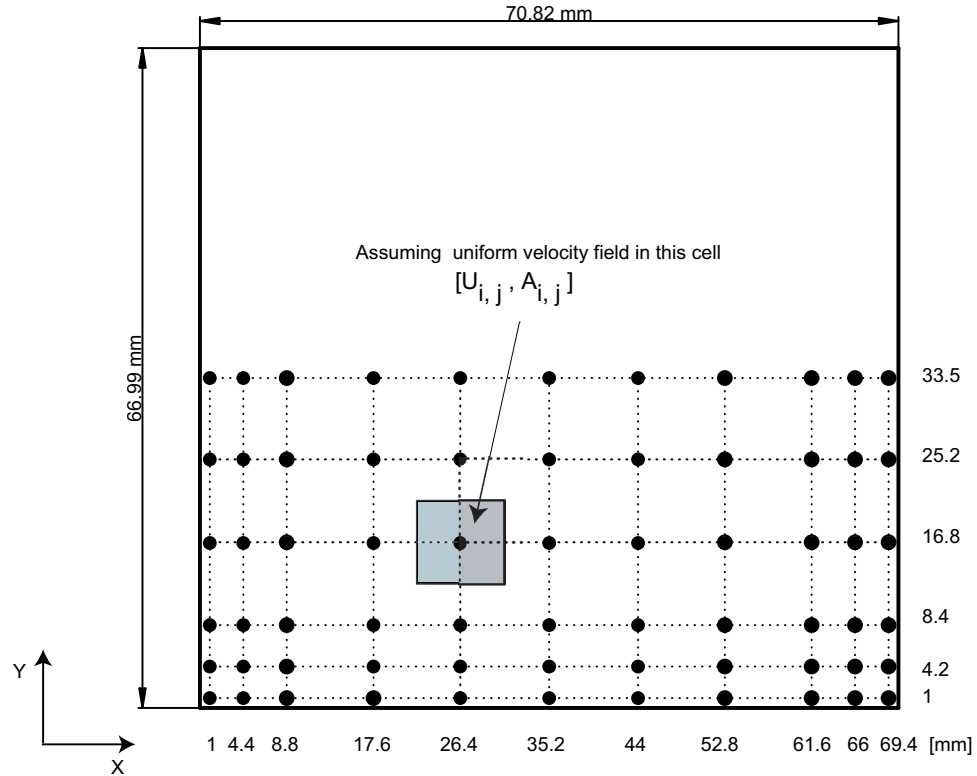


FIGURE C.1: Velocity measurement points and scheme of average velocity calculation in calming length on top of test section

C.2 Calculation of average velocity in channels

Axial velocity was measured in only 54 points in the cross-sectional area of the channels 1 to 9 in the 1/4 cross-sectional area of the assembly as shown in Fig. 5.8: six points in an individual channel for nine channels. The excessive light reflection of laser beam by the other side plate limited the measurement to half the area in every channel close to the laser beam. The channels in the assembly have a high aspect ratio, and their thickness is only 2.97 mm. This limited single measurement at the thickness-wise center in the Y direction in each channel, as shown in Fig. C.2. There is high possibility that these narrow long channels may not be precisely aligned with the LDV beam, and the Al plates may be slightly curved in the width-wise direction on the process of manufacturing or assembling the test section, because of their very small thickness. Even a slight misalignment of the LDV beam with the channels can cause sensitively the large deviation from the thickness-wise center in the channels.

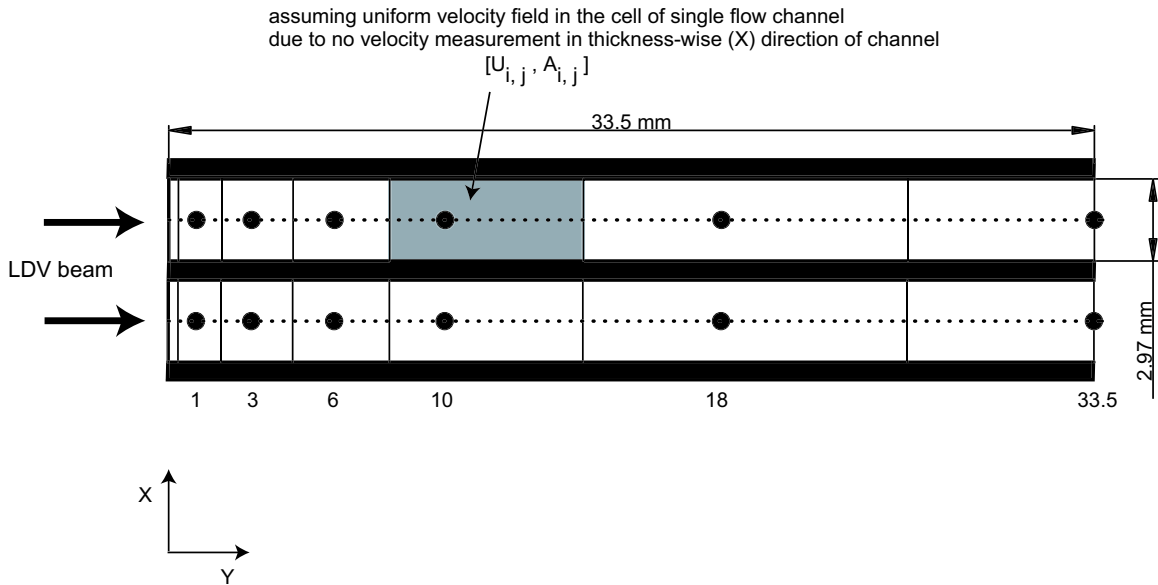


FIGURE C.2: Velocity measurement points in half channel and scheme of calculation of channel average velocity in the test section. Note that only 2 channels are illustrated in the figure.

This can lead to the significant deviation of the velocity at their thickness-wise center in the channels.

The channel average velocity in the channels of the test section is calculated in the same manner as in the calming length duct. The assembly average velocity is arithmetically calculated from the average velocity from channels 1 to 9 to evaluate the channel-to-channel flow distribution through the assembly. It is assumed that the velocity in the cell area around the velocity measurement point is uniform, as illustrated in Fig. C.2. It is anticipated that the velocity gradient in the Y direction may exist only in the outer corners near the side plates (i.e., $Y=0-6$ mm), whereas the velocity may be almost constant in the relatively wider central region (i.e., $Y=6-33.5$ mm). Hence, the error induced from the approximation of channel average velocity based on the assumption of the uniform velocity in the cell in the figure can be significantly reduced. However, the velocity gradient in the thickness-wise (X) direction should also exist in the channels. This is considered to evaluate the flow rate from the measured width-wise (Y) velocity distribution in the channels, using the logarithm law by Eq. 4.8 in Section 6.10.

Appendix D

Possible flow development past the handle in top end fitting

The velocity profile developing from the calming length duct is observed to be nearly symmetric and uniform in the core-region of the duct, as discussed in Section 6.3 although it is presumed that the fully developed profile was not completely attained at the bottom. After the calming length, flow meets the handle, which is positioned 38.1 cm above the fuel plates in the top end fitting. It partially/completely obstructs the flow area of middle channels 8 to 10 from the top plan view of the assembly (see Fig. 4.3). The nearly uniform and symmetric developing flow from the calming length should be considerably disturbed downstream due to the wake past the handle as illustrated in Fig. D.1.

The flow on its either side may be accelerated due to gradual contraction and expansion of the flow area, whereas the wake may be formed directly underneath the handle. Two similar axial velocity profiles on either side may form downstream: the high velocity in the center of each side and nearly zero velocity in the immediate proximity of sidewalls and just underneath the handle. This is similar to a dumbbell-shape profile. This profile may be redeveloping downstream toward the duct profile. However, the length of the top end fitting below the handle is only 38.1 mm ($4.0D_{h,handle}$), and may not be long enough for the fully developed profile to be completely re-established. Thus, the dumbbell-shape profile recovers gradually downstream but a slightly a blunted downstream just above the inlet of the channels: relatively low velocity above the inlet of middle channels 8 to 10 and high velocity in central channels 4 to 7 and 11 to 14.

The velocity profile in the Y-direction may not be influenced because the handle is completely aligned with the narrow rectangular channels in their width-wise (Y)

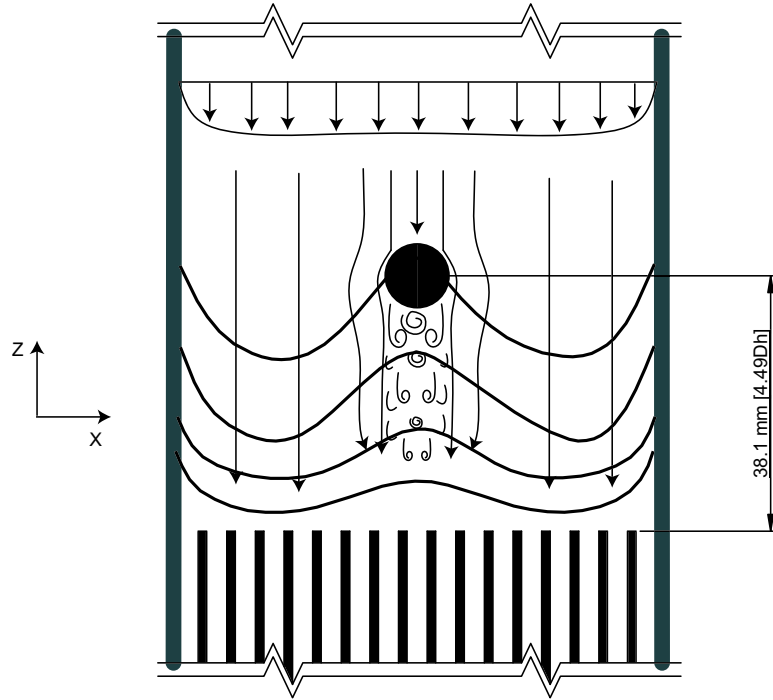


FIGURE D.1: Schematic of the possible flow streams and the axial velocity distribution in the top end fitting

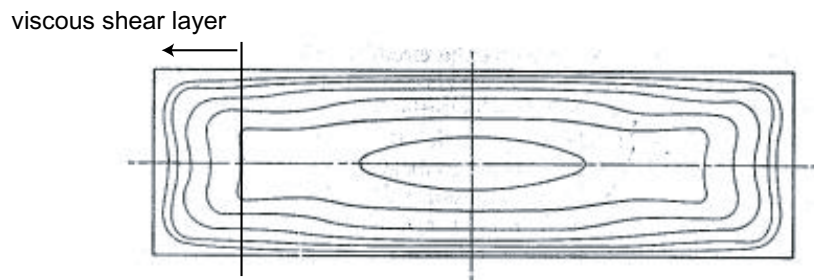
direction. Thus, it is assumed that the influence of the handle on the Y-direction velocity profile in the top end fitting is negligible.

In summary, the axial velocity distribution past the handle (just above the channel inlet) may be blunted dumb-bell shape profile due to the handle presence in the top end fitting. However, the velocity distribution in the Y-direction may not be influenced since the narrow channels of the assembly are completely aligned with the handle.

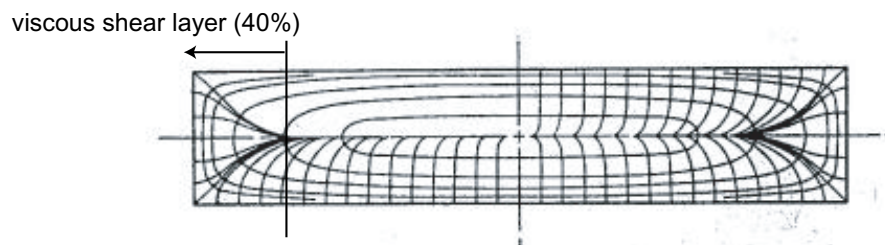
Appendix E

Width-wise (Y) velocity distribution in narrow channel with large aspect ratio

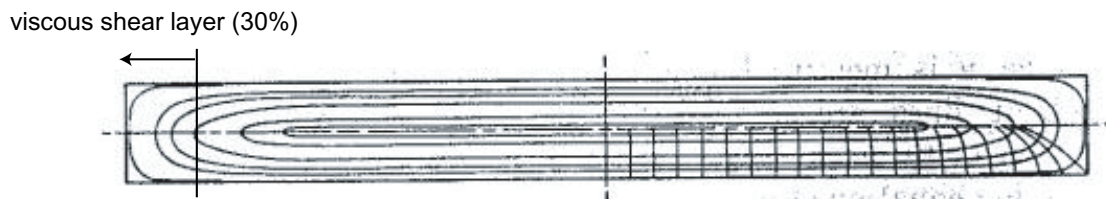
Few studies of the width-wise velocity distribution in the channels with high aspect ratio (AR) have been documented so far. The hydraulic studies in the narrow channels have normally been focused on the thickness-wise velocity distribution in the channels. Harnett, et. al [12] calculated the velocity field in the rectangular ducts of different AR to compare the predicted and measured friction factors for turbulent flow through rectangular ducts. The computed velocity profile and the experimental profile from Nikuradse are shown in Fig. E.1. It shows that the viscous shear layer solely due to side-plates wall was confined in the immediate proximity of the side-plate walls, and its relative portion in the duct was decreased with increasing AR. For instance, the viscous shear layer due to the side walls was limited to 40% of the channel in the width-wise length with AR=5:1, and 30% with AR = 10:1 in Figure E.1.



(a) experimental velocity contour in the rectangular duct of AR=3.5:1; Data from NiKurdse.



(b) computed velocity contour in the rectangular duct of AR=5:1



(c) computed velocity contour in the rectangular duct of AR=10:1

FIGURE E.1: Turbulent velocity profiles in rectangular channel

Appendix F

Flow rate calculation from the width-wise velocity distribution

The flow rate evaluated from the measured width-wise velocity distribution in each channel must be overestimated. This overestimated flow rate can be corrected by considering the thickness-wise velocity gradient in the channels, using the logarithm law by Eq. (4.8). The detailed calculation is as follows:

import the friction factor calculation sheet

☞ Reference: D:\MA Thesis\Text\CH 7\MathCad\friction_factor-02.mcd

Calculate the total flow area of the 17 channels in the assembly

$$\text{Area} := 17 \cdot (2.97 \cdot 10^{-3}) \cdot (66.99 \cdot 10^{-3}) \quad \text{Area} = 3.382 \times 10^{-3}$$

Import the nominal flow rate, and the assembly average velocity evaluated from the width-wise velocity distribution.

A :=  D:\..\flowrate.xls experimental data

M := A⁽⁰⁾ nominal flow rate[kg/s]

Re := A⁽¹⁾ Reynolds number

U_m := A⁽²⁾ measured average velocity in the channel at a given flow rate

To calculate the flow rate from the measured quantities of the width-wise velocity distribution, the average velocity in the assembly at given flow rate should be determined and then flow rate can be simply calculated:

$$M = \rho \cdot U \cdot \text{Area}$$

where M[kg/s], ρ = density,
U = average velocity at given flow rate,
Area = total flow area in the assembly.

Calculate the flow rate

$$i := 0..6$$

M_U := $\rho \cdot U_m \cdot \text{Area}$ from the assembly average velocity from the width-wise velocity distribution

To correct the overestimation of the flow rate evaluated directly from the measured width-wise velocity distribution, the thickness-wise velocity gradient in the channels can be considered by using the logarithm law of Eq. (4.8). The ratio of the average velocity to the maximum velocity by Eq. (4.8) is given by:

$$\text{Ratio} = \frac{V}{U_c} = \frac{1}{1 + 0.86\sqrt{f}}$$

$$f_{ch} := \begin{pmatrix} FF_{1,200} \\ FF_{1,250} \\ FF_{1,300} \\ FF_{1,350} \\ FF_{1,400} \\ FF_{1,450} \\ FF_{1,500} \end{pmatrix}$$

calculate the friction factor at given flow rate for Eq. (4.8)

$$\text{Ratio} := \frac{1}{1 + 0.86\sqrt{f_{ch}}}$$

M[kg/s] Ratio

2	0.848
2.5	0.851
3	0.853
3.5	0.854
4	0.856
4.5	0.856
5	0.857

$$\text{RATIO} := \text{augment}(M, \text{Ratio})$$

$$\text{RATIO} =$$

M corrected by considering the thickness-wise velocity in the channel by the logarithm law

$$M_{c_i} := M_{U_i} \cdot \text{Ratio}_i$$

$$M_{\text{comp}} := \text{augment}(M, M_U, M_c)$$

M_n M_U M_c Unit [kg/s]

$$M_{\text{comp}} =$$

2	2.496	2.117
2.5	3.074	2.616
3	3.592	3.063
3.5	4.182	3.573
4	4.711	4.03
4.5	5.258	4.503
5	5.738	4.919

Estimate the error of each flow rate evaluated from the measured width-wise velocity distribution.

$$\text{Error}_{1_i} := \frac{(M_{U_i} - M_i)}{M_i} \cdot 100$$

Error for the flow rate evaluated directly from the width-wise velocity distribution

$$\text{Error}_{2_i} := \frac{(M_{C_i} - M_i)}{M_i} \cdot 100$$

Error for the flow rate evaluated by considering the thickness-wise velocity gradient in the channels with the width-wise velocity distribution

$$\text{Error} := \text{augment}(M, \text{Error}_1, \text{Error}_2)$$

Summary of error in the flow rate evaluation:

	M_n	M_U	M_c	Unit [%]
Error =	2	24.777	5.871	
	2.5	22.954	4.64	
	3	19.718	2.11	
	3.5	19.473	2.073	
	4	17.769	0.751	
	4.5	16.837	0.063	
	5	14.763	-1.625	

Write the result onto the file



D:\..\flowrate.dat

M_{comp}

Appendix G

Pressure drop calculation by a 1-D simple correlation and its comparison with the experimental Data

G.1. Calculation of friction factor

$$N_{Re}(u, Dh, \rho, \mu) := \rho \cdot Dh \cdot \frac{u}{\mu}$$

$$N_{Re}(u, Dh, \nu) := Dh \cdot \frac{u}{\nu}$$

$\rho := 995.65$ density at $T=30$ °C
 $\mu := 797.35 \cdot 10^{-6}$ viscosity at $T=30$ °C
 $\nu := \frac{\mu}{\rho}$
 $\nu = 8.008 \times 10^{-7}$

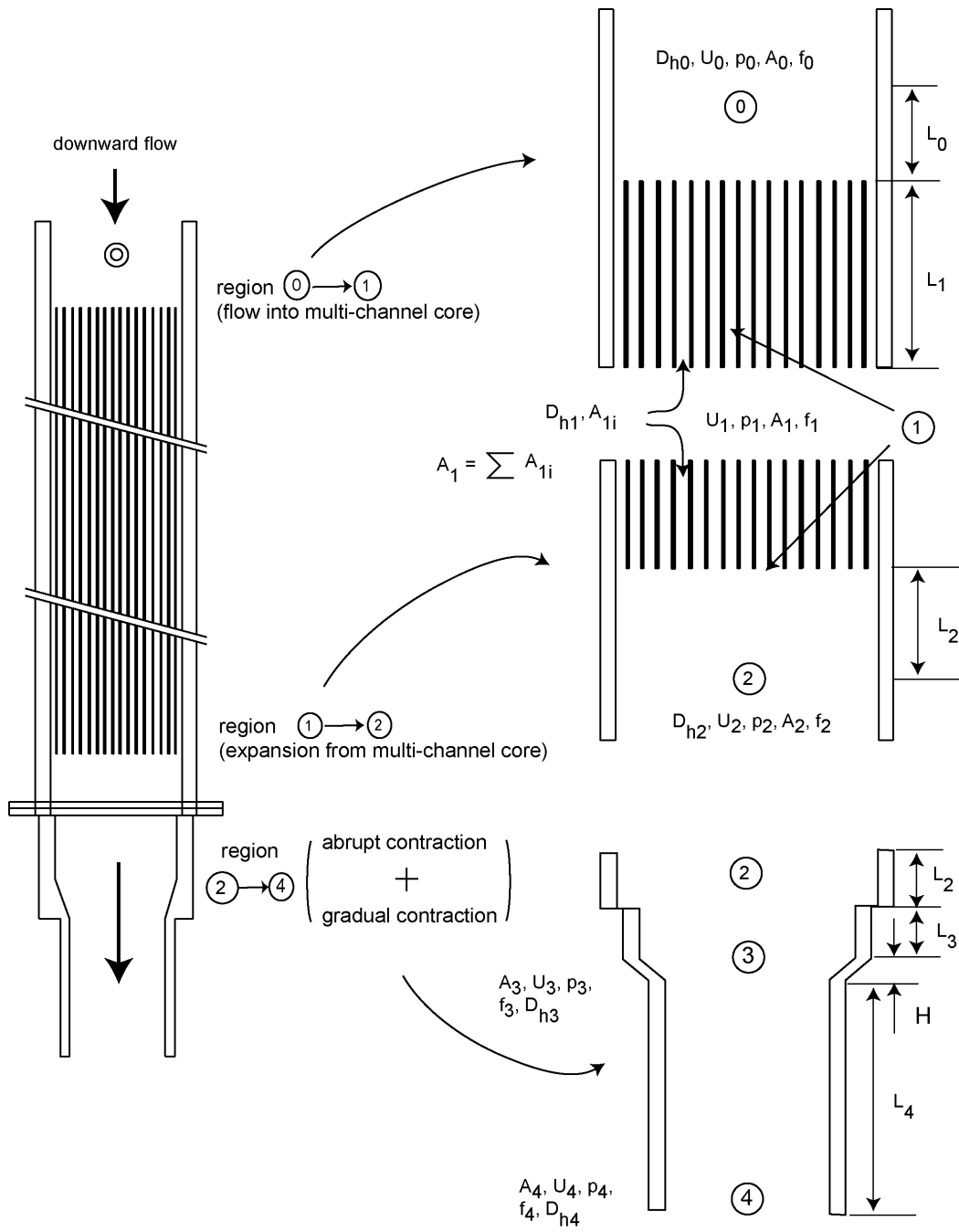
where $\rho = \text{density} \left(\frac{\text{kg}}{\text{m}^3} \right)$
 $D = \text{hydraulic diameter (m)}$
 $\nu = \text{flow velocity} \left(\frac{\text{m}}{\text{s}} \right)$
 $\mu = \text{dynamic viscosity} \left(\frac{\text{N} \cdot \text{s}}{\text{m}^2} \right)$
 $\nu = \text{kinematic viscosity} \left(\frac{\text{m}^2}{\text{s}} \right)$

Length of the given region in the assembly unit[m]

$L_0 := 0.0254$	length of the top end fitting
$L_1 := 0.6255$	length of the 17 flow channels
$L_2 := 0.0127$	length of the plates-free duct
$L_3 := 0.0254$	length of the larger diameter pipe in the bottom end fitting
$L_4 := 0.1524$	length of the smaller diameter pipe in the bottom end fitting
$H := 0.019$	length of the gradual contraction from larger diameter pipe to smaller one in the bottom end fitting

Index of the following figure

region index: 0 = top end fitting
 1 = plate region
 2 = plate-free region
 3 = upper bottom end fitting pipe
 4 = lower bottom end fitting pipe



NOTE: Drawings not scaled

Flow area calculation in the 18-plates assembly in each region

$$A_0 := 66.99 \cdot 10^{-3} \cdot 70.82 \cdot 10^{-3}$$

$$A_0 = 4.744 \times 10^{-3}$$

$$A_1 := 17 \cdot (2.97 \cdot 10^{-3} \cdot 66.99 \cdot 10^{-3})$$

$$A_1 = 3.382 \times 10^{-3}$$

$$A_2 := 66.99 \cdot 10^{-3} \cdot 70.82 \cdot 10^{-3}$$

$$A_2 = 4.744 \times 10^{-3}$$

$$A_3 := \pi \cdot \left(\frac{62.71 \cdot 10^{-3}}{2} \right)^2$$

$$A_3 = 3.089 \times 10^{-3}$$

$$A_4 := \pi \cdot \left(\frac{50.8 \cdot 10^{-3}}{2} \right)^2$$

$$A_4 = 2.027 \times 10^{-3}$$

Hydraulic diameter calculation in each region

$$Dh_0 := \frac{4 \cdot (66.99 \cdot 10^{-3} \cdot 70.82 \cdot 10^{-3})}{2 \cdot (66.99 \cdot 10^{-3} + 70.82 \cdot 10^{-3})}$$

$$Dh_0 = 0.069$$

$$Dh_1 := \frac{4 \cdot (66.99 \cdot 10^{-3} \cdot 2.97 \cdot 10^{-3})}{2 \cdot (66.99 \cdot 10^{-3} + 2.97 \cdot 10^{-3})}$$

$$Dh_1 = 5.688 \times 10^{-3}$$

$$Dh_2 := \frac{4 \cdot (66.99 \cdot 10^{-3} \cdot 70.82 \cdot 10^{-3})}{2 \cdot (66.99 \cdot 10^{-3} + 70.82 \cdot 10^{-3})}$$

$$Dh_2 = 0.069$$

$$Dh_3 := 62.71 \cdot 10^{-3}$$

$$Dh_3 = 0.063$$

$$Dh_4 := 50.80 \cdot 10^{-3}$$

$$Dh_4 = 0.051$$

To estimate the friction factor, f in the rectangular channel, it is recommended that a correction factor be used to calculate the friction factor from the pipe flow. The correction factor for laminar and turbulent regimes are evaluated in each region by Equation (4-17) and (4-18).

$$C_{lam_0} := 1.503 - 1.894 \cdot \left(\frac{66.99}{70.82} \right) + 2.034 \cdot \left(\frac{66.99}{70.82} \right)^2 - 0.755 \cdot \left(\frac{66.99}{70.82} \right)^3$$

$$C_{tur_0} := 1.097 - 0.177 \cdot \left(\frac{66.99}{70.82} \right) + 0.083 \cdot \left(\frac{66.99}{70.82} \right)^2$$

$$C_{lam_1} := 1.503 - 1.894 \cdot \left(\frac{2.97}{66.99} \right) + 2.034 \cdot \left(\frac{2.97}{66.99} \right)^2 - 0.755 \cdot \left(\frac{2.97}{66.99} \right)^3$$

$$C_{tur_1} := 1.097 - 0.177 \cdot \left(\frac{2.97}{66.99} \right) + 0.083 \cdot \left(\frac{2.97}{66.99} \right)^2$$

$$C_{lam_2} := C_{lam_0}$$

same dimension as in the top end fitting

$$C_{tur_2} := C_{tur_0}$$

In case of pipe, correction factor is taken as 1.

For the larger bottom end fitting pipe

$$C_{lam_3} := 1.0$$

$$C_{tur_3} := 1.0$$

For the smaller bottom end fitting pipe

$$C_{lam_4} := 1.0$$

$$C_{tur_4} := 1.0$$

Summary of correction factors in laminar and turbulent regimes

$$C_{factor} := \text{augment}(C_{lam}, C_{tur})$$

	0.892	1.004
	1.423	1.089
$C_{factor} =$	0.892	1.004
	1	1
	1	1

For an estimation of the friction factor, the Colebrook equation is used by Equation (4-18)

Colebrook equation for turbulent flow

$$\frac{1}{\sqrt{f}} = -2 \cdot \log \left(\frac{\varepsilon}{3.7 \cdot Dh} + \frac{2.51}{N_{Re}(u, Dh, \nu) \cdot \sqrt{f}} \right) \quad \text{where } f = \text{friction factor}$$

$$\varepsilon = \text{roughness}$$

to be solved for f by ROOT function

$$FA(f, \varepsilon, Dh, u, \nu) := \frac{1}{\sqrt{f}} + 2 \cdot \log \left(\frac{\varepsilon}{3.7 \cdot Dh} + \frac{2.51}{N_{Re}(u, Dh, \nu) \cdot \sqrt{f}} \right) \quad \text{no correction applied}$$

$$FB(f, \varepsilon, Dh, u, \nu, C_{tur}) := \frac{1}{\sqrt{C_{tur} \cdot f}} + 2 \cdot \log \left(\frac{\varepsilon}{3.7 \cdot Dh} + \frac{2.51}{N_{Re}(u, Dh, \nu) \cdot \sqrt{C_{tur} \cdot f}} \right)$$

correction applied

Calculate friction factors as function of mass flow rate:

$dM := 0.01$ flow rate increment

$j := 1..600$ range of flow rate

$i := 0..4$

$M_j := j \cdot dM$ $\max(M) = 6$

$u_{i,j} := \frac{M_j}{A_i \cdot \rho}$ average velocity

$Re_{i,j} := N_{Re}(u_{i,j}, Dh_i, \nu)$ Reynolds no

$Re_{lam} := 2000$ Reynolds numbers defining transition from laminar to turbulent

$Re_{tur} := 3000$

$\varepsilon := 0.046 \cdot 10^{-3}$ roughness of the Al plates

Compute friction factors f and minor loss coefficient in each region for laminar and turbulent regimes.

$$f := 0.001 \quad \text{initial guess of } f \quad i := 0..4$$

$$FF_{i,j} := \begin{cases} a_{i,j} \leftarrow N_{Re}(u_{i,j}, Dh_i, \nu) \\ b_{i,j} \leftarrow \text{root}\left(\text{FB}(f, \varepsilon, Dh_i, u_{i,j}, \nu, C_{tur,i}), f\right) \\ c_{i,j} \leftarrow \frac{64 \cdot C_{lam,i}}{N_{Re}(u_{i,j}, Dh_i, \nu)} \\ ft_{i,j} \leftarrow \frac{a_{i,j} - Re_{lam}}{Re_{tur} - Re_{lam}} \\ fl_{i,j} \leftarrow 1 - ft_{i,j} \\ c_{i,j} \text{ if } a_{i,j} \leq Re_{lam} \\ (ft_{i,j} \cdot b_{i,j} + fl_{i,j} \cdot c_{i,j}) \text{ if } a_{i,j} \geq Re_{lam} \wedge a_{i,j} \leq Re_{tur} \\ b_{i,j} \text{ otherwise} \end{cases}$$

Computer the minor loss coefficient in the given region

$$K1_j := \begin{cases} R_j \leftarrow N_{Re}(u_{1,j}, Dh_1, \nu) \\ s_j \leftarrow 0.64 + \frac{38}{R_j} \\ t_j \leftarrow \frac{1}{2} \left(1 - \frac{A_1}{A_0} \right) \\ s_j \text{ if } R_j \leq 2000 \\ t_j \text{ otherwise} \end{cases} \quad K2_j := \begin{cases} R_j \leftarrow N_{Re}(u_{2,j}, Dh_2, \nu) \\ s_j \leftarrow 0.0 \\ t_j \leftarrow \left(1 - \frac{A_1}{A_2} \right)^2 \\ s_j \text{ if } R_j \leq 2000 \\ t_j \text{ otherwise} \end{cases}$$

$$K3_j := \begin{cases} R_j \leftarrow N_{Re}(u_{3,j}, Dh_3, \nu) \\ s_j \leftarrow 1.20 + \frac{38}{R_j} \\ t_j \leftarrow \frac{1}{2} \left(1.0 - \frac{A_3}{A_2} \right) \\ s_j \text{ if } R_j \leq 2000 \\ t_j \text{ otherwise} \end{cases} \quad K4_j := \begin{cases} R_j \leftarrow N_{Re}(u_{4,j}, Dh_4, \nu) \\ s_j \leftarrow \frac{64}{R_j} \\ t_j \leftarrow 0.075 \\ s_j \text{ if } R_j \leq 2000 \\ t_j \text{ otherwise} \end{cases}$$

G. 2 Pressure drop calculation

Import the calculation of the frictional factors to evaluate the pressure drop:


 Reference: D:\MA Thesis\Text\CH 7\MathCad\friction_factor-02.mcd

Import the experimental data.

DP := 
D:\..\exp_data.xls

x1 := DP^{<0>} M[kg/s]
y1 := DP^{<1>} DPTS[kPa]
y2 := DP^{<2>} DPFUL[kPa]
y3 := DP^{<3>} DPOUT[kPa]

Import the result of Yu's numerical simulation.

DP_{Yu} := 
D:\..\Yu_numerical_data.xls

x2 := DP_{Yu}^{<0>} M[kg/s]
z1 := DP_{Yu}^{<1>} DPFUL[kPa]
z2 := DP_{Yu}^{<2>} P at the channel exit [kPa]
z3 := DP_{Yu}^{<3>} P at the measurement point [kPa]
z4 := DP_{Yu}^{<4>} Difference of P [z2-z3] point [kPa]

To calculate the pressure drop from the measured static pressure change, the change in static pressure induced by an area change (reversible pressure change) should be excluded. This can be done by using Bernoulli' equation.

$$\text{Region (0) to (1): } \frac{p_0 - p_1}{\frac{1}{2}\rho \cdot U_1} = 1 - \left(\frac{A_1}{A_0}\right)^2$$

$$\text{Region (1) to (2): } \frac{p_1 - p_2}{\frac{1}{2}\rho \cdot U_1} = \left(\frac{A_1}{A_2}\right)^2 - 1$$

$$\text{Region (2) to (3): } \frac{p_2 - p_3}{\frac{1}{2}\rho \cdot U_3} = 1 - \left(\frac{A_3}{A_2}\right)^2$$

$$\text{Region (3) to (4): } \frac{p_3 - p_4}{\frac{1}{2}\rho \cdot U_4} = 1 - \left(\frac{A_4}{A_3}\right)^2$$

Import the velocity in the specified region at given flow rate

$$U := \begin{pmatrix} u_{1,150} & u_{3,150} & u_{4,150} \\ u_{1,200} & u_{3,200} & u_{4,200} \\ u_{1,250} & u_{3,250} & u_{4,250} \\ u_{1,300} & u_{3,300} & u_{4,300} \\ u_{1,350} & u_{3,350} & u_{4,350} \\ u_{1,400} & u_{3,400} & u_{4,400} \\ u_{1,450} & u_{3,450} & u_{4,450} \\ u_{1,500} & u_{3,500} & u_{4,500} \end{pmatrix}$$

	u1	u3	u4	[m/s]
U =	0.445	0.488	0.743	
	0.594	0.65	0.991	
	0.742	0.813	1.239	
	0.891	0.976	1.487	
	1.039	1.138	1.734	
	1.188	1.301	1.982	
	1.336	1.463	2.23	
	1.485	1.626	2.478	

Calculate the reversible pressure change due to the flow-area change in the given region

$$DP01 := \frac{1}{2} \cdot \rho \cdot (U^{(0)})^2 \cdot \left[1 - \left(\frac{A_1}{A_0} \right)^2 \right]$$

$$DP12 := \frac{1}{2} \cdot \rho \cdot (U^{(0)})^2 \cdot \left[\left(\frac{A_1}{A_2} \right)^2 - 1 \right]$$

$$DP23 := \frac{1}{2} \cdot \rho \cdot (U^{(1)})^2 \cdot \left[1 - \left(\frac{A_3}{A_2} \right)^2 \right]$$

$$DP34 := \frac{1}{2} \cdot \rho \cdot (U^{(2)})^2 \cdot \left[1 - \left(\frac{A_4}{A_3} \right)^2 \right]$$

Calculate the pressure drop from the measured static pressure change.

$$MDPFUL := \frac{[y2 \cdot 1000 - (DP01 + DP12)]}{1000} \quad \text{region (0)->(2)}$$

$$MDPOUT := \frac{[y3 \cdot 1000 - (DP23 + DP34)]}{1000} \quad \text{region (2)->(4)}$$

$$MDPTS := \frac{[y1 \cdot 1000 - (DP01 + DP12 + DP23 + DP34)]}{1000} \quad \text{region (0)->(4)}$$

$$MDP := \text{augment}(MDPTS, MDPFUL, MDPOUT)$$

$$DPFULchecking := \text{stack}(x1^T, y2^T, MDPFUL^T)$$

	1.5	2	2.5	3	3.5	4	4.5	5	M [kg/s]
DPFULchecking =	0.527	0.872	1.308	1.819	2.373	2.993	3.635	4.335	DP _{FUL} [kPa]
	0.527	0.872	1.308	1.819	2.373	2.993	3.635	4.335	MDP _{FUL} [kPa]

where: M [kg/s]: nominal flow rate
 DP_{FUL} [kPa]: measured static pressure change
 MDP_{FUL} [kPa]: measured pressure drop

NOTE: Since the flow area is contracted to the plate region and then expanded to the plate-free region (same flow area as the top end fitting), the measured static pressure change (DP_{FUL}) should be equal to the pressure drop (MDP_{FUL}) in the region (0)->(2) as shown in DPFULchecking.

G.2.1 Calculation of the pressure drop by 1-D correlation

Calculate the total friction factor in each region to evaluate the pressure drop in the given region.

Through the plate region

$$f_{\text{fuel}0_j} := \frac{FF_{0,j} \cdot L_0}{Dh_0}$$

$$f_{\text{fuel}1_j} := \frac{FF_{1,j} \cdot L_1}{Dh_1} + K1_j + K2_j$$

$$f_{\text{fuel}2_j} := \frac{FF_{2,j} \cdot \frac{L_2}{2}}{Dh_2}$$

Through the bottom-end fitting:

$$f_{\text{out}1j} := \frac{FF_{3,j} \cdot L_3}{Dh_3} + K_{3j} \quad f_{\text{out}2j} := \frac{FF_{4,j} \cdot L_4}{Dh_4} + K_{4j}$$

Calculate the pressure drop in each region from the calculated friction factor and minor loss coefficient by 1-D correlation

$$DPFUL_j := \left[\frac{\rho \cdot (u_{0,j})^2}{2} \cdot f_{\text{fuel}0j} + \frac{\rho \cdot (u_{1,j})^2}{2} \cdot f_{\text{fuel}1j} + \frac{\rho \cdot (u_{2,j})^2}{2} \cdot f_{\text{fuel}2j} \right] \cdot \frac{1}{1000} \quad \text{DPFUL}$$

$$DPOUT1_j := \left[\frac{\rho \cdot (u_{2,j})^2}{2} \cdot f_{\text{fuel}2j} + \frac{\rho \cdot (u_{3,j})^2}{2} \cdot f_{\text{out}1j} \right] \cdot \frac{1}{1000} \quad \text{DPOUT \#1}$$

$$DPOUT2_j := \left[\frac{\rho \cdot (u_{4,j})^2}{2} \cdot f_{\text{out}2j} \right] \cdot \frac{1}{1000} \quad \text{DPOUT \#2}$$

$$DPOUT_{\text{minor}j} := \left[\frac{\rho \cdot (u_{3,j})^2}{2} \cdot K_{3j} + \frac{\rho \cdot (u_{4,j})^2}{2} \cdot K_{4j} \right] \cdot \frac{1}{1000} \quad \text{minor pressure loss in DPOUT}$$

$$DPOUT_j := DPOUT1_j + DPOUT2_j$$

$$DPOUT = DPOUT\#1 + DPOUT\#2$$

$$DPTS_j := DPFUL_j + DPOUT_j$$

$$DPTS$$

$$DPTS_{\text{minor}j} := \left[\frac{\rho \cdot (u_{1,j})^2}{2} \cdot (K_{1j} + K_{2j}) + \frac{\rho \cdot (u_{3,j})^2}{2} \cdot K_{3j} + \frac{\rho \cdot (u_{4,j})^2}{2} \cdot K_{4j} \right] \cdot \frac{1}{1000}$$

Total minor pressure losses along the assembly

Rearrange the result to write on the file.

$$DPFUL_{1D} := \text{augment}(M, DPFUL)$$

$$DPOUT_{1D} := \text{augment}(M, DPOUT1, DPOUT2, DPOUT, DPOUT_{\text{minor}})$$

$$DPALL := \text{augment}(M, DPTS, DPFUL, DPOUT, DPTS_{\text{minor}})$$

Write the result onto files:

 D:\..\DPFUL.xls

 D:\..\DPOUT.xls

 D:\..\DPTS.xls

 D:\..\MDP.xls

DPFUL_{1D}

DPOUT_{1D}

DPALL

MDP

G.3. Comparison of pressure drop calculation

G.3.1 Comparison of the experimental data with Yu's numerical simulation

k := 0..4

$$\text{DIFF}_{\text{DPFUL}_k} := \frac{(y_{2k+3} - z_{1k})}{y_{2k+3}} \cdot 100$$

DIFF := augment(x2, DIFF_{DPFUL})

M[kg/s] [%]

3	-15.662
3.5	-7.789
4	-3.839
4.5	-2.424
5	-0.522

DIFF =

G.3.2 Comparison of the experimental data with 1-D correlation prediction

Calculate the difference (in percentage) between the experimental data and the prediction by 1-D correlation.

i := 0..7

j := 0..2

$$\text{DP1} := \begin{pmatrix} \text{DPTS}_{150} & \text{DPFUL}_{150} & \text{DPOUT}_{150} \\ \text{DPTS}_{200} & \text{DPFUL}_{200} & \text{DPOUT}_{200} \\ \text{DPTS}_{250} & \text{DPFUL}_{250} & \text{DPOUT}_{250} \\ \text{DPTS}_{300} & \text{DPFUL}_{300} & \text{DPOUT}_{300} \\ \text{DPTS}_{350} & \text{DPFUL}_{350} & \text{DPOUT}_{350} \\ \text{DPTS}_{400} & \text{DPFUL}_{400} & \text{DPOUT}_{400} \\ \text{DPTS}_{450} & \text{DPFUL}_{450} & \text{DPOUT}_{450} \\ \text{DPTS}_{500} & \text{DPFUL}_{500} & \text{DPOUT}_{500} \end{pmatrix}$$

$$\text{Diff}_{i,j} := \frac{(\text{DP1}_{i,j} - \text{MDP}_{i,j})}{\text{DP}_{i,j}} \cdot 100$$

DIFF := augment(x1, Diff)

	M	DP _{TS}	DP _{FUL}	DP _{OUT}
	[kg/s]	[%]	[%]	[%]
DIFF =	1.5	-1.568	-0.93	-6.848
	2	-1.729	0.091	-6.466
	2.5	-0.457	0.229	-1.245
	3	-3.42	0.629	-8
	3.5	-0.938	1.853	-5.66
	4	-0.189	2.88	-6.189
	4.5	3.764	4.501	-3.698
	5	6.784	5.87	-3.048

G.4 Ratio of pressure drop in each region to overall pressure drop along the assembly

To estimate the ratio of the pressure drop in the plate region (DP_{PLATE}) to that through the whole assembly (DPTS), the measured pressure drop from the top end fitting to the plate-free duct can be correct to the pressure drop exactly in the plate region (channel inlet to channel exit). This can be done by using the vertical pressure distribution of Yu's numerical simulation.

Pressure drop exactly in the plate region in Yu's numerical simulation over $M=3.0 \sim 5.0$ kg/s

$k := 0..4$

$$SPCplate_{Yu} := (z1 + z4) \cdot 1000$$

Static pressure change from channel inlet to channel exit in the plate region

Note: (-z4) includes the pressure increase due to the flow expansion in the plate-free duct and probably the flow separation at the contractio step due to the bottom end fitting.

$$DPplate_Yu_k := \frac{SPCplate_{Yu_k} - DP01_{k+3}}{1000}$$

Pressure drop in that region

Calculate the pressure drop from channel inlet to channel exit in the present experiment.

$$SPCplate_{exp_k} := (y2_{k+3} + z4_k) \cdot 1000$$

Static pressure change from channel inlet to channel exit

$$DPplate_exp_k := \frac{SPCplate_{exp_k} - DP01_{k+3}}{1000}$$

Pressure drop in that region

$$DPplate := \text{augment}(x2, DPplate_Yu, DPplate_exp)$$

Calculate the ratio ($Ratio_2$) of DP_{PLATE} to DPTS in the present experiment.

$$Ratio_{2_k} := \frac{DPplate_exp_k}{MDPTS_{k+3}} \cdot 100$$

$Ratio_2 := \text{augment}(x2, Ratio_2)$

	M	Yu	Exp
DPplate =	3	1.65	1.366
	3.5	1.95	1.765
	4	2.268	2.153
	4.5	2.709	2.621
	5	3.138	3.115

	M	[%]
Ratio ₂ =	3	62.55
	3.5	62.828
	4	60.194
	4.5	61.117
	5	61.011

Note: The comparison of DPFUL (pressure drop from the top end fitting to the plate-free duct) in the present experiment and Yu's simulation showed close agreement except for relatively large difference, especially at the lower flow rate (i.e., 3.0kg/s). The pressure drop from channel inlet to channel exit corrected by using the result of Yu's numerical simulation leads to the overall pressure drop through the assembly by approximately 60%.

G.5 Vertical pressure distribution in the plate region

To examine the vertical pressure distribution in the plate-free duct, the result of Yu's numerical simulation is plotted in Fig. G.1. It is observed that the pressure remains almost constant before the channel inlet and is linearly decreased in the plate region except for the sharp decrease in the entrance length of the channels. However, the pressure in the plate-free duct shows a different trend. It is increased immediately downstream of the channel exit due to the abrupt expansion by the half thickness of the plates, and then increased or decreased, depending on the channels' location. The pressure below the outer channels (1 to 3) close to the dummy plate is slightly increased, while that below the central channels (4 to 8) is decreased downstream due to the bottom end fitting. This phenomenon should be related to the flow separation at the contraction step in this region due to the bottom end fitting. This is consistent with the result of Dekam E.I. and Calvert J.R., which showed that the wall static pressure was slightly influenced by about $0.5D_h$ upstream due to the sudden transitions between square and rectangular ducts of the same cross-sectional area (see Fig. 5 [34]). The pressure measurement tap is located on the surface of the dummy plate in the plate-free duct (see Fig. 5.9). Hence, the measured pressure through the plate region (DPFUL) and the bottom end fitting (DPOUT) should be influenced by this flow separation, as indicated in the figure (b) and (c). Note that the measured pressure drop through the whole assembly (DPTS) should not be influenced by this flow separation. It is also observed that the pressure drop in the top end fitting before the channel inlet is negligible due to its short length (25.4 mm).

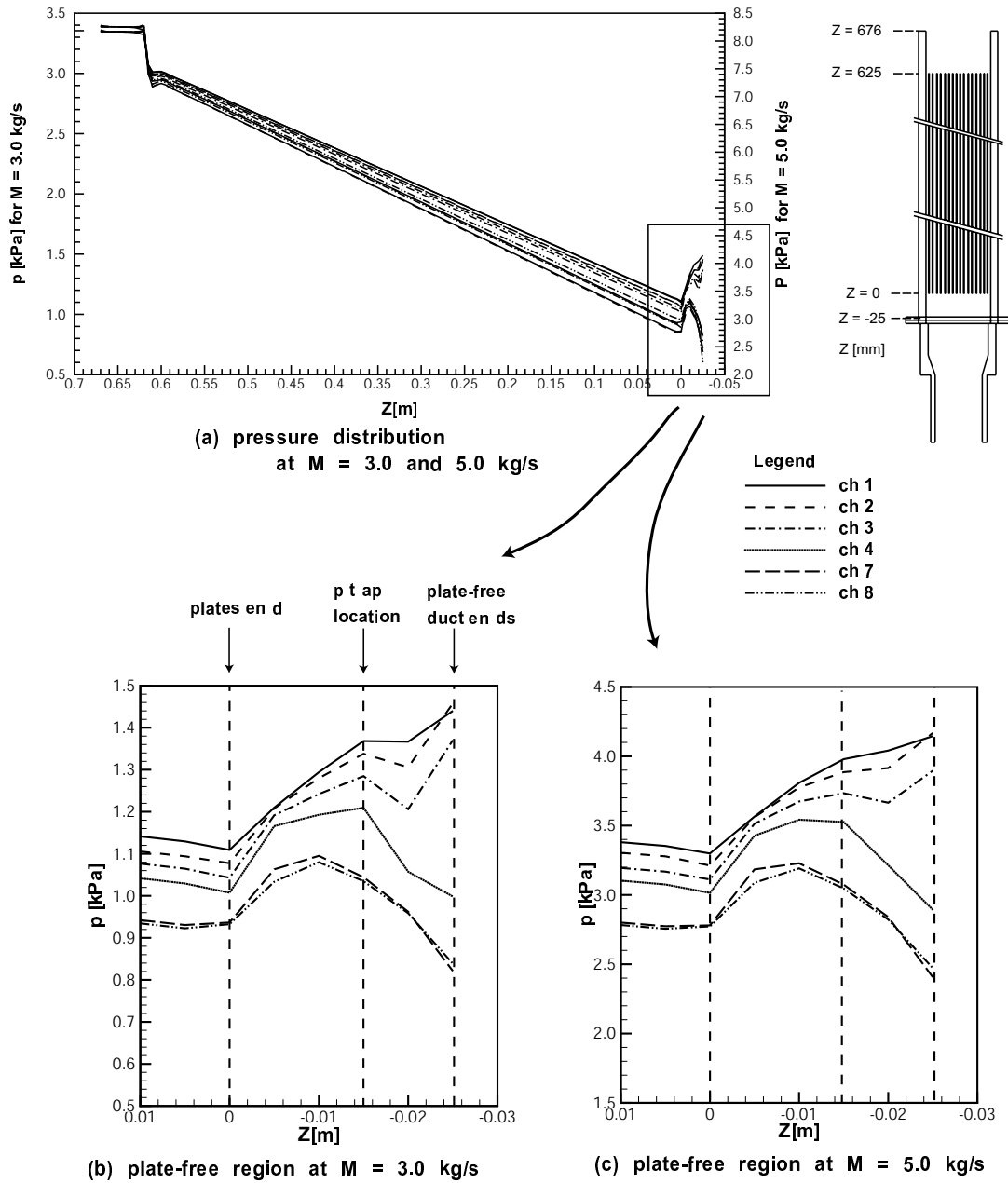


FIGURE G.1: Vertical pressure distribution along the assembly from Yu's numerical simulation

Appedix H

Error analysis of the measurement of pressure drop, flow rate and temperature

Measurement uncertainty is conducted, following the the procedure of the ANSI/ASME Standard on Measurement Uncertainty [33]. The total error in measurement consists of a fixed bias error and a random precision eerror, as shown in Equation (H-1). The uncertainty in measurements of pressure, flow rate, and temperature in the present experiment is calculated at the 95% confidence level:

$$U_{RSS} = \left[B_r^2 + (t \cdot S_r)^2 \right]^{\frac{1}{2}} \quad \text{for 95\% coverage} \quad (\text{H-1})$$

where, B_r = bias limit, S_r = precision index,
 t = value of the two-tailed student t for 95% confidence level.

For the estimation of single parameter uncertainty (i.e., pressure and temperature), Equation (H-1) can be directly used. Among elementary error sources, data acquisition errors and data reduction errors are neglected since they are not significantly contributed to overall errors. Here, all calibration error are considered bias error without separately considering the precision errors of instruments calibration.

On the other hand, flow rate is a function of several parameters (the pressure drop through orifice meter, density, discharge coefficient of orifice meter, and so on), as shown in equation (H-2). Thus, flow rate rarely can be directly measured. Errors of the measurements in these parameters are propagated to the measurement of the flow rate. This effect is considered as follows:

The flow rate is given by equation (B-5):

$$M = \frac{C \cdot F_a \cdot \varepsilon \cdot \left(\frac{\pi}{4} \right) \cdot d^2 \cdot \sqrt{2 \cdot \rho \cdot DP}}{\sqrt{1 - \beta^4}} \quad (\text{H-2})$$

The relative precision index (S_r) is:

$$\frac{S_M}{M} = \left[\left(1 \cdot \frac{S_C}{C} \right)^2 + \left(\frac{2}{1 - \beta^4} \cdot \frac{S_d}{d} \right)^2 + \left(\frac{2 \cdot \beta^4}{1 - \beta^4} \cdot \frac{S_D}{D} \right)^2 + \left(\frac{1}{2} \cdot \frac{S_\rho}{\rho} \right)^2 + \left(\frac{1}{2} \cdot \frac{S_{DP}}{DP} \right)^2 \right]^{\frac{1}{2}} \quad (\text{H-3})$$

The relative bias limit (B_r) is:

$$\frac{B_M}{M} = \left[\left(1 \cdot \frac{B_C}{C} \right)^2 + \left(\frac{2}{1 - \beta^4} \cdot \frac{B_d}{d} \right)^2 + \left(\frac{2 \cdot \beta^4}{1 - \beta^4} \cdot \frac{B_D}{D} \right)^2 + \left(\frac{1}{2} \cdot \frac{B_\rho}{\rho} \right)^2 + \left(\frac{1}{2} \cdot \frac{B_{DP}}{DP} \right)^2 \right]^{\frac{1}{2}} \quad (\text{H-4})$$

Since the contribution to overall error by the dimension of the system and fluid density is usually very samll, it can be neglected in the above equations.

Therefore. the uncertaintyv in flow rate bv the orifice meter can be evaluated as follows:

$$\frac{U_{RSS}}{M} = \left[\left(\frac{B_M}{M} \right)^2 + \left(2 \cdot \frac{S_M}{M} \right)^2 \right]^{\frac{1}{2}} \quad \text{for 95\% coverage} \quad (H-5)$$

H.1 Uncertainty in pressure drop measurement

Uncertainty in pressure drop measurement is calculated by Equation (H-1).

Import the data of the pressure and the flow rate of the present experiment

Data_info :=		DP ₀ :=	
	D:\..\datainfo.dat		D:\..\M15KGS.dat
DP ₁ :=		DP ₂ :=	
	D:\..\M20KGS.dat		D:\..\M25KGS.dat
DP ₃ :=		DP ₄ :=	
	D:\..\M30KGS.dat		D:\..\M35KGS.dat
DP ₅ :=		DP ₆ :=	
	D:\..\M40KGS.dat		D:\..\M45KGS.dat
DP ₇ :=			
	D:\..\M50KGS.dat		

M _{nominal} := Data_info ^{<0>}	Nominal flow rate
NO _{sample} := Data_info ^{<1>}	Number of samples of measurement
T _{value} := Data_info ^{<2>}	Student t value

Bias error from the calibration of individual pressure transmitters

B ₀ := 0.0044	pressure transmitter for the orifice meter (ΔP_M)
B ₁ := 0.0064	pressure transmitter for the DPTS through the assembly (ΔP_{TS})
B ₂ := 0.0015	pressure transmitter for the DPFUL through the plate region (ΔP_F)
B ₃ := 0.0019	pressure transmitter for the DPOUT through the bottom end fitting (ΔP_O)
B _C := 0.0121	discharge coefficient, dimensionless at C = 0.6170586

Calculate the uncertainty in pressure measurement

$$i := 0..7$$

$$j := 0..3$$

$$S_{i,j} := \text{Stdev}[(DP_i)^{\langle j \rangle}]$$

Precision index

$$U_{RSS_P_{i,j}} := \sqrt{(B_j)^2 + (T_{value_i} \cdot S_{i,j})^2}$$

Error evaluated by eq (H-1)

$$U_{RSS_P} =$$

	0	1	2	3
0	0.009	0.007	0.004	0.002
1	0.017	0.008	0.005	0.004
2	0.041	0.012	0.007	0.081
3	0.031	0.024	0.009	0.027
4	0.047	0.046	0.044	0.008
5	0.053	0.027	0.02	0.012
6	0.163	0.048	0.033	0.021
7	0.391	0.103	0.056	0.057

Column index:

0: DP in orifice meter

1: DPTS

2: DPFUL

3: DPIOUT

Error in (+/-) kPa

E.2 Uncertainty in flow rate measurement

Uncertainty in flow rate by the orifice meters calculated by using Equations (H-3), (H-4), and (H-5).

$$j := 4$$

$$a_{i,j} := \left[\left[B_C^2 + 0 + 0 + 0 + \left[\frac{1}{2} \cdot \frac{B_0}{\text{mean}[(DP_i)^{\langle 0 \rangle}]} \right]^2 \right]^2 \right]^{\frac{1}{2}}$$

$$a_{i,j} = \frac{B_M}{M}, \quad \text{by eq. (H-3)}$$

$$b_{i,j} := \left[0 + 0 + 0 + 0 + \left[\frac{1}{2} \cdot \frac{\text{Stdev}[(DP_i)^{\langle 0 \rangle}]}{\text{mean}[(DP_i)^{\langle 0 \rangle}]} \right]^2 \right]^{\frac{1}{2}}$$

$$b_{i,j} = \frac{S_M}{M} \quad \text{by eq. (H-4)}$$

$$c_{i,j} := \left[(a_{i,4})^2 + (2 \cdot b_{i,4})^2 \right]^{\frac{1}{2}}$$

$$c_{i,j} = \frac{U_{RSS}}{M} \quad \text{by eq. (H-5)}$$

$$U_{RSS_M_i} := c_{i,4}$$

0.0123
0.0123
0.0127
0.0122
0.0123
0.0122
0.013
0.015

Thus, the flow rate by the orifice meter is measured over the experimental range within less than a 1.5% error.

E.3 Uncertainty in temperature measurement

The uncertainty in measurement of temperature through the experimental loop is calculated by Equation (H-1).

Import the temperature data of T1, T2, T3

Temp :=  D:\Temperature.dat

Bias error (thermocouple T-type):

1. curve fitting of the 7th order inverse polynomials: $B_1 = 0.04 \text{ } ^\circ\text{C}$

2. T-type thermocouple has 1°C accuracy of operating range of $-270\text{--}400 \text{ } ^\circ\text{C}$: $B_2 = 1.0 \text{ } ^\circ\text{C}$

Student t value is taken 2.0 since number of sample = 182 by eq. (H-1)

since the number of temperature measurement is greater than 30, t value can be taken 2.0

$k := 0..2$

$$S_{Temp_k} := \text{Stdev}[(Temp)^{\langle k \rangle}] \quad \text{Precision index}$$

$$U_{RSS_T_k} := \sqrt{1.0^2 + 0.04^2 + (2.0 \cdot S_{Temp_k})^2}$$

$$U_{RSS_T_k} =$$

1.48	T1
1.46	T2
1.45	T3

Thus, the temperature along the test loop was measured within (+/-) $1.5 \text{ } ^\circ\text{C}$.